Impurity and boundary modes in the honeycomb lattice

Clément Dutreix

To cite this version:

Clément Dutreix. Impurity and boundary modes in the honeycomb lattice. Quantum Physics [quant-ph]. Université Paris Sud - Paris XI, 2014. English. NNT : 2014PA112217 . tel-01126856

HAL Id: tel-01126856

https://theses.hal.science/tel-01126856v1

Submitted on 6 Mar 2015

UNIVERSITÉ PARIS-SUD

ECOLE DOCTORALE 564 :
PHYSIQUE EN ÎLE-DE-FRANCE

Laboratoire de Physique des Solides

THÈSE DE DOCTORAT

PHYSIQUE

Clément DUTREIX

Impurity and Boundary Modes in the Honeycomb Lattice

Date de soutenance : 26/09/2014

Composition du jury :

Président du jury :	Fabrice MORTESSAGNE	Professeur (Nice Sophia Antipolis)
Directeur de thèse :	Gilles MONTAMBAUX	Professeur (Université Paris-Sud)
Rapporteurs :	David CARPENTIER	Chargé de recherche (ENS Lyon)
	Nuno M. M. R. PERES	Professeur (University of Minho)
Examinateurs :	Cristina BENA	Chargée de recherche (CEA Saclay)
	Jérôme CAYSSOL	Professeur (Université de Bordeaux)
	Jean-Noël FUCHS	Chargé de recherche (Université Pierre et Marie Curie)
Invité :	Frédéric PIÉCHON	Chargé de recherche (Université Paris-Sud)

to Louise, Solange, Alain and Solène

”You become responsible, forever, for what you have tamed”
Antoine de Saint-Exupéry, The Little Prince.

Acknowledgements

Before this three-year PhD, the student I was attended a lot of lectures and some professors probably deserve here a peculiar attention, for they strongly influenced my decision to pursue an academic career in physics. My first introduction to statistical physics, a lecture given by Christian Boulet throughout intensive black-board lectures, was particularly fascinating. The transcendental courses provided by Nicolas Pavloff and Michel Héritier about collective phenomena were also highly stimulating. Finally, the classical and quantum fields theory course, taught by Pascal Simon and Jean-Noël Fuchs - with a special mention for the so-pedagogical tutorials - definitely reinforced my wish to undergo a PhD, additionally to the numerical counterpart that was taught by Werner Krauth in an illuminating series of lectures about Monte Carlo methods.

Next came the PhD. Of course I would like to thank my supervisors first, Gilles Montambaux and Christina Bena, for their kindness and availability, as well as for the useful advice they gave me all along these three years.

Then I naturally spare a thought for the three people I shared the office with. The first one, Ameni Daboussi, was visiting the group as a PhD student when I started working on graphene. She kindly made me benefit from her experience in the field and I am glad we had the opportunity to discuss again during a subsequent stay in the group. I also appreciated a lot sharing the office with the conscientious Doru Sticlet. So many discussions... most of them based on black-board drawn donuts of course, and a memorable one about Leo Kadanoff. I hope we will have time to meet each other again, somewhere in the Netherlands between Delft and Nijmegen. By the way, I have to thank Lih-King Lim for the suggestions he made about my seminar slides, before I gave my first talk in Nijmegen. They turned out to be very useful. Finally, I wish a successful year to Oliver Hijano Cubelos, the third room-mate, who should be about to start (thinking of) the redaction of his manuscript now...

How could I forget to mention the office 164? The lovely sound of high-heel shoes, continuously flowing in the corridor, always ended there... for physical reasons presumably. The lucky men were Rafaël de Gail, Arnaud Raoux, Nicolas Thiébaut and their master student Félix Rose. Maybe I can take the liberty of congratulating Nicolas for teaching the

macroscopic Coulomb screening to the community of experimental physicists in Cargèse. That was such a wonderful experience. Here I would like to mention also Mari-France Mariotto, since she was greatly involved in the organisation of this summer school, as well as in many other conferences. I do not forget Yi Liu, the pétanque prodigy, and his roommate, Jean-René Souquet, especially for his useful comments about distributions theory.

”Fuel for live” was provided in the coffee area where students, postdocs and permanents met each other for the usual coffee break. That was also the occasion to learn some peculiarities of the graphene physics thanks to some pedagogical mini-lectures, relatively to a black board full of hexagons... almost as attractive as the suspicious calendar hanging in the corner. The usual enthusiastic lecturer was the former coffee-dealer, but still coffee addicted, Mark-Oliver Goerbig. His famous ”on monte?” ending some of his mini-lectures regularly led to the sunny terrace for an extra time... and an extra coffee. Olésia, Sébastien, Mircea, Nicolas and the others, you all made that break be a friendly moment.

And so were my Wednesdays, when some researchers competed each other during a soccer game instead of having lunch. Then I am very grateful to Eric Raspaud for introducing me to the LPS football playing team. I have to admit that, even when loosing, provoking or laughing at the opposition with Michel Denis and Michel Mathias was always a pleasure. They also supported me all along these three years and gave me many tricks to be successful in my work. Although they both have a labrador now, I am still glad to join them at la Montagne, Nice or everywhere else, provided there is some ”rasade” for Paulo.

Besides, this thesis obviously results from several collaborations, and I would like to mention Anu Jagannathan, Charis Quay, Marco Aprili and Fabrice Mortessagne for the many hours we spent discussing, sometimes quite early in the morning. Additionally, I would like to address a special ”thank you” to two generous and conscientious researchers, namely Jean-Noël Fuchs and Frédéric Piéchon. Their devotion to science as well as their sharp-mindedness still impress me. I am particularly grateful to Frédéric for sharing his knowledge about topological physics and for introducing me to the symmetry based Fu-Kane argument. It turned out to be very useful in the second chapter of this thesis.

Even if we did not spend a long time working together, I wish all the best to the new comers, Sergueï, Frédédic, Oscar and Yunlong.

The many days I spent at the fresh-doctor Madeny PES institute, developing new elaborated approaches on how apprehending unfair defeats, were as wonderful as the many sweet candies we had. I am glad you manage to achieve your business after I drove you to the airport quite early some mornings. Pippo must be proud of you. All the best in your new American life.

Finally, I wish to thank the main characters involved in any serious decision I take, namely my sister, my parents and my wife, for their unconditional support and attention. You all have been inspiring me for many years now and you keep fueling my life.

"Only two things are infinite, the universe and human stupidity, and I’m not sure about the former"
Albert Einstein

Contents

Introduction

Graphene, the first one-atom thick material discovered in nature, has been isolated only about a decade ago [1], which led the pioneering experimentalists K. Novoselov and A. Geim to the Nobel Prize in 2010. From a crystallographic perspective, the carbon atoms in this graphite layer design a triangular Bravais lattice with a diatomic pattern. This gives rise to an extra degree of freedom in the electronic band structure, which is known as pseudospin. Crucially, the graphene pseudospin reveals massless Dirac electrons at low-energy, whose existence was experimentally confirmed by the observation of the anomalous quantum Hall effect and the presence of zero-energy Landau levels [2, 3]. This offers the possibility to study relativistic quantum phenomena in condensed matter physics. Importantly, it has allowed a direct experimental observation of the Klein tunneling in graphene [4], whereas, in high-energy physics, this effect would not have been tested yet since it was predicted in 1928 [5]. By analogy with the helicity that is based on the 'true' spin in high-energy physics, the pseudospin in graphene also enables the definition of an electronic helicity, or chirality, at low-energy. The chiral nature of the massless Dirac electrons turns out to dramatically affect the quantum interferences induced by defects in this material, by totally suppressing the backscattering [6].

Moreover, the massless Dirac electrons refer to nodal dispersion relations. For this reason, the semimetallic phase they define in graphene can also be considered as an invitation to the world of topological matter. Indeed, the graphene nanoribbons are likely to host zero-energy edge-states [7, 8]. Such boundary modes find a topological origin through a dimensional reduction that consists in an appropriate mapping onto an effective one-dimensional insulating system [9]. More generally, insulators, as well as superconductors, are multi-band gapped systems that are likely to host boundary modes, whose existence depends on topological properties of the bulk band structure. Like graphene, topological matter was born in connection with a quantum Hall effect experiment [10], where the quantised Hall conductance refers to chiral edge-channels [11]. Nevertheless, about twenty more years of pioneering ideas [12–14] have been required, before the interest in topological matter was definitely boosted by the prediction of another kind of quantum Hall effect, namely the quantum spin Hall effect, proposed in 2005 [15].

Topological matter, together with graphene, have certainly received most of the scientific attention in condensed matter physics during the last decade. These two fields of research define the main framework in which the present thesis can be apprehended. It is divided into two parts.

Part I: Impurity and boundary modes in the hexagonal lattice

The first chapter can be considered as an introduction to some aspects of the graphene physics. It begins with the descriptions of the atomic structure and the electronic band structure, before touching on the absence of backscattering due to the chiral nature of the low-energy electrons. It finally introduces the possibility to remove these chiral electrons by opening an energy gap in the spectrum, which defines a Lifshitz transition [16].

The main idea of the second chapter consists in revisiting the impurity-scattering problem, already studied in graphene [17], in the context of the Lifshitz transition. A localised impurity induces quantum interferences in the electronic density of states, which are known as Friedel oscillations [18]. They are directly related to the electronic spectrum, as well as to the pseudospin and the chirality enabled by this extra degree of freedom. After characterising the real-space interferences right at the transition and beyond (where the chiral electrons have been removed and the spectrum gapped), we show that their decaying laws reveal the phase the system belongs to [19].

The case of vacancies, scatterers that imply the existence of a zero-energy impurity-state, is also considered. In this case again, we conclude that the impurity-state decay fully reveals the phase the system belongs to. On top of that, it is qualitatively remarkable that, right at the transition and beyond, all the zero-energy electrons are localised within a triangle, where the wavefunction components appear to be connected to the binomial coefficients of the Pascal triangle [19].

The third chapter deals with topological matter, or more explicitly with topological insulators and superconductors. In such multi-band gapped systems, the ability of electrons to be localised at a boundary depends on symmetry-protected topological properties of the Bloch band structure.

A simple one-dimensional two-band *insulator* is first considered in order to illustrate the connection there exists between the topological characterisation of a gapped band structure, which is protected by symmetry, and the presence of boundary modes that turn out to be zero-energy edge-states. Although this model was introduced a long time ago by Shockley [20] and discussed later on in the literature [21, 22], it was only considered within a nearest-neighbour tight-binding limit. In the present thesis, we analyse the same model when considering arbitrary distant-neighbour hopping processes. This extension allows the system to reach new topological phases that are characterised by an arbitrary large number of edge states.

Nevertheless, it happens that some gapless systems with a nodal dispersion relation, like *semimetals*, also find a topological characterisation via a dimensional reduction, which is illustrated in the case of a zigzag graphene nanoribbon. In this case, we study the persistence of the edge states in the presence of localised disorder [23].

Finally, the chapter ends with the analysis of a two-dimensional eight-band *superconductor*, whose zero-energy boundary modes are Majorana modes [24]. The considered system relies on a honeycomb lattice in the presence of spin-singlet superconductivity, Zeeman splitting and Rashba spin-orbit coupling. So far the literature only focuses on monatomic pattern lattices, or more generally on systems where the topological characterisation does not depend on the spin-orbit interactions. In the case of a honeycomb lattice, which has a diatomic pattern, we show that the magnitude of these interactions directly affects the topological phases. We also give a prescription to access the topological properties of this eight-band system [25], and thus predict the emergence of zero-energy Majorana modes that are localised at the edges of doped and strained nanoribbons.

Part II: Spintronic in mesoscopic superconductors

The fourth chapter, however, is connected neither with graphene, nor with topological matter. It proposes the study of a spin accumulation occurring in an out-of-equilibrium s-wave superconductor. At equilibrium, the superconductor is made of a condensate, i.e. particles coupled by a s-wave pairing, as well as unpaired quasiparticles. Injecting charge- and spin-polarised particles, namely spin-polarised electrons, into the superconductor induces charge and spin imbalances. When the injection stops, it may happen that charge and spin do not relax over the same time-scale. The first experiment that points out such a spin-charge decoupling (charge relaxes much faster than spin) has recently been realised [26].

In order to confirm this chargeless spin-relaxation time, a new experiment has been developed [27], based on measurements in the frequency domain. In the fourth chapter, we address a model that fits the experimental data and thus enables the extraction of this characteristic time [28].

Part I

Impurity and Boundary Modes in the Honeycomb Lattice

Chapter 1

Graphene

The diatomic pattern of the graphene honeycomb lattice is responsible for an extra degree of freedom in the band structure, known as *pseudospin*. In a tight-binding approach, the valence and conduction bands are separated by an energy gap, except at two special momenta in the vicinity of which the dispersion relation is conical. The Fermi surface of undoped graphene simply consists in two Fermi points and the system is said to be semimetallic. Moreover, the low-energy electrons are described by a massless Dirac equation and are characterised by a chirality, defined as the projection of the pseudospin on the momentum direction. This gives rise to unusual quantum phenomena, such as the absence of backscattering. These properties are the focus of the present introductory chapter.

1.1 Atomic structure

Graphene consists of a one-atom-thick layer of graphite, a carbon allotrope. The six electrons of carbon atoms fill orbitals following the Vsevolod Klechkovskii's rule [29] and $1s^2 2s^2 2p_x^1 2p_y^1 2p_z^0$ is the ground state configuration. Carbon-based solids, however, require chemical bondings that are explained by sp hybridisations. In pencil lead graphite, the 2s orbital mixes with two 2p orbitals, for example the $2p_x$ and $2p_y$ ones. Together they form σ covalent bonds that satisfy a trigonal planar geometry, with an interatomic distance $a_0 \simeq 1.42$Å. The remaining $2p_z$ orbitals, which stand perpendicularly to the plan, overlap between nearest neighbours. This is called π-bonding and it permits the involved electrons to move from one orbital to another, explaining the ability of graphite to conduct electricity. Additionally, Van der Waals bonds hold the layers together and build the graphite crystal. This is precisely the weakness of these bonds that makes possible to use graphite to write or to paint, literally *graphein* in Ancient Greek. It also enables graphene exfoliation that can be achieved by applying an adhesive tape onto graphite. Repeating this process leaves fewer and fewer layers after each step, until only one remains... graphene [1].

According to the above description, the σ covalent bonds in graphene build a honeycomb lattice. Crystallography describes it as a triangular Bravais lattice with a diatomic pattern. Such a lattice is illustrated in Fig. 1.1. Of course, the Mermin-Wagner theorem forbids any long-range order in two dimensions [30]. But in a three dimensional world, the formation of out-of-plane ripples, or the presence of a substrate, make the existence of graphene possible. Its dynamical and thermodynamical properties will be ignored in this thesis in which we consider graphene as a rigorously two-dimensional crystal.

Besides, its periodic structure has geometric symmetries, i.e. it maps into itself under isometries. These transformations have a group structure, which defines a point group. The one that characterises graphene symmetries is the dihedral group D_{6h}, following Schönflies notations. This means the lattice and the physical vectors (wavevector, polarisation ...) remain unchanged under six-fold rotations and mirror reflections. A fortiori, the crystal also contains an inversion center. That is why D_{6h} is said to be centrosymmetric.

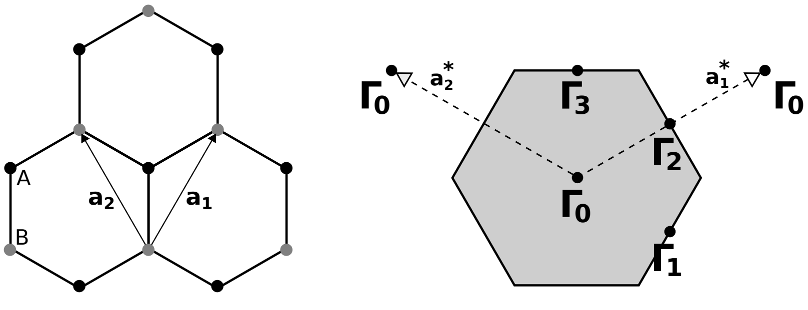

Fig. 1.1 The honeycomb lattice (left) and the hexagonal Brillouin zone (right).

The Bravais lattice invariance under discrete translations naturally leads to the notion of a Brillouin zone in the reciprocal lattice, the two lattices being connected by a Fourier transform. Here, we use an equivalent geometrical prescription to construct this reciprocal lattice. The basis vectors that span the triangular Bravais lattice are labeled $\mathbf{a}_1$ and $\mathbf{a}_2$ in real space. Then, the geometric relations

$$\begin{aligned} \mathbf{a}_1^*.\mathbf{a}_1 &= 2\pi \quad & \mathbf{a}_1^*.\mathbf{a}_2 &= 0 \\ \mathbf{a}_2^*.\mathbf{a}_2 &= 2\pi \quad & \mathbf{a}_2^*.\mathbf{a}_1 &= 0 \end{aligned} \tag{1.1}$$

define $\mathbf{a}_1^*$ and $\mathbf{a}_2^*$, two basis vectors of the reciprocal lattice. From this definition, it is clear that the reciprocal lattice is triangular as well. Actually, this is due to a more general property: if a function satisfies a certain symmetry in real space, so does its Fourier transform in reciprocal space, and vice versa. Indeed, say S represents such a symmetry operator, so that $f[S(\mathbf{r})] = f(\mathbf{r})$. In momentum space

$$\begin{aligned} f[S(\mathbf{q})] &= \int f(\mathbf{r}) e^{-iS(\mathbf{q}).\mathbf{r}} d^2\mathbf{r} \\ &= \int f(\mathbf{r}) e^{-i\mathbf{q}.S^{-1}(\mathbf{r})} d^2\mathbf{r} \\ &= \int f(S(\mathbf{r}')) e^{-i\mathbf{q}.\mathbf{r}'} d^2\mathbf{r}' \\ &= \int f(\mathbf{r}') e^{-i\mathbf{q}.\mathbf{r}'} d^2\mathbf{r}' \\ &= f(\mathbf{q}) \, . \end{aligned} \tag{1.2}$$

We finally introduce the unit cell of the reciprocal lattice, namely the *first Brillouin zone* (BZ). This is the volume inside a surface built from the bisections of segments that connect the origin to the nearest reciprocal-lattice nodes. Of course there also exist second BZs, third ones, and so on. Nevertheless, the problem of free electrons in an infinite crystal can be described in terms of Bloch wavefunctions that have the crystal periodicity. For this reason, the corresponding wavefunctions in momentum space are periodically identical up to a global phase from one BZ to another. That is why only one BZ suffices and by convention one generally picks the first BZ. The hexagonal BZ of the triangular lattice in the reciprocal space is illustrated in Fig. 1.1.

Here we insist on the properties of graphene reciprocal lattice, and on the fact that they stem from the triangular geometry of the Bravais lattice in real space. They do not depend on the hexagonal structure of graphene that involves the diatomic pattern. But, the existence of the two nonequivalent atoms greatly matters when studying the electronic properties of graphene, which is the topic of the next paragraphs.

1.2 Electronic band structure

1.2.1 A two-band description

As previously mentioned, the electronic properties of graphene arise from the π-orbitals filling electrons. They were first investigated in 1947 by the Canadian physicist P. R. Wallace [31], as he was considering graphene as the starting point in the study of graphite. During these wartime years, graphite was indeed being used in nuclear reactors and it was primordial to understand its behaviour under intense neutron and ion bombardment. Like Wallace, we start the study of graphene electronic properties using a tight-binding approximation. Electrons are allowed to hop from one p_z orbital to another. The presence of two nonequivalent atoms, A and B, in the honeycomb lattice leads to two families of p_z electronic orbitals. So two kinds of processes have to be distinguished. On the one hand, there are processes that couple the two distinct sublattices. They are said to be *inter-sublattice* processes. This is the case of nearest-neighbour (NN) and third nearest-neighbour hopping processes for example. On the other hand, there are processes that involve only one sublattice, like next nearest-neighbour (NNN) hopping processes or on-site potentials. One speaks of *intra-sublattice* processes. Although there is no interaction, we write the free-electron Hamiltonian in a second quantised form, which is more compact

$$H = \int_{BZ} d\mathbf{k}\ \psi^{\dagger}(\mathbf{k}) H(\mathbf{k}) \psi(\mathbf{k})\ , \tag{1.3}$$

where the fermionic field $\psi^{\dagger}(\mathbf{k}) = (a^{\dagger}_{\mathbf{k}}, b^{\dagger}_{\mathbf{k}})$ depends on the two-dimensional momentum $\mathbf{k}$ that runs over the BZ. The electronic spin is neglected here and the operator $a_{\mathbf{k}}$ ($b_{\mathbf{k}}$) annihilates an electron on sublattice A (B). The $2{\times}2$ Hamiltonian matrix $H(\mathbf{k})$ is Hermitian and can be expressed in terms of the identity matrix σ_0 and the Pauli matrices

$$\sigma_1 = \begin{pmatrix} 0 & 1 \\ 1 & 0 \end{pmatrix}\ , \quad \sigma_2 = \begin{pmatrix} 0 & -i \\ i & 0 \end{pmatrix}\ , \quad \sigma_3 = \begin{pmatrix} 1 & 0 \\ 0 & -1 \end{pmatrix}\ . \tag{1.4}$$

Therefore, $H(\mathbf{k}) = h_0(\mathbf{k})\sigma_0 + \mathbf{h}(\mathbf{k}).\boldsymbol{\sigma}$, with $\boldsymbol{\sigma} = (\sigma_1, \sigma_2, \sigma_3)$ and $\mathbf{h} = (h_1, h_2, h_3)$. The diagonal components h_0 and h_3 refer to intra-sublattice processes, whereas the off-diagonal components h_1 and h_2 refer to inter-sublattice processes. The spectrum is composed of two bands defined by $E_{\pm}(\mathbf{k}) = h_0(\mathbf{k}) \pm |h(\mathbf{k})|$. The term linear in the identity matrix is $\mathbf{k}$-dependent, and thus is not just a constant that one could remove to fix the zero energy. It breaks the *particle-hole symmetry* (PHS) since $E_{+}(\mathbf{k}) \neq -E_{-}(-\mathbf{k})$. Even so, this term is irrelevant when dealing with the eigenstates and we restrict our description to a particle-hole symmetric Hamiltonian

$$H(\mathbf{k}) = \mathbf{h}(\mathbf{k}).\boldsymbol{\sigma}. \tag{1.5}$$

The electronic dispersion relation is now given by $E_{\pm}(\mathbf{k}) = \pm|\mathbf{h}(\mathbf{k})|$. The valence and conduction bands, namely E_{-} and E_{+}, simply refer to negative and positive energies respectively.

The Hamiltonian matrix (1.5) formally reminds us of a spin-1/2 ($\boldsymbol{\sigma}$) in a magnetic field ($\mathbf{h}$) that periodically depends on the momentum. The *pseudospin* precisely corresponds to this extra degree of freedom. It directly arises from the existence of the two sublattices and thus relates to the real space. By analogy with a 'true' spin-1/2, we can give a geometrical representation of the vector $\mathbf{h}$ on the Bloch sphere, also called the Riemann sphere. Let us fashion the Hamiltonian matrix this way,

$$H(\mathbf{k}) = \pm|\mathbf{h}(\mathbf{k})| \begin{pmatrix} \cos\phi_{\mathbf{k}} & \sin\phi_{\mathbf{k}}\, e^{-i\theta_{\mathbf{k}}} \\ \sin\phi_{\mathbf{k}} e^{i\theta_{\mathbf{k}}} & -\cos\phi_{\mathbf{k}} \end{pmatrix} . \tag{1.6}$$

Defining the angles $\theta_{\mathbf{k}}$ and $\phi_{\mathbf{k}}$ is possible as long as the modulus of the vector $\mathbf{h}$ is non-zero, or, in other words, as long as the two bands E_+ and E_- remain non-degenerate and the spectrum gapped. Such a degeneracy concerns the Bloch sphere center ($|\mathbf{h}| = 0$). The projection of the vector $\mathbf{h}$ onto the sphere of radius 1, namely $\mathbf{h}/|\mathbf{h}|$, is depicted in Fig. 1.2. The eigenstates of (1.6) are equivalent to

$$|\psi_+(\mathbf{k})\rangle = \frac{1}{\sqrt{2}} \begin{pmatrix} \cot\frac{\phi_{\mathbf{k}}}{2} e^{-i\theta_{\mathbf{k}}} \\ 1 \end{pmatrix} , \quad |\psi_-(\mathbf{k})\rangle = \frac{1}{\sqrt{2}} \begin{pmatrix} \cot\frac{\phi_{\mathbf{k}}+\pi}{2} e^{-i\theta_{\mathbf{k}}} \\ 1 \end{pmatrix} . \tag{1.7}$$

Their evolution is ruled by Schrödinger or Dirac equations that are linear. So two eigenstates that differ from each other by a complex constant are equivalent and can be written under the form (1.7). The state $|\psi_+\rangle$ (or equivalently $|\psi_-\rangle$) consequently defines an equivalence class for any eigenstate in the two-dimensional complex Hilbert space $\mathscr{H} = \mathbb{C}^2$. From (1.7), every equivalence class is characterised by a complex number $z = \cot\frac{\phi_{\mathbf{k}}}{2} e^{-i\theta_{\mathbf{k}}}$, which is actually the stereographic projection of $\mathbf{h}(\mathbf{k})/|\mathbf{h}(\mathbf{k})|$ onto the complex plan. There exists a

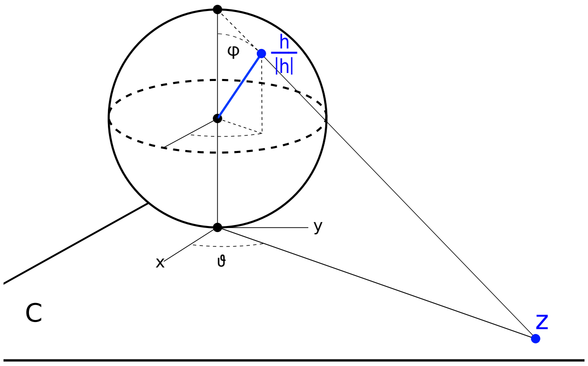

Fig. 1.2 Geometrical representation of the vector $\mathbf{h}/|\mathbf{h}|$ on the Bloch sphere and its stereographic projection onto the complex plane.

one-to-one correspondence between any points of the Bloch sphere and the complex plane, except the north pole maps away to the infinity. This is the reason why the projective space of the Hilbert space $\mathbb{C}^2$ is a two-dimensional sphere.

Besides, the evolution of vector $\mathbf{h}$, or equivalently the evolution of z, is crucial when dealing with the topological properties of such a two-band system [13, 32]. The topological properties of gapped Hamiltonians will be discussed in the third chapter of this thesis, but we just mention here the main idea for such a two-band description. As long as there exists an energy gap in the spectrum ($|\mathbf{h}| \neq 0$), it is possible to define an integer that counts the number of times the vector $\mathbf{h}/|\mathbf{h}|$ wraps the Bloch sphere when the momentum runs over the whole BZ. This integer gives the number of zero-energy modes that live at a boundary between two topologically distinct systems, which means two systems characterised by distinct wrapping numbers. This idea can be generalised to systems described by more than two energy bands, a case that we will encounter in the third chapter.

Moreover, if we take into account only inter-sublattice processes, then $h_0 = h_3 = 0$ and the system is said to be bipartite. It means the Hamiltonian matrix (1.5) anticommutes with σ_3

$$\{H(\mathbf{k}), \sigma_3\} = 0 \, . \tag{1.8}$$

This defines the so-called *sublattice symmetry* (SLS), also named chiral symmetry, and requires the vector $\mathbf{h}/|\mathbf{h}|$ to evolve along the equator of the Bloch sphere ($\phi_{\mathbf{k}} = \pi/2$). This anticommutation relation necessarily implies the PHS, meaning $E_+(\mathbf{k}) = -E_-(\mathbf{k})$. We will have the opportunity to discuss this symmetry in more detail in the two next chapters. Regarding the Bloch eigenstates defined in (1.7), they reduce to

$$|\psi_\pm(\mathbf{k})\rangle = \frac{1}{\sqrt{2}} \begin{pmatrix} 1 \\ \pm e^{i\theta_{\mathbf{k}}} \end{pmatrix} . \tag{1.9}$$

Of course they cannot wrap the entire Bloch sphere anymore under the SLS, and there is no interesting topological property in the sense it has been defined above. Nevertheless, topology is etymologically defined as the study ('logos') of surfaces ('topos'). Then one can similarly consider a one-dimensional closed surface described by $\mathbf{k}$ in the BZ, and count the number of times $\mathbf{h}/|\mathbf{h}|$ wraps the Bloch sphere equator. Such a consideration actually turns out to be relevant to explain the zero-energy edge states of graphene [33, 34], as well as the zero-energy Landau levels [2, 35, 36], whose existence is essentially based on the evolution of the phase $\theta_{\mathbf{k}}$ along a periodic path in the BZ. This phase also contains information about the chiral nature of the low-energy electrons in graphene, which is responsible for the absence of backscattering in this material [37].

1.2.2 Massless Dirac electrons

To be more specific, let us determine the low-energy band structure of graphene à la Wallace. First, we consider a tight-binding Hamiltonian that takes into account NN and NNN hopping processes

$$H = \sum_{\langle i,j \rangle} t(a_i^\dagger b_j + b_j^\dagger a_i) + \sum_{\langle\langle i,j, \rangle\rangle} t'(a_i^\dagger a_j + b_i^\dagger b_j) \ , \tag{1.10}$$

where the indices i and j label the unit cell. The first sum runs over the three NN, while the second sum runs over the six NNN. The corresponding hopping amplitudes would be estimated as $t \simeq 2.97eV$ and $t' \simeq 0.073eV$ respectively [38].

Before determining the band structure relative to the 2×2 Hamiltonian matrix $H(\mathbf{k})$, a few remarks are in order. They concern the Fourier transform definitions, or equivalently the description one chooses for the hexagonal lattice. First, the honeycomb lattice can be thought of as a triangular Bravais lattice with a diatomic pattern. In that case the Fourier transform reads

$$a_i = \int_{\mathbf{k}\in BZ} e^{i\mathbf{k}.\mathbf{R}_i} a_k \ , \quad b_i = \int_{\mathbf{k}\in BZ} e^{i\mathbf{k}.\mathbf{R}_i} b_k \ , \tag{1.11}$$

with $\mathbf{R}_i$ a vector of the triangular Bravais lattice corresponding to the unit cell i. Second, the honeycomb lattice can be described as a superposition of two triangular sublattices A and B, and

$$a_i = \int_{\mathbf{k}\in BZ} e^{i\mathbf{k}.\mathbf{R}_{Ai}} \tilde{a}_k \ , \quad b_i = \int_{\mathbf{k}\in BZ} e^{i\mathbf{k}.\mathbf{R}_{Bi}} \tilde{b}_k \ , \tag{1.12}$$

where $\mathbf{R}_{Ai}$ and $\mathbf{R}_{Bi} = \mathbf{R}_{Ai} + \boldsymbol{\delta}_3$ are two vectors specifying the position of the atoms A and B in unit cell i. Here $\boldsymbol{\delta}_3$ denotes the NN vector inside a given unit cell. Consequently, intra-sublattice processes are equal in both descriptions, whereas inter-sublattice processes are not. In our case, the NNN hopping process remains unchanged in both descriptions and

$$h_0(\mathbf{k}) = 2t'[\cos(\mathbf{k}.\mathbf{a}_1) + \cos(\mathbf{k}.\mathbf{a}_2) + \cos(\mathbf{k}.(\mathbf{a}_1 - \mathbf{a}_2))] \ . \tag{1.13}$$

The NN hopping term however depends on the Fourier transform definition we choose. It reads

$$h_1(\mathbf{k}) + ih_2(\mathbf{k}) = t(1 + e^{i\mathbf{k}.\mathbf{a}_1} + e^{i\mathbf{k}.\mathbf{a}_2}) \tag{1.14}$$

in the first description, whereas it is given by

$$\begin{aligned} h_1(\mathbf{k}) + ih_2(\mathbf{k}) \to \tilde{h}_1(\mathbf{k}) + i\tilde{h}_2(\mathbf{k}) &= t(e^{i\mathbf{k}.\boldsymbol{\delta}_1} + e^{i\mathbf{k}.\boldsymbol{\delta}_2} + e^{i\mathbf{k}.\boldsymbol{\delta}_3}) \\ &= t(e^{i\mathbf{k}.\mathbf{a}_1} + e^{i\mathbf{k}.\mathbf{a}_2} + 1)e^{i\mathbf{k}.\boldsymbol{\delta}_3} \\ &= f_1(\mathbf{k})e^{i\mathbf{k}.\boldsymbol{\delta}_3} \end{aligned} \tag{1.15}$$

in the second description. Here $\boldsymbol{\delta}_{i=1,2,3}$ are the NN vectors. Of course, $|\mathbf{h}| = |\tilde{\mathbf{h}}|$ and the two descriptions yield the same spectrum. Nevertheless, it turns out that one description can be more convenient than the other. For example, the first description makes the Hamiltonian matrix periodic in momentum space, which means $H(\mathbf{k}+\mathbf{G}) = H(\mathbf{k})$, with $\mathbf{G}$ a vector of the reciprocal lattice. From relation (1.15), it is clear that the Hamiltonian matrix is no longer periodic in the second representation. Indeed it explicitly takes into account the relative atomic positions via the NN vectors. For a more detailed discussion about this representation problem, the reader can refer to [39].

Let us choose the first representation and determine the dispersion relation of graphene. In the limit $t' \ll t$, which is a reasonable assumption given the respective values of these parameters, the bipartite system has a particle-hole symmetric spectrum. The valence and conduction bands are separated by an energy gap a priori, since $E_\pm(\mathbf{k}) = \pm|\mathbf{h}(\mathbf{k})|$, but the spectrum turns out to be degenerate right at the corners of the BZ where the two energy

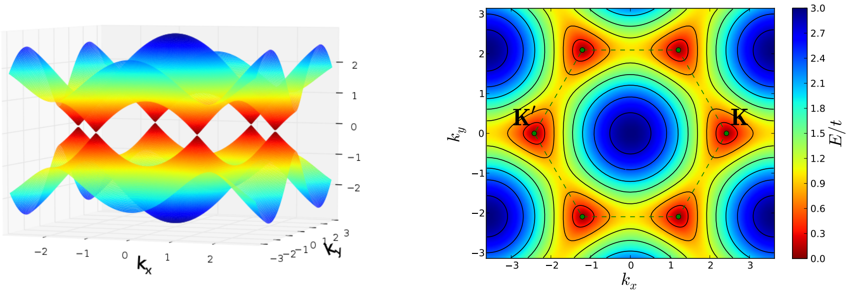

Fig. 1.3 Spectrum of the honeycomb lattice (left) and its projection onto the BZ (right) in a nearest-neighbour tight-binding approximation. The red areas characterise the Dirac cones arising at low-energy in the two nonequivalent valleys K and K'. The green dashed lines depict the BZ.

bands touch each other. The two nonequivalent corners of the BZ are defined by

$$K_\xi = \xi \frac{\mathbf{a}_1^* - \mathbf{a}_2^*}{3} + m\,\mathbf{a}_1^* + n\,\mathbf{a}_2^*, \tag{1.16}$$

where m and n are two integers. One also speaks about valleys, each one being labeled by a valley index ξ. Expanding the Hamiltonian matrix in their vicinity leads to

$$H(\mathbf{K}_\xi + \mathbf{q}) \simeq v_F \begin{pmatrix} 0 & -\xi q_x - iq_y \\ -\xi q_x + iq_y & 0 \end{pmatrix} \tag{1.17}$$

and the energy bands are given by

$$E_\pm(\mathbf{K}_\xi + \mathbf{q}) \simeq \pm v_F |\mathbf{q}| \tag{1.18}$$

with $v_F \simeq 10^6 m.s$ the Fermi velocity. It means the dispersion relation is conical around each valley, which describes relativistic fermions. The two nonequivalent Dirac cones are illustrated by the red areas in Fig. 1.3. In other words, the low-energy modes are described by massless Dirac equations when expressing the momentum operator in the position representation $\left(q_{x(y)} \rightarrow -i\partial_{x(y)}\right)$ in the Hamiltonian matrix (1.17). The Fermi surface of undoped graphene consists of two Fermi points that correspond to the corners of the BZ. These nodal points allow one to describe graphene as a two-dimensional semimetal.

1.2.3 Chirality and absence of backscattering

More interestingly, the graphene massless Dirac electrons are also chiral, a property that directly emanates from the pseudospin, and that is encoded in the phase $\theta_\mathbf{k}$ defined in (1.9). Indeed, the Hamiltonian matrix (1.17) can be re-written as

$$H(\mathbf{K}_\xi + \mathbf{q}) \sim \mathbf{q}.\boldsymbol{\sigma}, \tag{1.19}$$

where $\mathbf{q} = (-\xi q_x, q_y, 0)$. So the matrix $H(\mathbf{k})$ commutes with the chiral operator

$$C = \frac{\mathbf{q}.\boldsymbol{\sigma}}{|\mathbf{q}|} = \begin{pmatrix} 0 & e^{-i\theta_\mathbf{q}} \\ e^{i\theta_\mathbf{q}} & 0 \end{pmatrix}, \tag{1.20}$$

defined as the projection of the pseudospin onto the momentum. This implies that the chirality (helicity), given by the eigenvalues of this operator (±1), is a conserved quantity *within a given valley* and the pseudospin is either parallel or antiparallel to the momentum. An important consequence of the chirality is the absence of backscattering that was already mentioned in connection with carbon nanotubes in [6], where a rigorous demonstration can be found, as well as in [40], for the case of a large-scale potential. Here we simply touch on this effect in a more intuitive way [40], which is sufficient to point out the pseudospin effects. Consider a weak extended impurity potential $V(\mathbf{r}).\sigma_0$. This does not act on the pseudospin (σ_0) and it does not couple the distinct valleys in momentum space. The first order Born approximation connects the Fourier transform of this potential to the following scattering probability

$$\begin{aligned} P(\mathbf{q},\mathbf{q}') &\sim |V(\mathbf{q}'-\mathbf{q})|^2 \left|\langle \psi_\pm(\mathbf{q}')|\psi_\pm(\mathbf{q})\rangle\right|^2 \\ &\sim |V(\mathbf{q}'-\mathbf{q})|^2 \left|\frac{1+e^{\theta_\mathbf{q}-\theta_{\mathbf{q}'}}}{2}\right|^2 . \end{aligned} \tag{1.21}$$

In the case of backscattering, the incident and outgoing massless Dirac electron wavevectors satisfy $\mathbf{q}' = -\mathbf{q}$. Additionally, $\theta_{-\mathbf{q}} = \theta_\mathbf{q} + \pi$ so that the extra term due to the pseudospin in (1.21) vanishes. The scattering probability is rigorously zero in the case of backscattering regardless of the impurity potential term $V(2\mathbf{q}')$. In other words, this process requires the electrons to reverse the direction of propagation, whereas the impurity potential does not act on the pseudospin, which cannot be modified. This is the reason why backscattering is totally suppressed in graphene. This effect also enables incoming electrons with a normal incidence to tunnel as holes through a barrier potential with a transmission probability $t = 1$, which is known as Klein tunneling [4, 5, 37].

The case of short-range impurities, which allow inter-valley scattering, is what the next chapter focuses on. Again, it turns out that the quantum interferences 'suffer' the consequences of the pseudospin existence and of the backscattering suppression.

1.3 Lifshitz transition

1.3.1 Fermi points protection

Before moving to the scattering problem of localised impurities in two dimensions, we would like to say a few words about the robustness of the chiral massless Dirac fermions against perturbations, since they are the source of the striking properties that have been mentioned so far. Two discrete symmetries [41], namely the time-reversal symmetry (TRS) and the inversion symmetry, guarantee the robustness of conical points. They respectively acts on the Hamiltonian matrix as

$$\begin{aligned} T &: H(\mathbf{k}) = H^*(-\mathbf{k}) \\ I &: H(\mathbf{k}) = \sigma_1 H(-\mathbf{k}) \sigma_1 \ . \end{aligned} \tag{1.22}$$

The time-reversal symmetry requires the dispersion relation to fulfil $E(\mathbf{k}) = E(-\mathbf{k})$, which makes the Dirac cones come in pairs. The inversion symmetry reverses the coordinates in real space and also exchanges the A and B sublattices. Consider a general Hamiltonian matrix

$$H(\mathbf{k}) = \sum_{i=0}^{3} h_i(\mathbf{k}) \sigma_i \ , \tag{1.23}$$

then the space-time inversion TI implies the mass term h_3 to be zero. It means the Dirac cones are stable with respect to perturbations that would not break any of these two discrete symmetries. This is the case, for example, when taking into account the NNN hopping processes. As already mentioned, such processes are described by the identity operator σ_0. This breaks the SLS and shifts the energy of the Fermi points without opening any energy gap. In order to open an energy gap, one can for example consider a constant mass term $h_3(\mathbf{k}) = \mu$. Such an alternating on-site potential would make the two sublattices nonequivalent, breaking the inversion symmetry. This situation arises in the tight-binding description of electrons in the boron nitride hexagonal lattice. An other way to gap the spectrum consists in breaking the TRS by adding fluxes to the NNN hopping processes, such that there is no net magnetic flux in the unit cell. This is the idea of the so-called Haldane model [13]. Since it breaks the TRS, the Dirac cones, which are not symmetry protected, do not have to come in pairs.

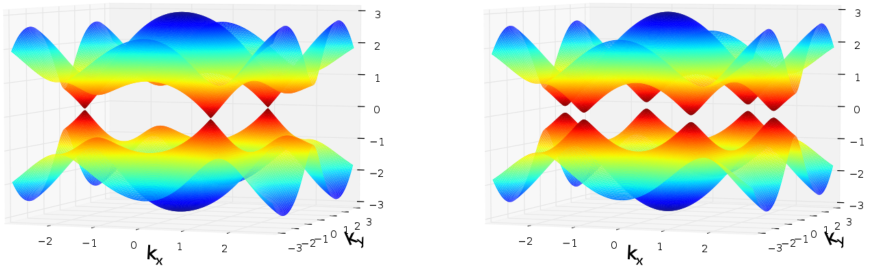

Fig. 1.4 Dispersion relations in the case of the Haldane model (left) and in the case of the boron nitride (right).

In the two $\pm\mathbf{K}$ valleys indeed, the mass term is given by $h_3(\pm\mathbf{K}) = \mu \pm 3\sqrt{3}\, t' \sin\phi$, where ϕ denotes the flux relative to the NNN hopping processes. So there exists a configuration for which the mass term vanishes in a single valley only, which yields a dispersion relation with a single Dirac cone (see Fig. 1.4).

Even in the absence of a mass term (h_3=0), and without breaking the TRS and the inversion symmetry, there actually exists another way to open an energy gap in the spectrum. It comes from the fact that the Dirac points also support a topological characterisation [42]. When the momentum describes a closed path $\mathscr{C}$ in momentum space the equivalence class of the Bloch wavefunctions defined in (1.9) can wind around the Bloch sphere equator. The winding number W of this mapping characterises nonequivalent paths $\mathscr{C}$ that cannot be continuously deformed into each other. It is related to the Berry phase [12] (right-hand side term in the equation below) by

$$\begin{aligned} 2\pi\, W(\mathscr{C}) &= -i \oint_{\mathscr{C}} d\mathbf{k}\, \langle \psi_\pm(\mathbf{k}) | \nabla_\mathbf{k} \psi_\pm(\mathbf{k}) \rangle \\ &= \oint_{\mathscr{C}} d\mathbf{k}\, \nabla_\mathbf{k} \theta_\mathbf{k}\, . \end{aligned} \tag{1.24}$$

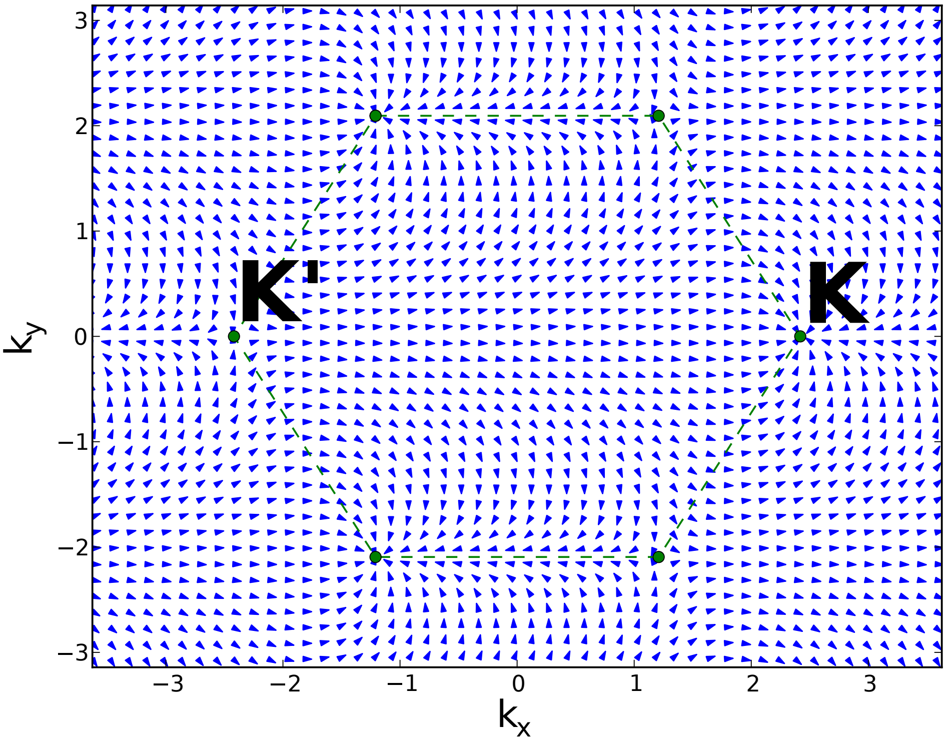

Fig. 1.5 Behaviour of the Bloch spinor phase θ_k in the BZ.

The topological invariant W cannot change except if the phase $\theta_{\mathbf{k}}$ becomes ill-defined, which occurs right at the conical points at the corners of the BZ, where the phase exhibits vortices (Fig. 1.5). From the low-energy expansion (1.19), this phase is defined as $\theta_{\mathbf{q}} = \arctan(\xi q_y/q_x)$ in the valley $\mathbf{K}_\xi$, so that the two nonequivalent valleys have opposite winding numbers and opposite Berry phases. Therefore, the paths $\mathscr{C}_\xi$ that enclose once the conical point referring to valley $\mathbf{K}_\xi$ are topologically equivalent, for they are characterised by the same invariant $W(\mathscr{C}_\xi) = \xi$. Through this characterisation, the Dirac cones appear to be topologically protected. Nevertheless, and because the two nonequivalent cones are characterised by opposite invariants, the interesting situation arises if the two cones merge, a situation which does not require breaking the TRS and the inversion symmetry. In that case, the vortex and the anti-vortex in the phase $\theta_{\mathbf{k}}$ annihilate each other, which describes the absence of Dirac cone in the BZ $\big(W(\mathscr{C}) = 0$ for any path $\mathscr{C}\big)$. Note finally that such a merging can only occur at time-reversal invariant points $\mathbf{\Gamma}_i$ (see Fig. 1.1), since they satisfy $E(\mathbf{\Gamma}_i) = E(-\mathbf{\Gamma}_i)$. Indeed they are defined as $\mathbf{\Gamma}_i = -\mathbf{\Gamma}_i + \mathbf{G}$ with $\mathbf{G}$ a Bravais lattice vector. Otherwise, the TRS requires the existence of two conical points in the BZ, as previously mentioned.

1.3.2 Dirac-cone merging transition

Thus, the Dirac-cone merging offers a third possibility to destroy the Dirac cones, even in the presence of the TRS and inversion symmetry. The coincidence between the Dirac points (determined by the band structure) and that of the corners of the BZ (intrinsic to the Bravais lattice) occurs only when the three NN hopping amplitudes are equal [43]. Let us consider one of the three NN hopping amplitudes as variable, say the one within the lattice unit cell defined by the basis vectors $\mathbf{a_1}$ and $\mathbf{a_2}$ (see Fig. 1.1). This tunable amplitude is denoted t' and could simulate a uniform strain applied to the graphene sheet. Fig. 1.6 illustrates the fact that the two nonequivalent Dirac cones move away from the corners of the BZ when

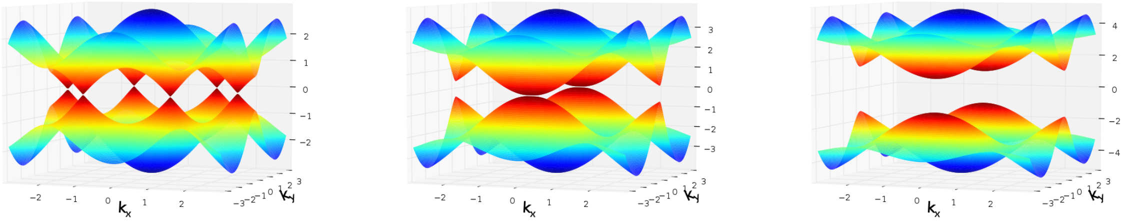

Fig. 1.6 Dispersion relation for $t' = t$, $t' = 2t$ and $t' = 3t$ (from left to right).

varying this tunable parameter. Increasing the amplitude t' from t to $2t$ makes the two Dirac points merge at momentum $\mathbf{\Gamma}_3$. The critical value $t' = 2t$ corresponds to the annihilation of a pair of Dirac points with opposite winding numbers, or equivalently, with opposite Berry phases. The Dirac cone merging defines a transition between a semimetallic phase and an insulating one, since a gap opens at $\mathbf{\Gamma}_3$ for $t' > 2t$.

This can be shown when expanding the Hamiltonian matrix in the vicinity of this momentum [44]

$$H(\mathbf{\Gamma}_3 + \mathbf{q}) \simeq \begin{pmatrix} 0 & \Delta + \frac{q_x^2}{2m^*} - ic_y q_y \\ \Delta + \frac{q_x^2}{2m^*} + ic_y q_y & 0 \end{pmatrix}, \tag{1.25}$$

where $c_y = 3ta_0$, $2m^* = \frac{4}{3ta_0^2}$, and $\Delta = t' - 2t$ characterises the distance from the transition and also gives the value of the gap when $t' > 2t$. Exactly at the transition ($\Delta = 0$), the Hamiltonian exhibits a semi-Dirac energy dispersion [45] such that the spectrum is linear in q_y but quadratic with respect to q_x

$$E_\pm(\mathbf{\Gamma}_3 + \mathbf{q}) = \pm\sqrt{(c_y q_y)^2 + \left(\frac{q_x^2}{2m^*}\right)^2}. \tag{1.26}$$

Please note that the critical value of the strain magnitude ($t' = 2t$) is not experimentally achievable in graphene [46]. However the Dirac-cone merging transition has already been observed in the context of artificial lattices [47–49]. This transition consisting in the annihilation of the two conical points, and corresponding to a change in the Fermi surface topology, defines a Lifshitz transition [16], with reference to the work Lifshitz realised together with Kaganov in relation to the thermodynamical properties of electrons in metals under pressure.

Chapter 2

Impurity scattering

This chapter mainly discusses *Friedel oscillations*, or equivalently quantum interferences, induced by short-range impurities in the local density of states (LDOS). It covers the two-dimensional cases of nonrelativistic electrons, massless Dirac electrons and semi-Dirac electrons. The problem is apprehended through a T-matrix approach and simple lattice considerations. It highlights the possibility to use impurity scattering as a real space probe of the Dirac-cone merging transition.

2.1 Friedel oscillations in the very beginning

These oscillations were first introduced in the 1950's by Jacques Friedel in a study of alloys electronic structure [18]. The principal idea, addressed in that work, concerns the behaviour of conduction electrons when a localised charge is introduced in an interstitial or substitutional position. This many-body problem cannot be understood neither in a simple Hartree-Fock approximation (mean field theory), nor in a perturbation theory since the long-range electron-electron interactions lead to divergences to all orders. It is actually necessary to take into account the rearrangement of the electron gas, as a response to the usual Coulomb potential $V(\mathbf{q}) = e^2/\mathbf{q}^2$, where $\mathbf{q}$ is a three-dimensional momentum. Such a response is well described by the following Dyson equation

$$\tilde{V}(\mathbf{q},\omega) = V(\mathbf{q}) + V(\mathbf{q})\Pi(\mathbf{q},\omega)\tilde{V}(\mathbf{q},\omega) \ , \tag{2.1}$$

where $\tilde{V}$ is the renormalised Coulomb interaction. It now depends on the frequency ω, for there are retardation effects. The lowest diagrammatic expansion of the response function

Π, sometimes called polarisation operator, leads to the Lindhard function

$$\Pi_0(\mathbf{q},\omega) \sim \int d^3k \frac{f(\varepsilon_{\mathbf{k}}) - f(\varepsilon_{\mathbf{k+q}})}{\omega - (\varepsilon_{\mathbf{k}} - \varepsilon_{\mathbf{k+q}}) + i\delta} , \tag{2.2}$$

where f is the Fermi distribution, ε the free-electron dispersion relation, and the imaginary part δ is the quasiparticle life-time. This approximation is known as the Random Phase Approximation (RPA). Then, the static potential is obtained when $\omega = 0$. First, Thomas and Fermi computed the integral (2.2) in the limit $\mathbf{q} \to 0$. It results in the following Yukawa potential [50]

$$\tilde{V}(r) \sim \frac{e^2}{r} e^{-k_D r} , \tag{2.3}$$

where r is the distance to the localised charge added in the electron gas. The exponential implies that the long-range Coulomb interaction is screened over the characteristic Debye length $1/k_D$.

Nevertheless, the Thomas-Fermi approximation is not sufficient. It is a long wavelength approximation, so it is likely to miss some effects in the electron gas response to the short-range perturbation. This is what happens indeed, and it can be understood from the integral (2.2). When $\omega = 0$ in the denominator, there are also divergences, i.e. poles that contribute to the integral and are missed in the Thomas-Fermi approximation. Such divergences occur here when $\varepsilon_{\mathbf{k}} = -\varepsilon_{\mathbf{k+q}}$, which is known as nesting. The nesting provokes instabilities in the Fermi surface and it is responsible for fundamental phenomena such as the Peierls transition, charge and spin density waves, as well as BCS superconductivity. As far as we are concerned, the spectrum is parabolic and two Fermi surfaces locally nest together with a translational vector $q = 2k_F$, where k_F is the Fermi momentum. This gives rise to a long-range oscillating term, namely

$$\tilde{V}(r) \sim \frac{\cos(2k_F r)}{r^3} . \tag{2.4}$$

The modulations it induces in the spatial electronic density are precisely the Friedel oscillations. This effect also appears when dealing with spins instead of charges. The electronic response function to a magnetic impurity exhibits divergences for wavevectors $q = 2k_F$. It results in an oscillating long-range magnetic interaction that spatially behaves as (2.4) [51].

Therefore, the $2k_F$ oscillations turn out to emanate from a nesting property of Fermi surfaces, instead of the screening effect that refers to the long-range Coulomb interaction.

2.2 T-matrix approximation

2.2.1 Diagrammatic formalism

The impurity problem addressed in this thesis deals with non-interacting electrons, in contrast with the original Friedel's work we have just discussed. Nevertheless, it still reveals Friedel oscillations, i.e. $2k_F$-wavevector spatial modulations related to a nesting property of Fermi surfaces. The considered localised impurities are neither charged nor magnetic. Any of them can be represented by the potential $V(\mathbf{r}) = V_0\delta(\mathbf{r})$ in real space, whose Fourier transform is only a constant term, V, in momentum space. Besides, the impurity cannot pump any energy from the electronic background, which describes an elastic scattering. Of course, impurity scattering does not conserve the momentum. Any incoming electron with momentum $\mathbf{k}$ is scattered away with momentum $\mathbf{k}'$. Fig. 2.1 gives a diagrammatic perturbative representation to all orders in the impurity scattering. It leads to the following Dyson equation for the T-matrix

$$T(\mathbf{k_1},\mathbf{k_2},i\omega) = V(\mathbf{k_1},\mathbf{k_2}) + \int d\mathbf{k}'\, V(\mathbf{k_1},\mathbf{k}')G_0(\mathbf{k}',i\omega)T(\mathbf{k}',\mathbf{k_2},i\omega) \tag{2.5}$$

where $i\omega_n$ are the Matsubara frequencies. The bare Green's function is defined from the Hamiltonian in momentum space by $G_0(\mathbf{k},i\omega_n) = [i\omega_n - H_\mathbf{k}]^{-1}$. Remember that the impurity potential is independent of the momentum, which greatly simplifies the calculation of the T-matrix. Indeed, it is just a geometric series, so the infinite summation of diagrams can be performed exactly. It results in

$$T(i\omega_n) = [1 - V\int d\mathbf{k}'G_0(\mathbf{k}',i\omega_n)]^{-1}V\ . \tag{2.6}$$

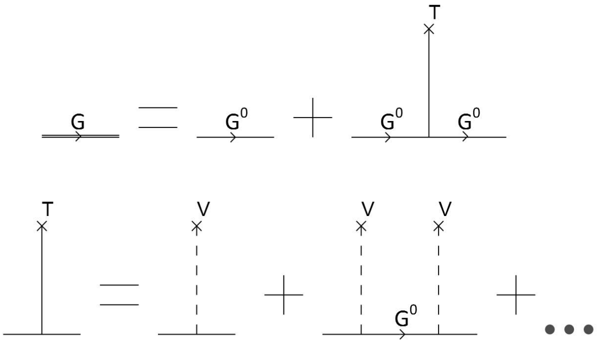

Fig. 2.1 Diagrammatic perturbative expansion of the generalised Green's function to all orders in the impurity potential.

From Fig. 2.1, it follows that the retarded generalised Green's function, obtained by analytical continuation $i\omega_n \to \omega + i\delta$, reads

$$G(\mathbf{r_1}, \mathbf{r_2}, \omega) = G_0(\mathbf{r_1} - \mathbf{r_2}, \omega) + G_0(\mathbf{r_1}, \omega) T(\omega) G_0(-\mathbf{r_2}, \omega) \ . \tag{2.7}$$

When an electron is added to the system at position $\mathbf{r_2}$ with a given energy ω, it is likely to be scattered by the impurity once, twice, ... or not at all. By taking all these possibilities into account, the generalised Green's function simply expresses the probability amplitude to find this electron with the same energy ω (elastic process) at position $\mathbf{r_1}$. This function contains information about the spectrum, as well as about a lot of thermodynamical measurable quantities. The measurable quantity we are interested in here is the *local density of states* (LDOS). It gives a spatial representation of the electronic density at a certain energy. We would like to determine how the LDOS changes in the presence of a localised impurity. On the right-hand side of equation (2.7), the first term describes how the electrons propagate in the absence of any impurity, which is not qualitatively relevant. This is the reason why we define $\Delta G = G - G_0$ as the correction to the bare Green's function. Then, the correction to the LDOS in real space, due to the impurity, is given by

$$\Delta\rho(\mathbf{r}, \omega) = -\frac{1}{\pi} Im[Tr\, \Delta G(\mathbf{r}, \mathbf{r}, \omega)] \ . \tag{2.8}$$

If the quantum interferences arising from elastic scattering can be probed with an atomic-scale spatial resolution in scanning tunneling microscopy experiments [52], its Fourier transform is meaningful too. The LDOS correction in momentum space can be written as

$$\Delta\rho(\mathbf{q}, \omega) = \frac{i}{2\pi} \int d\mathbf{k}\ [\Delta G(\mathbf{k} + \mathbf{q}, \mathbf{k}, \omega) - \Delta G^*(\mathbf{k}, \mathbf{k} + \mathbf{q}, \omega)] \ . \tag{2.9}$$

2.2.2 Application to graphene

Since there are two nonequivalent atoms per unit cell in graphene, the impurity potential and the bare Green's function are 2×2 matrices

$$V = V_0 \delta(\mathbf{r}) \frac{\sigma_0 + \sigma_3}{2}, \quad G_0 = \begin{pmatrix} G_{0,AA} & G_{0,AB} \\ G_{0,BA} & G_{0,BB} \end{pmatrix} \ . \tag{2.10}$$

The above potential matrix describes an impurity that breaks the symmetry between the two sublattices by being localised at the origin, on the sublattice A. The discussion is also limited to a repulsive potential ($V_0 > 0$), but the case of an attractive potential can be retrieved when reversing all energy signs. Furthermore, G_0 refers to the unperturbed system where the two sublattices are equivalent, so $G_{0,AA} = G_{0,BB}$. Now we derive some relations, rather practical than conceptual, in order to compute the LDOS and its Fourier transform, both numerically and analytically.

First of all, we establish a connection between the Green's function defined in the continuum and the discrete ones defined in terms of the lattice-site coordinates. The Bloch wavefunctions $\psi_{A,\mathbf{k}}(\mathbf{r}) = u_{A,\mathbf{k}}(\mathbf{r})e^{i\mathbf{k}.\mathbf{r}}$ and $\psi_{B,\mathbf{k}}(\mathbf{r}) = u_{B,\mathbf{k}}(\mathbf{r})e^{i\mathbf{k}.\mathbf{r}}$ are the eigenstates of the one-body Hamiltonian. They have the lattice periodicity, since $u_{A,\mathbf{k}}(\mathbf{r}+\mathbf{R}) = u_{A,\mathbf{k}}(\mathbf{r})$ with $\mathbf{R}$ a Bravais lattice vector, and the same for $u_{B,\mathbf{k}}$. The fermonic field that creates a π-electron at a position $\mathbf{r}$ referring to the sublattice A in the continuum can be expressed in terms of these Bloch wavefunctions as

$$\begin{aligned} c_A^\dagger(\mathbf{r}) =& \int_{BZ} d\mathbf{k}\ \psi_{A,\mathbf{k}}^*(\mathbf{r})c_A^\dagger(\mathbf{k}) \\ =& \int_{BZ} d\mathbf{k}\ \psi_{A,\mathbf{k}}^*(\mathbf{r})\sum_i e^{i\mathbf{k}.\mathbf{R}_{Ai}}c_{A,i}^\dagger \\ c_A^\dagger(\mathbf{r}) =& \sum_i w_A^*(\mathbf{r}-\mathbf{R}_{Ai})c_{A,i}^\dagger\ , \end{aligned} \tag{2.11}$$

where w denotes the Wannier functions, and $\mathbf{R}_{Ai}$ a lattice vector corresponding to an atom A in unit cell i. Besides, the Bloch wavefunctions in a tight-binding approach are given by

$$\psi_{A,\mathbf{k}}(\mathbf{r}) = \sum_j \phi(\mathbf{r}-\mathbf{R}_{Aj})e^{i\mathbf{k}.\mathbf{R}_{Aj}}\ , \tag{2.12}$$

where ϕ is an atomic orbital centered at $\mathbf{R}_{Aj}$. Note that it does not depend on the sublattice index since graphene is made of carbon atoms only. Relations (2.11) and (2.12) together lead to $w_A(\mathbf{r}-\mathbf{R}_{Ai}) = \phi(\mathbf{r}-\mathbf{R}_{Aj})$ and finally

$$c_A^\dagger(\mathbf{r}) = \sum_i \phi^*(\mathbf{r}-\mathbf{R}_{Aj})c_{A,i}^\dagger\ . \tag{2.13}$$

Of course, the same relation holds on sublattice B when doing the substitution $A \mapsto B$. Therefore, the Green's function reads

$$\begin{aligned} G_{\alpha\beta}(\mathbf{r_1},\mathbf{r_2},i\omega_n) =& -\langle c_\beta(\mathbf{r_1},i\omega_n)c_\alpha^\dagger(\mathbf{r_2},i\omega_n)\rangle \\ =& \sum_{ij}\phi(\mathbf{r_1}-\mathbf{R}_{\beta i})\phi^*(\mathbf{r_2}-\mathbf{R}_{\alpha j})G_{\alpha\beta}(\mathbf{R}_{\beta i},\mathbf{R}_{\alpha\mathbf{j}},i\omega_n)\ , \end{aligned} \tag{2.14}$$

where α and β are the sublattice indices. Also the thermic average $\langle ... \rangle$ depends on the picture chosen for the operators (Heisenberg picture, interaction picture for perturbative approaches...), so that the above expression holds for both Green's functions G_0 and G. Under these conditions, the T-matrix reads

$$T(\omega) = \frac{V_0}{1 - V_0 \int_{BZ} G_{0,AA}(\mathbf{k},\omega)} \begin{pmatrix} 1 & 0 \\ 0 & 0 \end{pmatrix} , \tag{2.15}$$

and the LDOS correction in real space is given by

$$\begin{aligned}
\Delta\rho(\mathbf{r},\omega) &= -\frac{1}{\pi} Im\Big[Tr\,\Delta G(\mathbf{r},\mathbf{r},\omega)\Big] \\
&= -\frac{1}{\pi} Im\Big[\Delta G_{AA}(\mathbf{r},\mathbf{r},\omega) + \Delta G_{BB}(\mathbf{r},\mathbf{r},\omega)\Big] \\
&= -\frac{1}{\pi}\sum_{ij} Im\Big[\phi(\mathbf{r}-\mathbf{R}_{Ai})\phi^*(\mathbf{r}-\mathbf{R}_{Aj})\Delta G_{AA}(\mathbf{R}_{Ai},\mathbf{R}_{Aj},\omega) \\
&\qquad + \phi(\mathbf{r}-\mathbf{R}_{Bi})\phi^*(\mathbf{r}-\mathbf{R}_{Bj})\Delta G_{BB}(\mathbf{R}_{Bi},\mathbf{R}_{Bj},\omega)\Big] \\
&= -\frac{1}{\pi}\sum_{ij} Im\Big[\phi(\mathbf{r}-\mathbf{R}_{Ai})\phi^*(\mathbf{r}-\mathbf{R}_{Aj})G_{0,AA}(\mathbf{R}_{Ai},0,\omega)T_{AA}(\omega)G_{0,AA}(0,\mathbf{R}_{Aj},\omega) \\
&\qquad + \phi(\mathbf{r}-\mathbf{R}_{Bi})\phi^*(\mathbf{r}-\mathbf{R}_{Bj})G_{0,BA}(\mathbf{R}_{Bi},0,\omega)T_{AA}(\omega)G_{0,AB}(0,\mathbf{R}_{Bj},\omega)\Big] \\
\Delta\rho(\mathbf{r},\omega) &= -\frac{1}{\pi}\sum_{ij} Im\Big[\phi(\mathbf{r}-\mathbf{R}_{Ai})\phi^*(\mathbf{r}-\mathbf{R}_{Aj})G_{0,AA}(\mathbf{R}_{Ai},\omega)T_{AA}(\omega)G_{0,AA}(-\mathbf{R}_{Aj},\omega) \\
&\qquad + \phi(\mathbf{r}-\mathbf{R}_{Bi})\phi^*(\mathbf{r}-\mathbf{R}_{Bj})G_{0,BA}(\mathbf{R}_{Bi},\omega)T_{AA}(\omega)G_{0,AB}(-\mathbf{R}_{Bj},\omega)\Big] ,
\end{aligned} \tag{2.16}$$

where $G_{0,\alpha\beta}(\mathbf{R}_{\gamma i},\omega) = \int_{BZ} d\mathbf{k}\ G_{0,\alpha\beta}(\mathbf{k},\omega)e^{-i\mathbf{k}.\mathbf{R}_{\gamma i}}$. The atomic orbitals ϕ are basically Gaussian or Lorentz functions for numerical computations. When the characteristic width of these functions goes to zero, i.e. $\phi \to \delta$ (the Dirac delta function), the Fourier transform of the LDOS correction on sublattice B reads

$$\begin{aligned}
\Delta\rho_B(\mathbf{q},\omega) &= -\frac{1}{\pi}\int d\mathbf{r}\ e^{i\mathbf{q}.\mathbf{r}} Im\Big[\Delta G_{BB}(\mathbf{r},\mathbf{r},\omega)\Big] \\
&= -\frac{1}{2i\pi}\int d\mathbf{r}\ e^{i\mathbf{q}.\mathbf{r}}\Big[\Delta G_{BB}(\mathbf{r},\mathbf{r},\omega) - \Delta G^*_{BB}(\mathbf{r},\mathbf{r},\omega)\Big] \\
&= \frac{i}{2\pi}\int d\mathbf{r}\ e^{i\mathbf{q}.\mathbf{r}}\sum_{i,j}\delta(\mathbf{r}-\mathbf{R}_{Bi})\delta(\mathbf{r}-\mathbf{R}_{Bj})\Big[G_{0,BA}(\mathbf{R}_{Bi},\omega)T_{AA}(\omega)G_{0,AB}(-\mathbf{R}_{Bj},\omega) \\
&\qquad - G^*_{0,BA}(\mathbf{R}_{Bi},\omega)T^*_{AA}(\omega)G^*_{0,AB}(-\mathbf{R}_{Bj},\omega)\Big]
\end{aligned}$$

$$\begin{aligned}\Delta\rho_B(\mathbf{q},\omega) =& \frac{i}{2\pi}\sum_i e^{i\mathbf{q}\cdot\mathbf{R}_{Bi}}\Big[G_{0,BA}(\mathbf{R}_{Bi},\omega)T_{AA}(\omega)G_{0,AB}(-\mathbf{R}_B,\omega) \\ &\qquad - G^*_{0,BA}(\mathbf{R}_{Bi},\omega)T^*_{AA}(\omega)G^*_{0,AB}(-\mathbf{R}_{Bi},\omega)\Big] \\ =& \frac{i}{2\pi}\int_{BZ} d\mathbf{k}\Big[G_{0,BA}(\mathbf{k}+\mathbf{q},\omega)T_{AA}(\omega)G_{0,AB}(\mathbf{k},\omega) - G^*_{0,BA}(\mathbf{k}+\mathbf{q},\omega)T^*_{AA}(\omega)G^*_{0,AB}(\mathbf{k},\omega)\Big]\end{aligned} \tag{2.17}$$

Note that the momentum $\mathbf{q}$ is not restricted to the BZ. Finally, the LDOS correction due to sublatice A is obtained in the same way when doing the substitution $B \to A$

$$\Delta\rho_A(\mathbf{q},\omega) = \frac{i}{2\pi}\int_{BZ} d\mathbf{k}\Big[G_{0,AA}(\mathbf{k}+\mathbf{q},\omega)T_{AA}(\omega)G_{0,AA}(\mathbf{k},\omega) - G^*_{0,AA}(\mathbf{k}+\mathbf{q},\omega)T^*_{AA}(\omega)G^*_{0,AA}(\mathbf{k},\omega)\Big] \tag{2.18}$$

2.3 Nonrelativistic electron gas

2.3.1 Free electrons Green's function

Before studying the LDOS modulations induced by short-range potentials in graphene, we first study the usual case of a two-dimensional nonrelativistic electron gas. Although the results discussed in this chapter can essentially be found in the literature, the computational work they involve is not mentioned generally. For this reason we pay a careful attention to their establishment. In the case of a conventional electron gas, a parabolic spectrum describes the free particles, $\varepsilon(\mathbf{q}) \sim q^2$, where q labels the modulus of a two-dimensional momentum $\mathbf{q}$. In real space, the corresponding unperturbed Green's function is given by

$$G_0(\mathbf{r},\Omega) = \int_{\mathbb{R}^2} \frac{d\mathbf{q}}{(2\pi)^2}\frac{e^{i\mathbf{q}\cdot\mathbf{r}}}{\Omega - q^2} \, . \tag{2.19}$$

We define $\Omega = \omega^2$, for more convenience. It does not prevent Ω (resp. ω) from being negative (resp. imaginary). Using the following integral representation of the first kind Bessel's function J_0

$$J_0(qr) = \frac{1}{2\pi}\int_0^{2\pi} d\theta e^{iqr\cos\theta} = \frac{2}{\pi}\int_1^{+\infty} du \frac{\sin(qru)}{\sqrt{u^2-1}} \, , \tag{2.20}$$

the unperturbed propagator can be rewritten as

$$G_0(\mathbf{r},\omega) = \frac{1}{\pi^2}\int_1^{+\infty} \frac{du}{\sqrt{u^2-1}}\int_0^{+\infty} dq \frac{q\sin(qru)}{\omega^2 - q^2} \, . \tag{2.21}$$

The second integral, which runs for an even function of q, is performed after being decomposed in partial fractions

$$\frac{1}{2}\int_{-\infty}^{+\infty} dq\frac{q\sin(qru)}{\omega^2-q^2} =\frac{1}{i8\omega}\int_{-\infty}^{+\infty}\Big[\frac{qe^{iqru}}{\omega+q}+\frac{qe^{iqru}}{\omega-q}-\frac{qe^{-iqru}}{\omega+q}-\frac{qe^{-iqru}}{\omega-q}\Big]dq\,. \tag{2.22}$$

The sine function has been expressed in terms of exponentials in order to apply Jordan's Lemma. Indeed, when computing the two first integrals on the right-hand side of equation (2.22), we can use the complex-plane paths depicted in Fig. 2.2, where the origin-centered contour C^{+} (remember that $ur > 0$) gives a zero contribution. The Γ contour around the singularity leads to the following principal value

$$\langle p.v.\big[\frac{1}{\omega\pm q}\big]\,|qe^{iqru}\rangle = -i\pi\omega e^{\mp i\omega ru}\,, \tag{2.23}$$

where we use the bra-ket Dirac's notation for distributions. Via the Kramers-Kronig relation,

$$\begin{aligned}\int_{-\infty}^{+\infty}\frac{qe^{iqru}}{\omega+q} =&\langle p.v.\big[\frac{1}{\omega\pm q}\big]\,|qe^{iqru}\rangle - i\pi\langle\delta_{\mp\omega}|qe^{iqru}\rangle\\ =&-i\pi\omega e^{\mp i\omega ru}\pm i\pi\omega e^{\mp i\omega ru}\,.\end{aligned} \tag{2.24}$$

Proceeding in the same way for the two last integrals in (2.22), with the origin-centered contour C^{-}, yields the following result

$$\frac{1}{2}\int_{-\infty}^{+\infty} dq\frac{q\sin(qru)}{\omega^2-q^2} = -\frac{\pi}{2}e^{i\omega ru}\,, \tag{2.25}$$

so that the unperturbed Green's function in real space reads

$$G_0(\mathbf{r},\Omega) = -\frac{1}{2\pi}\int_{1}^{+\infty} du\frac{e^{i\omega ru}}{\sqrt{u^2-1}} = \frac{1}{4i}H_0^{(1)}(\sqrt{\Omega}\,r)\,, \tag{2.26}$$

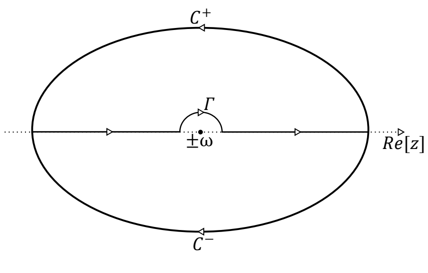

Fig. 2.2 Contour integral

where $H^{(1)}$ refers to the Hankel's function, i.e. a Bessel's function of the third kind. Remember that Bessel's functions naturally appear in cylindrical (spherical) coordinate systems dealing with propagating waves, like the ones described by the radial Schrödinger equation. Note also that one could have added equivalently an infinitely small imaginary part to the poles $\pm\omega$ in (2.22) to make them leave the real axis and then get the same result without using the distribution formalism.

2.3.2 Friedel oscillations

As we are interested in the LDOS large-distance oscillations, we look for a series expansion of the unperturbed Green's function for large values of r. Besides, we consider Hankel's functions for any index ν, not necessarily $\nu = 0$. This will become useful in the next sections. Such functions can be defined by the following integral representation

$$H_\nu^{(1)}(\omega r) = \frac{\Gamma(\frac{1}{2}-\nu)}{i\pi\Gamma(\frac{1}{2})}\left(\frac{\omega r}{2}\right)^\nu \int_{C_H} dz e^{i\omega r z}(z^2-1)^{\nu-1/2} \,, \tag{2.27}$$

where C_H is the Hankel contour depicted in Fig. 2.3. This contour was first introduced by the German mathematician Hermann Hankel in his investigations of the Gamma function [53]. When changing the integration contour by $z = 1 + i\tilde{z}$, which means translating C_H by -1 and then rotating it through an angle $-\pi/2$ about the origin, the two branch points move to 0 and $2i$ respectively. The integral running over the new contour yields

$$H_\nu^{(1)}(\omega r) = \frac{\sqrt{2}}{i\pi}\frac{\Gamma(\frac{1}{2}-\nu)}{\Gamma(\frac{1}{2})}(\omega r)^\nu e^{i(\omega r+\nu\frac{\pi}{2}+\frac{\pi}{4})} \int_0^{+\infty} dt \frac{e^{-\omega r t}}{t^{-\nu+\frac{1}{2}}(1+\frac{it}{2})^{-\nu+\frac{1}{2}}} \,. \tag{2.28}$$

At present, this integral converges for values of ν such that $Re(\nu) > -1/2$. We also recognise the Laplace transform of function $t^{\nu-\frac{1}{2}}(1+\frac{it}{2})^{\nu-\frac{1}{2}}$. Based on Watson's lemma, a series

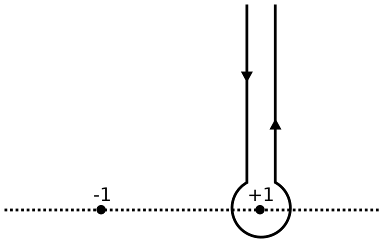

Fig. 2.3 Hankel contour representation in the complex plane.

expansion of this term for $\omega r \gg 1$ leads to

$$\begin{aligned}
H_\nu^{(1)}(\omega r) =& \frac{\sqrt{2}}{i\pi}\frac{\Gamma(\frac{1}{2}-\nu)}{\Gamma(\frac{1}{2})}(\omega r)^\nu e^{i(\omega r+\nu\frac{\pi}{2}+\frac{\pi}{4})}\int_0^{+\infty} dt e^{-\omega r t} t^{\nu-\frac{1}{2}} \sum_{n=0}^{+\infty}\left(\begin{array}{c}\nu-\frac{1}{2}\\ n\end{array}\right)\left(\frac{it}{2}\right)^n \\
=& \frac{\sqrt{2}}{i\pi}\frac{\Gamma(\frac{1}{2}-\nu)}{\Gamma(\frac{1}{2})}(\omega r)^\nu e^{i(\omega r+\nu\frac{\pi}{2}+\frac{\pi}{4})}\sum_{n=0}^{+\infty}\frac{\Gamma(\frac{1}{2}+\nu)}{\Gamma(n+1)\Gamma(\nu+\frac{1}{2}-n)}\left(\frac{i}{2}\right)^n\int_0^{+\infty} dt e^{-\omega r t} t^{\nu-\frac{1}{2}} \\
=& \frac{\sqrt{2}}{i\pi}\frac{\Gamma(\frac{1}{2}-\nu)}{\Gamma(\frac{1}{2})}(\omega r)^\nu e^{i(\omega r+\nu\frac{\pi}{2}+\frac{\pi}{4})}\sum_{n=0}^{+\infty}\frac{\Gamma(\frac{1}{2}+\nu)\Gamma(\nu+\frac{1}{2}+n)}{\Gamma(n+1)\Gamma(\nu+\frac{1}{2}-n)}\left(\frac{i}{2}\right)^n(\omega r)^{-\nu-\frac{1}{2}-n} \\
=& \frac{\sqrt{2}}{i\pi}\frac{\Gamma(\frac{1}{2}-\nu)\Gamma(\frac{1}{2}+\nu)}{\Gamma(\frac{1}{2})}\frac{e^{i(\omega r+\nu\frac{\pi}{2}+\frac{\pi}{4})}}{\sqrt{\omega r}}\sum_{n=0}^{+\infty}\frac{\Gamma(\nu+\frac{1}{2}+n)}{n!\Gamma(\nu+\frac{1}{2}-n)}\left(\frac{i}{2\omega r}\right)^n \\
H_\nu^{(1)}(\omega r) =& \sqrt{\frac{2}{\pi\omega r}}e^{i(\omega r-\nu\frac{\pi}{2}-\frac{\pi}{4})}\sum_{n=0}^{+\infty}\frac{\Gamma(\nu+\frac{1}{2}+n)}{n!\Gamma(\nu+\frac{1}{2}-n)}\left(\frac{i}{2\omega r}\right)^n . \qquad (2.29)
\end{aligned}$$

The method to get this expansion is quite tedious, but the result is going to be very useful all along the present chapter. Coming back to the non-relativistic electron gas, the free electron Green's function at large distances is well approximated by

$$G_0(\mathbf{r},\Omega) \sim \frac{e^{i(\sqrt{\Omega}r-\frac{3\pi}{4})}}{\sqrt{r}} . \qquad (2.30)$$

From its definition (2.19), it is clear that this propagator is an even function of $\mathbf{r}$ and satisfies $G_0(\mathbf{r},\Omega) = G_0(-\mathbf{r},\Omega)$. Actually this propagator is simply a function of $|\mathbf{r}|$ (rotational invariance). The correction to the bare Green's function is

$$\Delta G(\mathbf{r},\mathbf{r},\Omega) = G_0(\mathbf{r},\Omega)T(\Omega)G_0(-\mathbf{r},\Omega) \sim \frac{T(\Omega)}{r}e^{i(2\sqrt{\Omega}r+\frac{\pi}{2})} . \qquad (2.31)$$

Moreover, in the impurity problem we are considering, the T-matrix does not depend on the position. So it will not modify the long-wavelength oscillations decay generated in the LDOS. Thus, we only consider the limit of a small impurity potential for simplicity. To first approximation, the LDOS correction defined in (2.8) behaves as

$$\Delta\rho(\mathbf{r},\Omega) \sim V_0\frac{\cos(2\sqrt{\Omega}r)}{\sqrt{\Omega}r} . \qquad (2.32)$$

This is the result Adhikari has already discussed in a careful analysis of the impurity problem for nonrelativistic electrons in two dimensions [54]. Therefore, a localised defect induces Friedel oscillations with a wavevector $q = 2k_F$ in the LDOS. Indeed, the nonrelativistic electron energy is given by $\Omega_F \sim k_F^2$ at the Fermi level. On top of that, these Friedel oscillations decay algebraically, as the inverse of the distance to the impurity.

The quantum interferences, induced by step edges and point defects in the LDOS, have already been observed at the Cu(111) surface [55], and the Au(111) surface [56] using scanning tunneling microscopy (STM). This technique, developed by the 1986 Nobel laureates G. Binnig and H. Rohrer [52], is based on the concept of quantum tunneling. When varying the bias between a conducting tip and a metallic surface, it enables the electrons to tunnel through the vacuum. The measurement of the conductance leads to the electronic density as a function of the energy (LDOS). Although the specific features of the Friedel oscillations can be obtained via this technique, it is useful to perform their Fourier transform too. Let us see how they manifest themselves in momentum space by computing the Fourier transform of the interference term (2.32)

$$\begin{aligned}\Delta\rho(\mathbf{q},\omega) &= \int_{\mathbb{R}^2} d\mathbf{r}\frac{\cos(2\omega r)e^{-i\mathbf{q}.\mathbf{r}}}{\omega r} \\ &= \frac{\pi}{\omega}\lim_{\varepsilon\to 0}\int_0^{+\infty} dr\, J_0(qr)[e^{-(\varepsilon-i2\omega)r}+e^{-(\varepsilon+i2\omega)r}]\ ,\end{aligned} \tag{2.33}$$

where the integral has been regularised by $\varepsilon > 0$. In the above expression, we recognise the Laplace transform of the Bessel function J_0. It is defined by

$$L[J_0](p) = \int_0^{+\infty} dx\, J_0(x)e^{-px}\ . \tag{2.34}$$

Since J_0 satisfies the Bessel equation $xJ_0''(x)+J_0'(x)+xJ_0(x)=0$, its Laplace transform verifies the differential equation $(1+p^2)L'(p)+pL(p)=0$, whose solution is nothing but

$$L(p) = A/(1+p^2)^{1/2}\ . \tag{2.35}$$

The constant A is obtained by remarking that, on the one hand $\lim\limits_{p\to 0} L[J_0'] = 0$, and on the other hand $\lim\limits_{p\to 0} L[J_0'] = pL[J_0](p) - J_0(0) = A-1$. So $A=1$, and the Fourier transform in (2.33) is rewritten as

$$\begin{aligned}\Delta\rho(\mathbf{q},\omega) &= \frac{\pi}{\omega q}\Big[\frac{1}{\sqrt{1-\left(\frac{2\omega}{q}\right)^2}}+\frac{1}{\sqrt{1-\left(\frac{2\omega}{q}\right)^2}}\Big] \\ &= \frac{2\pi}{\omega}\frac{\theta(q-2\omega)}{\sqrt{q^2-4\omega^2}}\end{aligned} \tag{2.36}$$

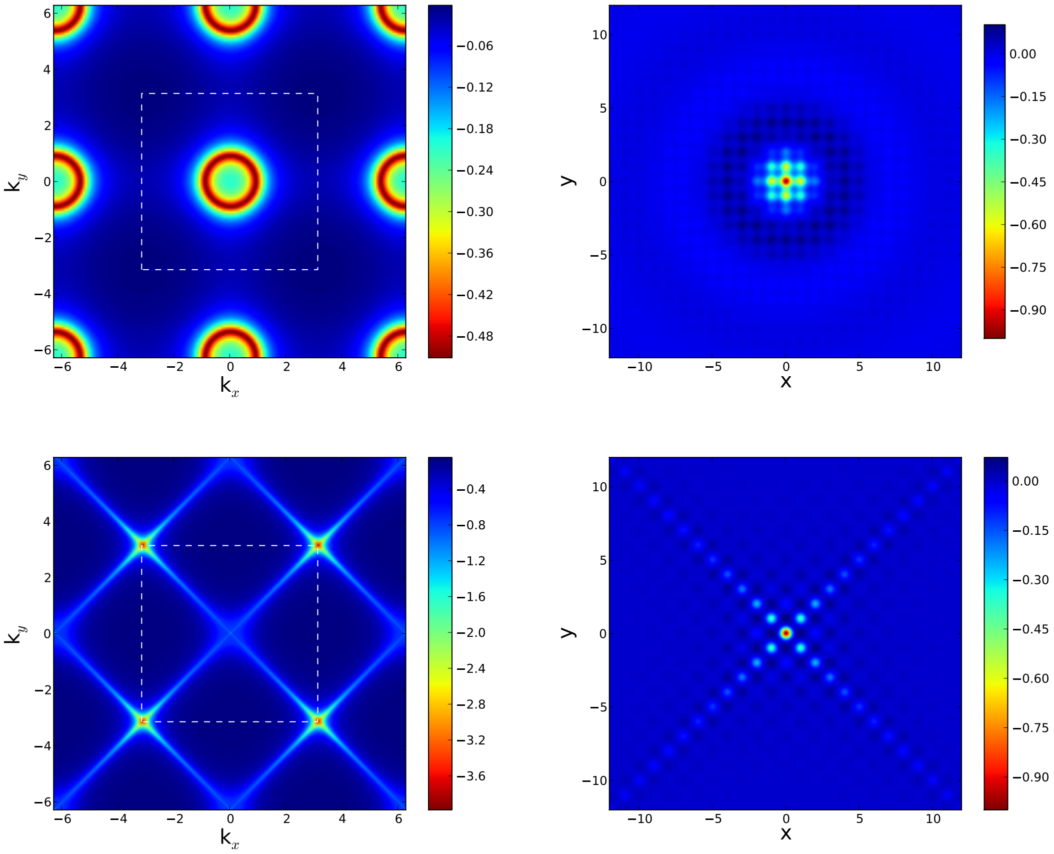

Fig. 2.4 LDOS correction for the square lattice (right) and its Fourier transform (left) in the parabolic-band approximation (top, $\Omega = 0.20t$) and at the Van Hove singularity energy (bottom, $\Omega = 4.00t$). The white dashed lines depict the Brillouin zone.

It finally reads

$$\Delta\rho(\mathbf{q},\Omega) = \frac{2\pi}{\sqrt{\Omega}} \frac{\theta(q - 2\sqrt{\Omega})}{\sqrt{q^2 - 4\Omega}} \ . \tag{2.37}$$

The Heaviside step function means that their is no intensity for wavevectors whose modulus is smaller than $2k_F$. The intensity diverges for wavevectors satisfying $q = 2k_F$, before vanishing for larger momenta. Thus, the $1/r$ decaying long-range modulations the impurity induces should manifest themselves through an empty $2k_F$-radius circle in the reciprocal space.

In order to illustrate this point, we numerically compute the LDOS and its Fourier transform in the case of a square lattice with a localised impurity. They are depicted in Fig. 2.4. The first row corresponds to the parabolic-band approximation we have discussed so far,

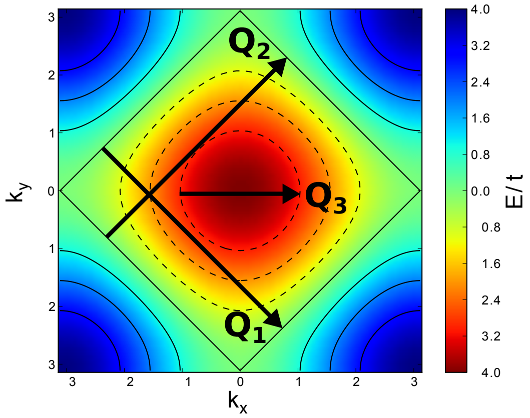

Fig. 2.5 Constant-energy contours of the square-lattice spectrum in the first Brillouin zone and nesting vectors. The rotated square line outlines the constant zero-energy contour that corresponds to the Van Hove singularity in the density of states.

while the second row refers to the Van Hove singularity that occurs at half-filling for the tight-binding model on the square lattice. The impurity is located at the real space origin.

At low energy, i.e. $\Omega = 0.2t$ where t is the nearest-neighbour amplitude, the Fourier transform of the LDOS correction shows a high-intensity circle in red, within the first Brillouin zone. Other circles are just replicas relative to reciprocal lattice vectors. This feature is in agreement with the analytical prediction (2.37). More generally, any elastic scattering between two states $\mathbf{k}$ and $\mathbf{k}'$ yields spatial modulations with wavevector $\mathbf{q} = \mathbf{k}' - \mathbf{k}$. The scattering probability depends on the curvature of the constant-energy contour defined by the Fermi surface. It is particularly efficient for good nesting vectors, namely wavevectors satisfying $q = 2k_F$ in our case [56, 57]. In the parabolic-band approximation, the Fermi surface is circular. The nesting vectors are then defined by $\mathbf{k}' = -\mathbf{k}$, which corresponds to a backscattering process. Such a wavevector, namely $\mathbf{Q_3}$, is depicted in Fig. 2.5 for a circular constant-energy contour. By isotropy, one easily realises that the orientation of vector $\mathbf{Q_3}$ does not matter, which explains the high-intensity circles in the LDOS Fourier transform in Fig. 2.4.

At the Van Hove singularity however, the topology of the Fermi surface changes and the constant-energy contour is a square. There are four efficient scattering wavevectors that connect two opposite edges of this square. It concerns the nesting vectors $\pm\mathbf{Q_1}$ and $\pm\mathbf{Q_2}$ in Fig. 2.5. This is what the four high-intensity areas, which are located at the corners of the Brillouin zone, describe in Fig. 2.4. So the scattering in real space is predominant with respect to these four nesting vectors.

Not only the STM spectroscopy measurement is a local probe of the electronic density even in the presence of defects, but it also reveals the constant-energy contours in momentum space via the nesting vectors. The electronic filling does not matter for such a technique, since it is able to probe both the empty states (above the Fermi sea) when injecting electrons and the occupied states (below the Fermi sea) when injecting holes. In the two following sections, we will see that STM experiments can also probe the chirality of electrons, namely the projection of the pseudospin on the momentum direction.

2.4 Chiral massless Dirac electrons

2.4.1 Scanning tunneling microscopy analysis

The constant-energy contours that describe massless Dirac electrons in graphene are also circular. They are depicted by the black dashed lines in Fig. 2.6 and refer to the Dirac cones located at the corners of the hexagonal Brillouin zone. Thus, there are two nonequivalent circular Fermi surfaces, one per valley. Consequently, the scattering may take place within a given valley, and one speaks of $intravalley$ scattering, but it may also occur between two distinct valleys. Indeed, the presence of a short-range impurity yields a large potential in momentum space, so that it can couple two momenta that are far apart. In such a case, one speaks of $intervalley$ scattering.

Whatever it is, backscattering should be the more efficient process again, due to the circular shape of the constant-energy contours. Therefore, the Friedel oscillations generated by a point defect should exhibit a $1/r$ algebraic decay, as they do in the case of a nonrelativistic electron gas. However, this is not what is observed in STM experiments [58, 59]. We numerically compute the LDOS as well as its Fourier transform, whose two-dimensional patterns are presented in Fig 2.7. This is an illustration of what is experimentally obtained. In the conical approximation ($\omega = 0.15t$), the LDOS have a three-fold symmetry with respect to the defect which is located at the origin, on the sublattice A. It appears that the electrons are mainly localised on the sublattice B, which corresponds to the red areas in the figure. First, we rather focus on the Fourier transform of the LDOS correction.

On the one hand, let us identify the modulations induced by intervalley scattering. From Fig. 2.6, there are six distinct vectors that couple two nearest-neighbour valleys, among which vectors $\pm\mathbf{Q_4}$. Together, the six vectors should lead to six $2k_F$-radius circles located at the corners of the hexagonal Brillouin zone, delimited by the white dashed lines in the figure. This is what happens in Fig 2.7, except that the rotational symmetry is broken resulting in

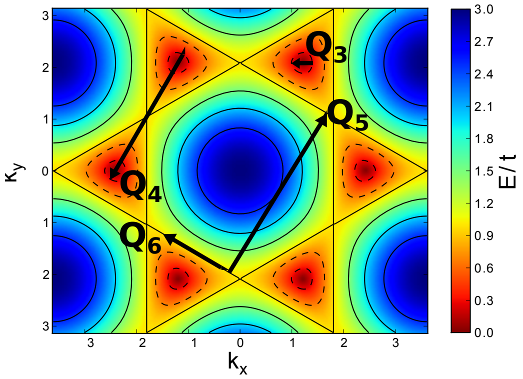

Fig. 2.6 Constant-energy contours of the graphene spectrum and good nesting vectors. The nesting vector $\mathbf{Q_4}$ connects constant low-energy contours of two non-equivalent valleys, whereas the nesting vector $\mathbf{Q_3}$ refers to a the constant low-energy contour within a single valley. The nesting vectors $\mathbf{Q_5}$ and $\mathbf{Q_6}$ describes scattering processes at the Van Hove singularity energy ($\omega = t$).

circular arcs only. The reason why it is broken is given later on. But at least, the $2k_F$-radius circular arcs are the manifestation of the intervalley backscattering efficiency.

On the other hand, *intravalley* scattering occurs within any single valley. Its manifestation is then expected for small momenta. Based on Fig 2.7 there is an intensity modulation around the zero momentum. It corresponds to the red central disk around the zero momentum. This is in opposition to the intervalley scattering and the nonrelativistic electrons cases. Note that the replicas of intravalley scattering, which are associated to reciprocal lattice vectors and lie at the edges of the plot, lead to empty circles. The explanation based on an analytical computation of the Friedel oscillations will be given later.

This discrepancy between intravalley and intervalley scattering means that the shape of the Fermi surfaces is not sufficient to give a qualitative picture of the impurity scattering in graphene. The issue actually relies on the *pseudospin*, this extra degree of freedom that refers to the two sublattices A and B in the real space. As mentioned in Chapter 1, chiral Dirac electrons propagating in opposite directions, as it should be for backscattering, must have opposite pseudospin within a given valley, for their chirality is a conserved quantity. Then the overlap between the incoming and outgoing wavefunctions should be zero. This is what happens in the presence of long-range disorder, which does not couple the two distinct valleys and entirely suppresses the backscattering process [6].

Before studying the Friedel oscillations in more details, we qualitatively discuss what happens when focusing right at the Van Hove singularity energy. The Fermi surface is now hexagonal. As illustrated in Fig. 2.6, there are six good nesting vectors that couple two opposite edges of the hexagonal contour, among which $\pm\mathbf{Q_5}$. They are the wavevectors that lead to the red areas in reciprocal space in Fig 2.7. In real space, the quantum interferences are well marked with respect to these six wavevectors. There are also nesting vectors that couple two states along the same edge of the hexagonal contour, like $\pm\mathbf{Q_6}$ in Fig. 2.6. The modulus of these vectors is allowed to vary along the constant energy contour. This is the reason why there is a star-shape modulation around the zero momentum sin the LDOS Fourier transform (see Fig. 2.7).

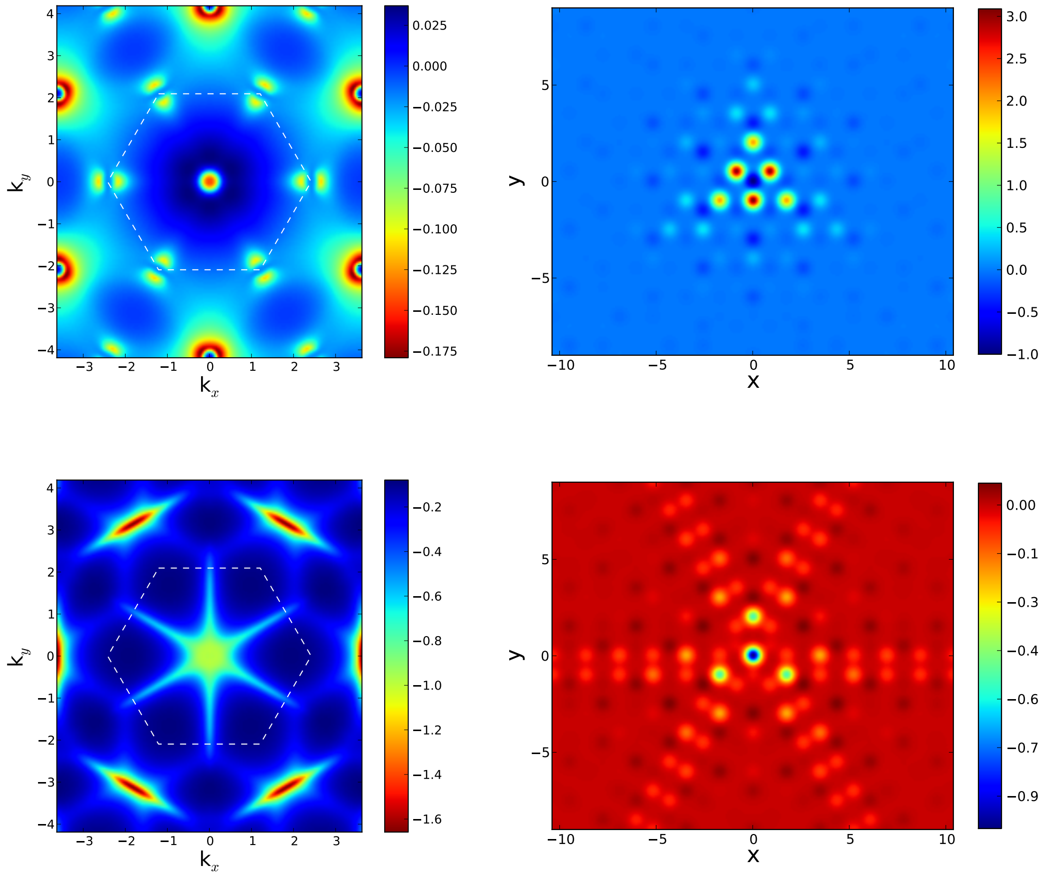

Fig. 2.7 LDOS correction (right) and its Fourier transform (left) for Dirac fermions in the honeycomb lattice (top, $\omega = 0.15t$) and at the Van Hove singularities (bottom, $\omega = 1.00t$). The white dashed lines depict the Brillouin zone.

2.4.2 Friedel oscillations

To determine accurately the role played by the graphene pseudospin, we describe the impurity problem in terms of the T-matrix. The low-energy Hamiltonian matrix

$$H(\mathbf{K_m}+\mathbf{q}) \simeq v_F \begin{pmatrix} 0 & qf_m(\mathbf{q}) \\ qf_m^*(\mathbf{q}) & 0 \end{pmatrix} \tag{2.38}$$

describes graphene Dirac electrons in the valley $\mathbf{K_m}$, where m labels any of the six valleys in the first Brillouin zone. Here $f_m(\mathbf{q}) = \mathbf{q}.\mathbf{J_m}/q$ is a simple phase factor, since $\mathbf{J_m}$ are complex unit vectors [60]. Such fermions correspond to the following eigenstates in momentum space

$$\psi_{m,\pm}(\mathbf{q}) = \begin{pmatrix} 1 \\ \pm f_m(\mathbf{q}) \end{pmatrix} , \tag{2.39}$$

The function f_m is the phase factor responsible for the absence of backscattering in graphene. Remember that $f_m(-\mathbf{q}) = -f_m(\mathbf{q})$ requires $\psi^\dagger_{m,\pm}(-\mathbf{q})\psi_{m,\pm}(\mathbf{q}) = 0$, which means that the overlap between two counter propagating waves referring to the same valley m is rigorously null. The unperturbed Green's function introduced in (2.10) is a 2×2 matrix and can be written as

$$G_0(\mathbf{r},\omega) = \int \frac{d\mathbf{q}}{(2\pi)^2} \frac{e^{i\mathbf{q}.\mathbf{r}}}{\omega^2 - q^2} \begin{pmatrix} \omega & qf_m(\mathbf{q}) \\ qf_m^*(\mathbf{q}) & \omega \end{pmatrix} . \tag{2.40}$$

In the above expression, ω refers to the energy, whereas it was $\Omega = \omega^2$ that denoted the energy in the non-relativistic electrons problem. Two kinds of integrals have to be computed when looking for a large-distance expression of the bare Green's function. The first one corresponds to the diagonal components of matrix (2.40). It has already been seen in the definition (2.19), and results in

$$G_{0,AA}(\mathbf{r},\omega) = \frac{\omega}{4i} H_0^{(1)}(\omega r) . \tag{2.41}$$

The second integral, which have to be computed, corresponds to the off-diagonal component of matrix (2.40). It turns out that

$$G_{0,AB}(\mathbf{r},\omega) = \int \frac{d\mathbf{q}}{(2\pi)^2} (J_{m,x}q_x + J_{m,y}q_y) \frac{e^{i\mathbf{q}.\mathbf{r}}}{\omega^2 - q^2}$$

$$\begin{aligned}
G_{0,AB}(\mathbf{r},\omega) =& (-i)\left[J_{m,x}\partial_x + J_{m,y}\partial_y\right] \int \frac{d\mathbf{q}}{(2\pi)^2} \frac{e^{i\mathbf{q}.\mathbf{r}}}{\omega^2 - q^2} \\
=& -\frac{\omega}{4}\left[\frac{J_{m,x}x + J_{m,y}y}{\sqrt{x^2+y^2}}\right] \partial H_0^{(1)}(\omega\sqrt{x^2+y^2}) \\
G_{0,AB}(\mathbf{r},\omega) =& \frac{\omega}{4} f_m(\mathbf{r})\, H_1^{(1)}(\omega r)\,,
\end{aligned} \tag{2.42}$$

where f_m is the phase factor introduced in (2.39), except that we will use from now on its real space form. Thus, the 2×2 unperturbed Green's function becomes

$$G_0(\mathbf{r},\omega) = \frac{\omega}{4}\begin{pmatrix} -iH_0^{(1)}(\omega r) & f_m(\mathbf{r})H_1^{(1)}(\omega r) \\ f_m^*(\mathbf{r})H_1^{(1)}(\omega r) & -iH_0^{(1)}(\omega r) \end{pmatrix}. \tag{2.43}$$

Based on the expansion (2.29), a first order approximation leads to

$$\begin{aligned}
\Delta\rho_A(\mathbf{r},\omega) &\simeq \frac{i}{8\pi}\, T(\omega)\, e^{i2\omega r + i(\mathbf{K_m}-\mathbf{K_n}).\mathbf{r}}\, \frac{\omega}{r}\left[1 + \frac{\Gamma(\frac{3}{2})}{\Gamma(-\frac{1}{2})}\frac{i}{2\omega r} + ...\right] \\
\Delta\rho_B(\mathbf{r},\omega) &\simeq \frac{i}{8\pi}\, T(\omega)\, e^{i2\omega r + i(\mathbf{K_m}-\mathbf{K_n}).\mathbf{r}}\, \frac{\omega}{r} f_m^*(\mathbf{r}) f_n(-\mathbf{r})\left[1 + \frac{\Gamma(\frac{5}{2})}{\Gamma(\frac{1}{2})}\frac{i}{2\omega r} + ...\right],
\end{aligned} \tag{2.44}$$

where T is the only non-zero T-matrix component. The momenta $\mathbf{K_m}$ and $\mathbf{K_n}$ correspond to two valleys in momentum space.

In the case of intervalley scattering ($m \neq n$) a localised impurity induces long-range oscillations in the LDOS that decay as $1/r$ on both sublattices [60]. The total LDOS averaged on the unit cell exhibits the same algebraic decay

$$\Delta\rho(\mathbf{r},\omega) \sim \frac{\cos(2\omega r)}{r}\,. \tag{2.45}$$

The Friedel oscillations induced by intervalley scattering in graphene decay with the same algebraic law as in a nonrelativistic electron gas (2.32). In momentum space, we have pointed out in (2.37) that these oscillations generate high-intensity empty circles. We remind here their expression in momentum space

$$\Delta\rho(\mathbf{q},\omega) \sim \frac{\theta(q - 2\sqrt{\Omega})}{\sqrt{\Omega q^2 - 4\Omega^2}}\,. \tag{2.46}$$

Again, the $2k_F$ oscillations are predominant, which is an evidence of the backscattering efficiency. Coming back to the STM experiments whose Fourier transform is illustrated in Fig. 2.7, two kinds of intervalley scattering can be distinguished. First, the circular arcs at the corners of the Brillouin zone (white dashed lines) result from scattering processes between two nonequivalent valleys for which $f_m^*(\mathbf{r})f_n(-\mathbf{r})$ is a function of $\mathbf{r}$, which breaks the rotational symmetry as explained in [60]. Second, the empty circles at the plot edges result from a scattering occurring between two neighbouring equivalent valleys that are consequently coupled by reciprocal lattice vectors. This refers to an Umklapp process. In this case, $f_m^*(\mathbf{r})f_n(-\mathbf{r})$ is just a phase factor independent of the vector $\mathbf{r}$ and the rotational invariance is preserved [60].

In the case of intravalley scattering ($m = n$), the LDOS is still given by (2.44) at large distances. Thus, one could still expect backscattering to be the predominant process, with modulations wavevectors $q = 2k_F$. As previously mentioned, this is not what is observed in STM experiments. Because $m = n$ now, the following situation arises $f_m^*(\mathbf{r})f_m(-\mathbf{r}) = -1$. It means that the two sublattice contributions given in (2.44) are in antiphase, and they cancel each other when averaging on the unit cell. The long-range oscillations are obtained from the next leading order, which leads to

$$\Delta\rho(\mathbf{r},\omega) \sim \frac{\sin(2\omega r)}{r^2} \,. \tag{2.47}$$

Due to the pseudospin induced phase factor $f_m(\mathbf{r})$, the Friedel oscillations are strongly reduced to a $1/r^2$ decay, in the case of intravalley scattering [17, 61, 62]. This can be interpreted as a chirality effect of the graphene Dirac electrons, which requires the pseudospin to be either parallel or antiparallel to the momentum within a given valley. This is a fundamental discrepancy with intervalley-scattering-induced modulations that decay as $1/r$, similarly to the case of a conventional electron gas.

Concerning the Friedel oscillations in momentum space, they are given by

$$\begin{aligned}\Delta\rho(\mathbf{q},\omega) &= \int d\mathbf{r}\frac{\sin(2\omega r)}{r^2}e^{-i\mathbf{q}.\mathbf{r}} \\ &\sim \frac{\pi}{2}\theta(2\omega - q) + \arcsin\big(\frac{2\omega}{q}\big)\theta(q-2\omega)\,,\end{aligned} \tag{2.48}$$

where we have used the fact that the Fourier transform of the cardinal sine function is the rectangular function. This leads to a filled circle of high intensity in momentum space for wavevectors satisfying $q < 2k_F$ ($\omega \sim k$). It explains the red-filled circular area around $q = 0$ in the LDOS Fourier transform illustrated in Fig. 2.7. The chirality of massless Dirac electrons, by forbidding the intravalley backscattering, strongly reduces the $2k_F$ modulations. It means that STM can also be used to probe the chiral nature of massless Dirac fermions.

2.5 Semi-Dirac electrons at the Lifshitz transition

2.5.1 Friedel oscillations

In the above sections, we have shown that the impurity scattering is usually most efficient for wave vectors satisfying $q = 2k_F$, meaning backscattering is generally the predominant process. In graphene, the chirality within a given Dirac cone strongly affects this and the Friedel oscillations. In what follows, we would like to focus on the case of the Dirac merging transition. As explained in Chapter 1, it is possible to make the two-nonequivalent Dirac cones move away from the corners of the BZ by applying a uniform strain onto the graphene sheet [43]. For a critical value of the strain magnitude, which is not experimentally achievable in graphene [46], the two cones merge into a single one, defining a Lifshitz transition [16]. At low energy, the dispersion relation close to this valley is given by

$$\varepsilon_{\pm}(\mathbf{q}) = \pm\sqrt{(c_y q_y)^2 + \left(\frac{q_x^2}{2m^*}\right)^2}\,, \tag{2.49}$$

where c_y is a characteristic velocity and m^* plays the role of renormalised mass. Exactly at the transition, the dispersion relation is said to be semi-Dirac, for it is linear in q_y but quadratic with respect to q_x. The constant-energy contours have an elliptical shape at low energy, as depicted by the black dashed lines in Fig. 2.8. By analogy with the conical-dispersion case studied above, the linearity along q_y requires the pseudospin to be either parallel or antiparallel to the momentum. The phase of the spinor Bloch eigenstates $\psi_{\pm}(\mathbf{q}) = (1, \pm e^{i\theta_{\mathbf{q}}})$ satisfies $\theta_{-q_y} = \theta_{q_y} + \pi$. Note it only occurs for momenta satisfying $q_x = 0$, but one expects it to affect the Friedel oscillations. To check this, we start from the low-energy expansion of the Hamiltonian matrix [45]

$$H(\mathbf{q}) \simeq \begin{pmatrix} 0 & \frac{q_x^2}{2m^*} - ic_y q_y \\ \frac{q_x^2}{2m^*} + ic_y q_y & 0 \end{pmatrix}. \tag{2.50}$$

The unperturbed Green's function is given by

$$G_0(x,y,\omega) = \int \frac{d\mathbf{q}}{(2\pi)^2} \frac{e^{ixq_x} e^{iyq_y}}{\omega^2 - q_y^2 - q_x^4} \begin{pmatrix} \omega & q_x^2 - iq_y \\ q_x^2 + iq_y & \omega \end{pmatrix}, \tag{2.51}$$

where we have defined new variables, so that c_y and m^* are now hidden inside the coordinates of the vector $\mathbf{r}$. The diagonal integrals yields

$$G_{0,AA}(x,y,\omega) = -i\omega \int_0^\infty d\alpha e^{i\alpha\omega^2} \int \frac{dq_x}{2\pi} e^{ixq_x - i\alpha q_x^4} \int \frac{dq_y}{2\pi} e^{iyq_y - i\alpha q_y^2} , \tag{2.52}$$

where we have exponentiated the denominator by introducing an additional integral running over α. For $x = 0$ it yields

$$G^0_{AA}(0,y,\omega) \simeq 2^{-5/2}\Gamma(1/4)\omega^{3/4}y^{1/4}H^{(1)}_{-\frac{1}{4}}(\omega y) . \tag{2.53}$$

In a similar way we get

$$\begin{aligned} G^0_{AB}(0,y,\omega) &\simeq F2^{-3/4}\Gamma(3/4)\omega^{1/4}y^{-1/4}H^{(1)}_{1/4}(\omega y) \\ &\pm iF2^{-5/4}\Gamma(1/4)\omega^{3/4}y^{1/4}H^{(1)}_{3/4}(\omega y) \\ G^0_{BA}(0,y,\omega) &= \bar{F}2^{-3/4}\Gamma(3/4)\omega^{1/4}y^{-1/4}H^{(1)}_{1/4}(\omega y) \\ &\pm i\bar{F}2^{-5/4}\Gamma(1/4)\omega^{3/4}y^{1/4}H^{(1)}_{3/4}(\omega y) . \end{aligned} \tag{2.54}$$

Note that on the right-hand-side of the above formulae we have chosen to denote the absolute value $|y|$ simply by y. Moreover, the ± signs correspond to a positive and respectively negative value for y. And F is just a phase factor. Now we turn back to the Friedel Oscillations and evaluate the corrections to the LDOS using the above expressions for the Green's function components. The results are presented in Fig. 2.9. We compare these results to a full evaluation of the T-matrix (without making the low-energy expansion), as well as with

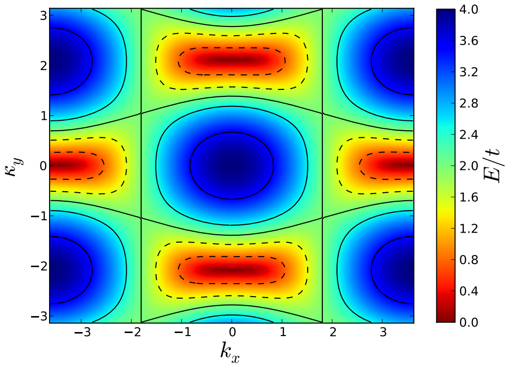

Fig. 2.8 Constant-energy contours at the Lifshitz transition.

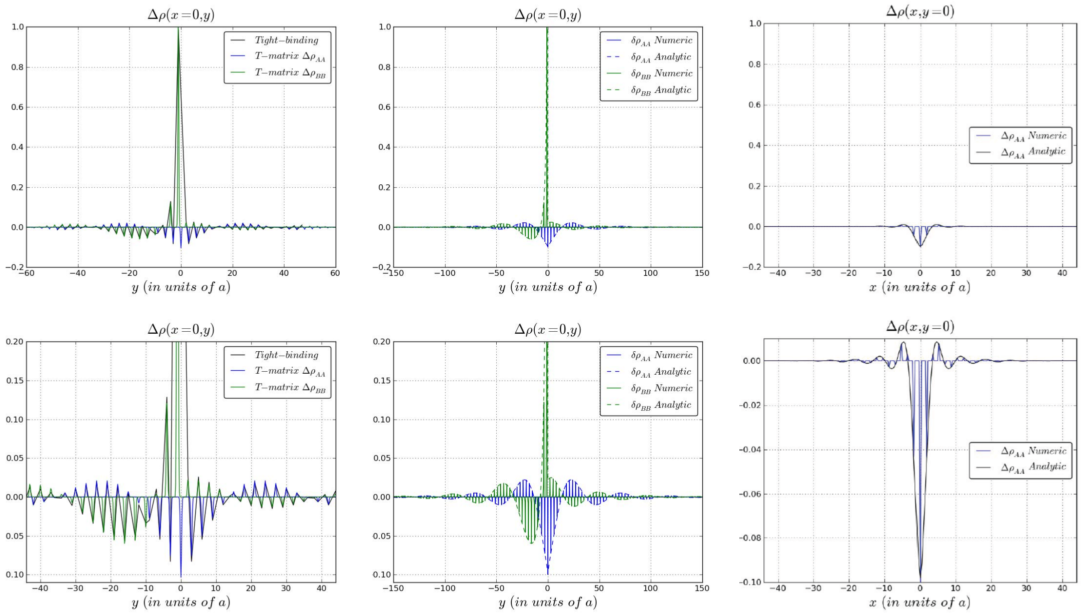

Fig. 2.9 LDOS correction as a function of position in the vicinity of the impurity right at the Lifshitz transitions. The second line presents a series of zooms-in of the plots outlined on the first line. In the first column we compare $\Delta\rho$ obtained using the full T-matrix approximation to the one obtained by the tight-binding method for an energy $\omega = -0.20t$. Note that, consistent to the low energy expansion given by Eq. (2.55), the Friedel oscillations are dephased by π between the two sublattices. The second column presents a comparison between the correction to the LDOS $\Delta\rho$ along the $x = 0$ direction obtained by the full T-matrix approximation (full lines) and by the low energy expansion (dotted lines) for $\omega = -0.20t$. In blue we plot the LDOS on the A sublattice comprising the impurity ($y = 0$) whereas in green the LDOS on the B sublattice. In the third column we plot the LDOS along the $y = 0$ direction obtained by the full T-matrix approximation for $\omega = -0.20t$. The blue curve is obtained using the full T-matrix approximation while the black one is obtained in the continuum approximation.

results obtained using the tight-binding method. As it can be seen in Fig. 2.9 all methods yield very similar results, which confirms their accuracy for this type of calculation. We also note that the LDOS correction is asymmetric between the positive and negative values of y on the B sublattice, whereas it is symmetric on the A sublattice. To obtain the asymptotic expansion of the Friedel oscillations we expand the Hankel functions for large values of ωy. Based on expansion (2.29), we get

$$\begin{aligned} \Delta\rho_A(0,y,\omega) &\sim \frac{\cos(2\omega y + \pi)}{\sqrt{y}} \\ \Delta\rho_B(0,y,\omega) &\sim \frac{\cos(2\omega y)}{\sqrt{y}} \end{aligned} \tag{2.55}$$

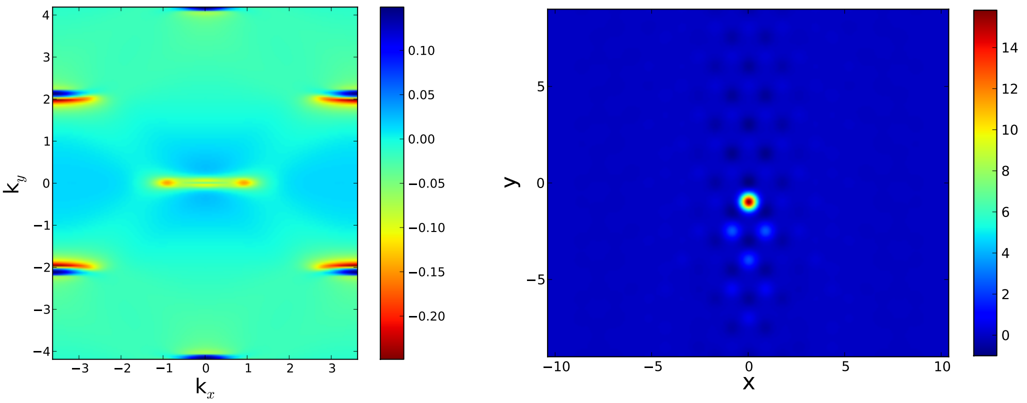

Fig. 2.10 LDOS (right) and its Fourier transform (left) for semi-Dirac electrons ($\omega = 0.15t$).

The resulting Friedel oscillations decay as $1/\sqrt{y}$ at large distances on both sublattices [19], slower than the typical inverse decay for a regular two-dimensional system, however their period is still proportional to $1/\omega$. When summing the contribution of the two sublattices, the terms in $y^{-1/2}$, which are dephased by a factor of π, vanish. The Friedel oscillations are then described by the next leading correction which is non-zero only on the B sublattice

$$\Delta\rho(0,y,\omega) \sim \mp\frac{1}{y}\cos\left(\frac{2\omega y}{c_y}+\frac{\pi}{4}\right). \tag{2.56}$$

Here the minus/plus signs correspond to positive and respectively negative values of y. The long wavelength oscillations thus decay following the usual $1/y$ law, different from the $1/r^2$ law corresponding to the intra-nodal scattering in typical graphene. Thus the transition from the $1/r^2$ decay to a $1/r$ decay in the low-energy FO provides a real-space signature of the Dirac points merging.

The Friedel oscillations along the perpendicular direction ($y = 0$) cannot be evaluated analytically, however in the third column of Fig. 2.9 we plot the dependence of the Friedel oscillations as a function of x for $y = 0$. Note that the amplitude of the oscillations is greatly reduced with respect of the oscillations in the y direction. Besides, the total LDOS correction $\Delta\rho$ and its momentum dependence are plotted in Fig. 2.10. In momentum space the outer regions, which were circular arcs in Fig. 2.7, have disappeared at the merging transition for which internodal quasiparticle scattering no longer exists. Moreover, we note that the features corresponding to intranodal scattering, centered on the sites of the reciprocal lattice are strongly anisotropic, corresponding to the low-energy anisotropic semi-Dirac spectrum. Regarding the LDOS correction, the modulations are much more pronounced at the position right under the impurity site. This is depicted by the red dots. Note also that the three fold symmetry is broken by the uniform strain.

Finally, we would like to point out an interesting situation that occurs when considering the limit of an infinite impurity potential. As explained in the next section, such an impurity generates a zero-energy state. It can be described when using the relation

$$H^{(1)}_{-1/4} = J_{-1/4} - i\frac{\cos(\pi/4)J_{-1/4} - J_{1/4}}{\sin(\pi/4)} \tag{2.57}$$

and considering the limit $\omega \to 0$ in (2.53) and (2.54), instead of the $\omega r \gg 1$ limit we have considered to calculate the form of the Friedel oscillations. The LDOS turns out to be zero on the sublattice A, whereas it behaves in the following manner on the sublattice B

$$\rho_B(0, y, \omega \to 0) \sim \frac{\theta(-y)}{y} \ . \tag{2.58}$$

While there is no electronic weight on the entire sublattice A, the Heaviside step function means that there is no electronic weight on the sublattice B for all the positive values of y. The explanation of this peculiar behaviour is given in the last chapter section through simple lattice considerations.

2.5.2 Beyond the merging transition

So far, the physics beyond the merging transition has not been explored. In such a gapped phase the spectrum is quadratic in both directions, although anisotropic

$$\varepsilon_\pm(\mathbf{q}) = \pm\left(\Delta + \frac{q_x^2}{2m^*} + \frac{c_y^2 q_y^2}{2\Delta}\right) \ , \tag{2.59}$$

where $2\Delta = t' - 2t$ is the energy gap beyond the merging. Defining $X = xm^*/\Delta$ and $Y = y/c_y$ so that $\mathbf{R} = (X, Y)$, and using expansion (2.29), the LDOS correction for electrons in the valence or conduction bands ($\omega^2 > \Delta^2$) can be written as

$$\begin{aligned} \Delta\rho_A(\mathbf{R}, \omega) &\sim \frac{\omega}{R}\cos\left(2\sqrt{\omega^2 - \Delta^2}R\right) \\ \Delta\rho_B(\mathbf{R}, \omega) &\sim \frac{\Delta^2}{R}\cos\left(2\sqrt{\omega^2 - \Delta^2}R\right) \ . \end{aligned} \tag{2.60}$$

Note that the Friedel oscillations decay as 1/R on both sublattices, typical of a usual bidimensional electron gas.

Besides, when $\omega^2 < \Delta^2$, expansion (2.29) holds with $\omega \to i\omega$, so that the LDOS decays exponentially

$$\begin{aligned}\Delta\rho_A(\mathbf{R},\omega) &\sim \frac{\omega}{R} e^{-2\sqrt{\Delta^2-\omega^2}R} \\ \Delta\rho_B(\mathbf{R},\omega) &\sim \frac{\Delta^2}{R} e^{-2\sqrt{\Delta^2-\omega^2}R} \,. \end{aligned} \tag{2.61}$$

To conclude, the long-wavelength modulations are reduced to a $1/r^2$ decay, as long as there exist chiral massless Dirac electrons, which typically refers to the semimetallic phase. Right at the Lifshitz transition, the two nonequivalent Dirac cones merge into a semi-Dirac spectrum. The massless electrons remain chiral along one direction. In this case, we recover the usual $1/r$ decay for the long-wavelength oscillations, although $1/\sqrt{r}$ decaying modulations do exist on both sublattices. Beyond the Lifshitz transition, the gapped spectrum, which define an insulating phase, is parabolic and we recover the conventional $1/r$ decaying modulations. Thus the Friedel oscillations induced by point defects reveal the nature (mass, chirality, ...) of the electrons in the system, and can be used as a real space signature for the Dirac-cone merging transition.

The table below qualitatively summarises the spatial decay of the Friedel oscillations as a function of the sublattice and the dispersion relation.

Dispersion relation	conical	semi-conical (along k_y)	parabolic
ρ_A	$1/r$	$1/\sqrt{y}$	$1/r$
ρ_B	$1/r$	$1/\sqrt{y}$	$1/r$
$\rho_A + \rho_B$	$1/r^2$	$1/y$	$1/r$

2.6 Vacancies as resonant scatterers

2.6.1 Low-energy resonances

From the T-matrix expression (2.15), the impurity induces resonances in the LDOS when

$$1 - V_0 G_{0,AA}(0,\omega) = 0 \,. \tag{2.62}$$

This condition leads to virtual bound states, namely localised states that hybridise with a continuum of delocalised states [63]. They have been described in the previous sections in a real space picture. The above condition is equivalent to

$$V_0 \simeq \frac{1}{\omega \ln\left(\frac{|\omega|}{D}\right)} \,, \tag{2.63}$$

when assuming that the resonance energy ω is small compared to the bandwidth D [64]. It means that we have to consider strong impurities in order to get a reasonably small resonance energy in graphene. To be more specific, the potential magnitude higher than 10eV is required to generate a resonance within 1eV of the Dirac point [61]. It fundamentally contrasts with a two-dimensional electron gas where any value of the potential gives rise to a low-energy resonance. In this case indeed, the resonance condition is given by

$$V_0 \simeq \frac{1}{\ln\left(\frac{|\omega|}{D}\right)} \,. \tag{2.64}$$

Both conditions (2.63) and (2.64) are illustrated in Fig. 2.11 where the bandwidth is the energy unit ($D = 1$). It is clear that a minimum potential magnitude is required in graphene (green curve) in order to get a resonance at low energy, whereas any impurity can be considered as a resonant scatterer in a usual electron gas (blue curve). Such strong impurity potentials come only from vacancies [62] and adatoms [65], so they seem to be the only ones realistic low-energy resonant scatterers in graphene.

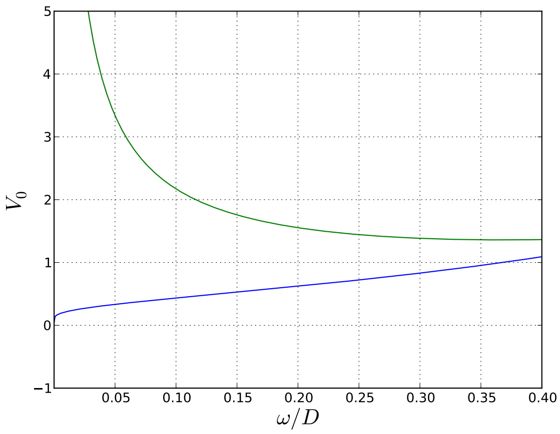

Fig. 2.11 Potential magnitude as a function of the resonance energy it induces in the case of a two-dimensional electron gas (blue lines) and in the case of graphene (green lines).

2.6.2 Lattice considerations

This last chapter section deals with vacancies, which can be induced by ion irradiation [66]. They are simulated by considering the potential magnitude as infinite, $V_0 \to \infty$. So the impurity site is not available for electrons and the resonant energy is rigorously zero. It turns out that the zero-energy resonant states induced by vacancies also reveal the phase the system belongs to in the vicinity of the Lifshitz transition.

As mentioned in Chapter 1, the graphene honeycomb lattice is made of two triangular sublattices A and B. The π-band electrons of graphene are well described in a nearest-neighbour tight-binding approximation. As long as we consider such a description, and more generally, as long as there is no intra-sublattice process considered, the lattice is said to be *bipartite*. The Hamiltonian of a bipartite system generically takes the form

$$H = \begin{pmatrix} 0 & T \\ T^\dagger & 0 \end{pmatrix} . \tag{2.65}$$

In the above matrix, T is a $N_A \times N_B$ block, not necessarily a square matrix. $N_{A(B)}$ is the number of atoms in the A(B) sublattice, assuming there is only one electron per atom. Here we restrict ourself to $N_B \geq N_A$. Such a Hamiltonian anti-commutes with

$$S = \begin{pmatrix} \mathbb{I}_{N_A} & 0 \\ 0 & -\mathbb{I}_{N_B} \end{pmatrix} , \tag{2.66}$$

where $\mathbb{I}_N$ is the $N \times N$ identity matrix so that the unitary operator S always squares to $+1$, which defines a chiral symmetry also called sublattice symmetry. This fundamental symmetry implies a particle-hole symmetric spectrum. Indeed, assuming $H|\psi\rangle = E|\psi\rangle$, then $HS|\psi\rangle = -ES|\psi\rangle$. Thus, the eigenstates always come by pairs with opposite energies when $E \neq 0$. But it also includes the possibility of existence of zero-energy states, which transform into themselves under the transformation S, i.e. $S|\psi\rangle = \pm|\psi\rangle$. As a consequence, they have null components on one sublattice. In other words, the two sublattices are independent at zero energy.

Moreover, every finite bipartite lattice has an extra number of $N_B - N_A$ zero-energy eigenstates living on the sublattice B, regardless of the components of the block T [67]. This property was first highlighted by B. Sutherland in the eighties [68]. While he was investigating the effect of the lattice quasiperiodicity on the wavefunction localisation, he found systems that reveal localised states at energies inside the bands and inside the band gap. He subsequently realised this has nothing to do with the lack of periodicity, but that it rather concerns the bipartite nature of the lattice. The proof relies on an elementary rank-nullity theorem. Consider the off-diagonal block T of the Hamiltonian (2.65) as the matrix representation of a linear transformation θ. This transformation maps the Hilbert space referring to sublattice B, η_B, onto the one referring to sublattice A, η_A. The rank-nullity theorem states that $dim\ \eta_B = dim\ Ker(\theta) + Rank(\theta)$. Since the rank is the dimension of the image of the linear map θ, it necessarily meets the following inequality $Rank(\theta) \leq N_A$, so that

$$dim\ Ker(\theta) \geq N_B - N_A\ . \tag{2.67}$$

It means that an additional number of $N_B - N_A$ zero-energy eigenstates of T, which are zero-energy eigenstates of H too, live exclusively on the sublattice B (in the case $N_B \geq N_A$). Note this is sometimes called the Lieb's theorem, making reference to his study of itinerant-electron magnetism in bipartite lattice [69].

In the presence of a single vacancy, $N_B - N_A = 1$, i.e. we have one zero-energy impurity-state wavefunction. Here the fundamental point is that the uniform strain, which enables to make the two Dirac cone merge, is encoded in the nearest-neighbour hopping amplitudes, which does not change the structure of the matrix (2.65). Then the sublattice symmetry ensures that such a zero-mode does exist both in the semi metallic phase and in the gapped phase. As a consequence, this zero-energy state is a good candidate to characterise the Dirac cones merging in real space. We study the form of this wavefunction, using simple arguments along the lines of [62]. In this work, the authors have determined the exact analytic form of the impurity wavefunction for an isotropic honeycomb lattice (graphene) with a single vacancy. Their method consists in an appropriate matching of the zero modes of two semi-infinite and complementary graphene sheets. This is the method we generalise in what follows for anisotropic graphene.

In Fig. 2.12 the two semi-infinite graphene sheets are defined such that their edges are orthogonal to the anisotropic direction, along which $t' = \alpha t$. Here we have introduced an anisotropy parameter α, that allows us to explore the Lifshitz transition. The presence of Dirac cones in the semimetallic phase corresponds to $\alpha < 2$, whereas the merging transition occurs for $\alpha = 2$. Then, the insulating phase corresponds to $\alpha > 2$. The upper half-plane has a 'bearded' edge, whereas the lower half-plane has a zigzag edge.

Let us first consider the lower half-plane terminated by the zigzag edge. The localised states at a 'zigzag graphite edge' were already determined by Fujita and collaborators in 1996 [7], a few years before the graphene research boom. Here we follow the prescrip-

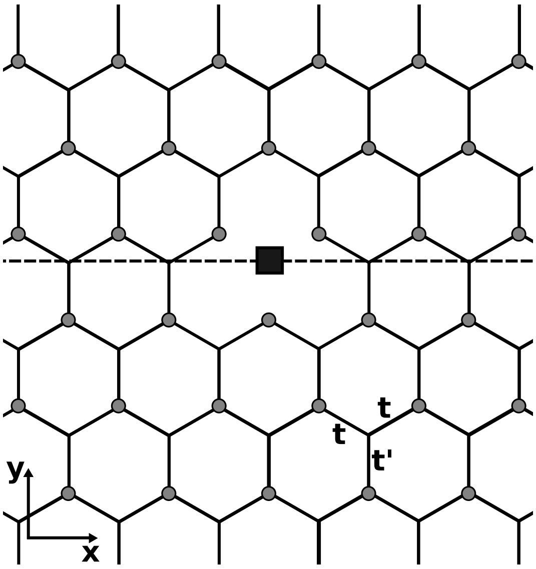

Fig. 2.12 Honeycomb lattice in presence of a vacancy (black square) on the sublattice A. The sites referring to the sublattice B are depicted by grey disks. The black dashed line divides the sheet into two semi-infinite planes. The lower half-plane has a zigzag edge, whereas the upper-half one has a 'bearded' termination. The nearest-neighbour hopping amplitude t' simulates an anisotropy and controls the Dirac cone merging transition.

tion addressed in this precursory work. There is a 'good' quantum number, which is the momentum k, associated to the translational invariance along the edge. Therefore, we set the wavefunction components on the edge as in Fig. 2.13. The wavefunction components referring to question marks are determined by taking into account the fact that we are looking for zero-energy states of the Hamiltonian. In the nearest-neighbour approximation, the wavefunction component $b^{(l)}$ satisfies the following recurrence relation

$$b^{(l)}_{m,n} + b^{(l)}_{m+1,n} + \alpha b^{(l)}_{m,n+1} = 0 \ , \tag{2.68}$$

where (l) refers to the lower half-plane. A general solution is

$$b^{(l)}_{m,n} = \left(-\frac{2}{\alpha}\cos\frac{k}{2}\right)^n e^{ik(m+\frac{n}{2})} \ . \tag{2.69}$$

The zero-energy evanescent modes vanish when $n \to \infty$, which means $|2\cos(k/2)| < \alpha$. It leads to values of the momentum such as $2Q_c < k < 2(\pi - Q_c)$, where $Q_c = \arccos(-\alpha/2)$. While for isotropic graphene ($\alpha = 1$) this condition is verified for $2\pi/3 \leq k \leq 4\pi/3$, above the merging point ($\alpha \geq 2$) such a condition is satisfied for all values of k ($0 \leq k \leq 2\pi$). The case $\alpha = 2$ leads to $k = 0$, associated to an extended state, and there are no allowed

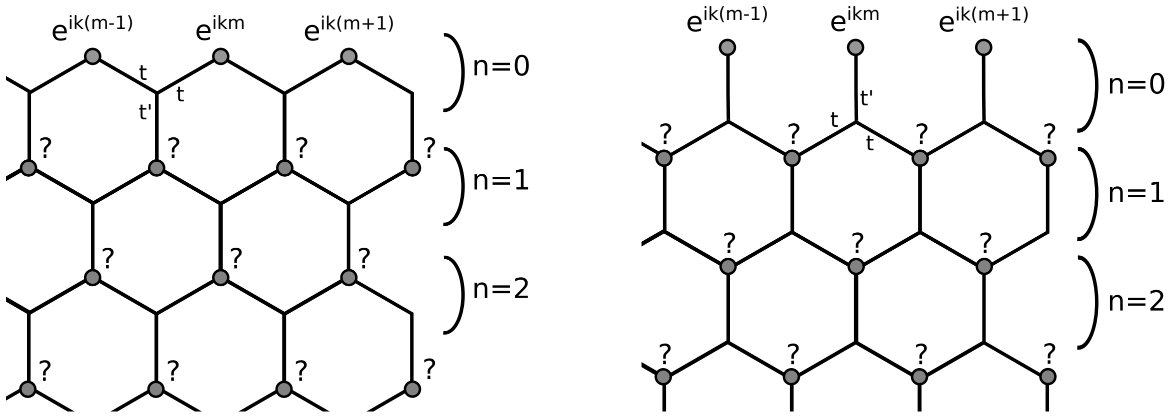

Fig. 2.13 Lower (left) and upper (right) half-planes, respectively with zigzag and 'bearded' edges made of atoms B.

edge states in this limit. In a similar manner, the wavefunction components $b^{(u)}$ in the upper half-plane are given by

$$b^{(u)}_{m,n} = \left(-\frac{2}{\alpha}\cos\frac{k}{2}\right)^{-n} e^{ik(m+\frac{n}{2})} \ . \tag{2.70}$$

The evanescent modes require $|2\cos(k/2)| > \alpha$. It leads to a range of complementary values for the momentum $0 < k < 2Q_c$ or $2(\pi - Q_c) < k < 2\pi$. Importantly, there are no evanescent modes in the upper half-plane in the insulating phase ($\alpha \geq 2$). It is a crucial point that will enable a direct evaluation of the impurity state.

The condition that the impurity wavefunctions on the two semi-infinite planes match at the interface can be written as

$$\alpha B^{(l)}_{m,0} + B^{(u)}_{m,0} + B^{(u)}_{m+1,0} = 0 \ , \tag{2.71}$$

where B labels the impurity wavefunction components and differs from b a priori.The above relation is valid everywhere on the edges except for $m = 0$, since it refers to the vacancy position. Introducing $B_{m,0} = \sum_k B_{k,0} e^{ikm}$, the condition (2.71) can be rewritten in terms of momentum as

$$\alpha \sum_k B^{(l)}_{k,0} e^{ikm} + \sum_k B^{(u)}_{k,0}(1 + e^{ik}) e^{ikm} = 0 \ . \tag{2.72}$$

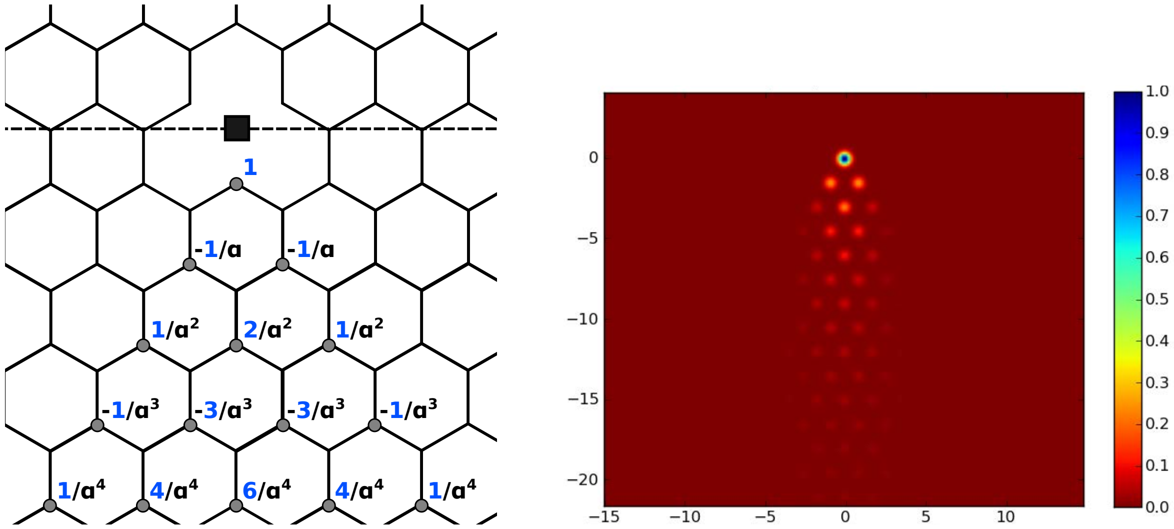

Fig. 2.14 Zero-energy wavefunction components (left) and impurity state obtained numerically (right) in the insulating phase.

A possible solution for the boundary solution is

$$\begin{cases} \alpha B^{(l)}_{k,0} = 1, & 2Q_c < k < 2(\pi - Q_c) \\ B^{(u)}_{k,0}\,(1+e^{ik}) = 1, & 0 < k < 2Q_c \;\; and \;\; 2(\pi - Q_c) < k < 2\pi \,. \end{cases} \tag{2.73}$$

As for the case of isotropic graphene studied in Ref. [62], this solution corresponds to the edge solutions for two isolated complementary semi-infinite planes. This implies that the impurity wavefunction can be expressed as a linear combination of the edge states given by (2.69) and (2.70). Focusing on the lower half-plane, it yields

$$B^{(l)}_{m,n} \simeq \sum_{k=2Q_c}^{2(\pi-Q_c)} \left(-\frac{2}{\alpha}\cos\frac{k}{2}\right)^n e^{ik(m+\frac{n}{2})} \,. \tag{2.74}$$

Before computing the above integral, we can already discuss what happens in the insulating phase, where the impurity state lies within the band gap. As already mentioned, Q_C is null for $\alpha \geq 2$, and there is no evanescent mode in the upper half-plane. In other words, all the electrons are all localised on sublattice B in the lower-half plane. The impurity wavefunction components are null everywhere else. The condition (2.71) becomes $\alpha B^{(l)}_{m,0} + 0 + 0 = 0$ and must be satisfied along the black dashed line in Fig. 2.14, except for the impurity site. So the wavefunction has zero components along the zig-zag edge, except at the site situated right under the impurity, for which we take $B^{(l)}_{0,0} = 1$. Then the Hamiltonian (2.65) implies that $\alpha B^{(l)}_{m,1} + B^{(l)}_{m,0} + B^{(l)}_{m+1,0} = 0$ for all values of m. This leads to

$B^{(l)}_{-1,1} = B^{(l)}_{0,1} = -1/\alpha$ and $B^{(l)}_{m,1} = 0$ for all other sites with $n = 1$. If we extend this analysis to the subsequent rows, we obtain the impurity wavefunction values shown in Fig. 2.14. So above the merging point, the zero-energy electrons are all localised in a triangle 'under' the vacancy, which seems in agreement with numerical exact diagonalisation [19]. Besides note that, due to the lattice geometry, this peculiar state reveals the Pascal's triangle corresponding to the blue numbers in the figure, as also mentioned recently in [70] and [71].

2.6.3 Zero-energy bound-state evaluation

Considering that the lattice as infinite, the discrete sum in (2.74) turns into an integral, and the impurity wavefunction can be written as

$$B^{(l)}_{m,n} \simeq \int_{2Q_c}^{2(\pi-Q_c)} dk \Big(-\frac{2}{\alpha}\cos\frac{k}{2}\Big)^n e^{ik(m+\frac{n}{2})} \,. \tag{2.75}$$

For large values of n, i.e. at large distances, only the largest values of the cosine need to be considered in the integral. This occurs in the vicinity of Q_c and $\pi - Q_c$. We assume that the cutoff parameter which controls this approximation is k_c

$$B^{(l)}_{m,n} \simeq \int_{Q_c}^{Q_c+k_c} dk \Big(-\frac{2}{\alpha}\cos k\Big)^n e^{ik(2m+n)} + \int_{\pi-Q_c-k_c}^{\pi-Q_c} dk \Big(-\frac{2}{\alpha}\cos k\Big)^n e^{ik(2m+n)} \tag{2.76}$$

A Taylor expansion of the cosine around the momenta Q_c yields $\cos(Q_c + q) = \cos(Q_c)[1 - q\tan(Q_c) - q^2/2] + o(q^2)$. Note that the first order term is non-zero only for $\alpha < 2$. In this case we can limit ourselves to the first order approximation

$$\begin{aligned} B^{(l)}_{m,n} &\simeq \int_0^{k_c} dq (-1)^n e^{-n\tan(Q_c)q} e^{iq(2m+n)} e^{iQ_c(2m+n)} + \int_0^{k_c} dq (-1)^{2n} e^{n\tan(\pi-Q_c)q} e^{-iq(2m+n)} e^{i(\pi-Q_c)(2m+n)} \\ &\simeq \int_0^{\infty} dq (-1)^n e^{-n\tan(Q_c)q} e^{iq(2m+n)} e^{iQ_c(2m+n)} + \int_0^{\infty} dq e^{-n\tan(Q_c)q} e^{-iq(2m+n)} e^{i(\pi-Q_c)(2m+n)} \\ &\simeq (-1)^n \frac{e^{iQ_c(2m+n)}}{\tan(Q_c).n - i(2m+n)} + \frac{e^{i(\pi-Q_c)(2m+n)}}{\tan(Q_c).n + i(2m+n)} \,. \end{aligned} \tag{2.77}$$

Introducing the cartesian coordinates $x = a_0\sqrt{3}(2m+n)/2$ and $y = -n3a_0/2$, with a_0 nearest-neighbour distance, leads to

$$B^{(l)}(x,y) \simeq \frac{e^{i2Q_c x/\sqrt{3}+2i\pi y/3}}{-\tan(Q_c)y/3 - ix/\sqrt{3}} + \frac{e^{i2(\pi-Q_c)x/\sqrt{3}}}{-\tan(Q_c)y/3 + ix/\sqrt{3}} \,. \tag{2.78}$$

In the semimetallic phase, the vacancy induces a localised state at zero-energy that decays algebraically as $1/r$, albeit exhibiting a strong asymmetry between x and y. Here $\mathbf{r} = \left(2x/\sqrt{3},\ 2\tan(Q_c)y/3\right)$. In the case of isotropic graphene ($Q_c = \pi/3$),

$$B^{(l)}(x,y) \simeq a_0\sqrt{3}\frac{e^{i2\pi(-y+x/\sqrt{3})/(3a_0)}}{-y-ix} + a_0\sqrt{3}\frac{e^{i4\pi x/(3\sqrt{3}a_0)}}{-y+ix} \,, \tag{2.79}$$

and we recover the result of [62] by doing the substitution $x \to y$ and $-y \to x$.

For $\alpha \geq 2$ however, $Q_c = 0$. The first order terms in the above expansions vanish and we need to consider the second order corrections. It leads to

$$\begin{aligned} B^{(l)}(x,y) &\simeq \int_0^{k_c} 2dq(-2/\alpha)^n e^{-n\frac{q^2}{2}} e^{iq(2m+n)} + \int_0^{k_c} dq(-2/\alpha)^n e^{-n\frac{q^2}{2}} e^{-iq(2m+n)} \\ &\simeq (-2/\alpha)^n e^{-\frac{(2m+n)^2}{2n}} \int_0^{\infty} dq e^{-\frac{n}{2}(q+i\frac{2m+n}{n})} + (-2/\alpha)^n e^{-\frac{(2m+n)^2}{2n}} \int_0^{\infty} dq e^{-\frac{n}{2}(q-i\frac{2m+n}{n})} \\ &\simeq (-1)^n \frac{e^{-nln(\frac{\alpha}{2})-\frac{(2m+n)^2}{2n}}}{\sqrt{n}} \\ B^{(l)}(x,y) &\simeq \frac{e^{2yln(\frac{\alpha}{2})/3+\frac{x^2}{y}}}{\sqrt{|y|}} e^{2i\pi y/3} \,. \end{aligned} \tag{2.80}$$

Thus, the localised wavefunction decays exponentially in the insulating phase ($y < 0$). Indeed, y is negative in the lower half-plane. Right at the Dirac cone merging transition, the wavefunction exhibits an algebraic decay as $1/\sqrt{|y|}$ (assuming $y \gg x^2$) [19]. It means the LDOS, which is given by the modulus squared of the wavefunction, is zero in the upper half-plane and decays as $1/|y|$ in the lower half-plane. This is in agreement with our findings in the Friedel oscillations section dealing with semi-Dirac electrons. Indeed, the T-matrix approach for a vacancy led to a vanishing LDOS on the sublattice A, whereas on the sublattice B the LDOS correction was found to be

$$\Delta\rho_B(0,y,\omega \to 0) \sim \frac{\theta(-y)}{y} \,. \tag{2.81}$$

Once again, the form of the decay for the zero-energy impurity states provides a real-space signature of the Dirac-cone merging transition. Importantly, remark that the phase θ_q and the chirality are not defined at zero-energy, and thus, are not responsible for the distinct features of the zero-energy impurity state. Since this transition has already been observed in the case of artificial honeycomb lattices [47–49], the impurity state induced by a missing site (vacancy) becomes particularly relevant experimentally.

The table below summarises the possible spatial decays of the zero-energy vacancy-induced wavefunction.

Phase	semimetallic	semimetallic	insulating
Dispersion relation	conical	semi-conical	parabolic
$B(x,y)$	$1/r$	$1/\sqrt{\lvert y\rvert}$	$e^{2y\ln(\alpha/2)/3+x^2/y}$

Note finally that the sublattice symmetry is not mandatory in the above discussion. This symmetry can be broken in systems such as boron nitride. The two nonequivalent atoms, namely A and B, respectively correspond to boron and nitrogen atoms. In a nearest-neighbour tight-binding description, Hamiltonian (2.65) changes to

$$H = \begin{pmatrix} \mu.\mathbb{I}_{N_A} & T \\ T^\dagger & -\mu.\mathbb{I}_{N_B} \end{pmatrix} . \tag{2.82}$$

The distinction between boron and nitrogen atoms is simulated by opposite on-site energies ($\pm\mu$). Due to these intra-sublattice terms, the system is no longer bipartite. In the case of a vacancy on the sublattice B, the form of the induced-impurity state, which emerges at zero energy in regular graphene, remains unchanged, except that in boron nitride it forms at energy $-\mu$. In the same manner, a single vacancy on the sublattice A would induce a similar state at energy $+\mu$.

Chapter 3

Topological boundary modes

The characterisation of condensed phases of matter took a serious step with Landau's theory of phase transitions [72]. Unlike the glass transition and Berezinsky-Kosterlitz-Thouless transition, classical and quantum second-order transitions occur when a collective order of the many-body system spontaneously breaks continuous or discrete symmetries, such as the spin rotation symmetry in magnets, the translational symmetry in Peierls structural transition, the gauge symmetry in Bose condensation and BCS superconductivity, etc.

The present chapter deals with the more recent concept of *symmetry protected topological order*. The discussion of this type of order has begun in connection to the discovery of the integer quantum Hall effect in the early eighties [10, 73], followed by the topological characterisation of its measurable quantised Hall conductance that ensures the presence of chiral edge channels [11]. More generally, symmetry protected topological order is about systems that have a bulk energy gap and preserve a given symmetry, namely topological insulators and superconductors. As long as this symmetry is preserved, a topological characterisation of the system becomes possible, and can then be related to the existence of boundary modes within the energy gap. For non-interacting particles, as it will be the case all along the present chapter, the existence of such boundary modes relies on the topology of the Bloch band-structure of the single-particle Hamiltonian that describes the system. Under the preserved symmetry, distinct topological phases cannot be continuously deformed into each other without a phase transition, which requires an energy-gap closing. Since topological properties ensure their existence, the boundary modes are therefore expected to be robust against any disorder that does not close the energy-gap and preserves the given symmetry. In other words, the existence of boundary modes within the energy-gap is guaranteed by topological properties of the band structure, which are themselves protected by a preserved symmetry. This has to be distinguished from the notion of *topological order* introduced by

X. G. Wen in [74], where this is the degeneracy of the many-body ground-state that is topologically protected, without requiring such a preserved symmetry. For instance spin liquids [75] and the fractional quantum Hall effect [76] both manifest a topological order.

In order to highlight how symmetry, topology and robust boundary modes intervene in symmetry protected topological systems, we begin this chapter with the generalisation of an old *one-dimensional two-band topological insulator*, namely the Shockley model [20]. It offers the benefit to be illustrative, exactly solvable, and quite universal [22]. Although it was subsequently discussed in the literature [21, 22], it was only considered within a nearest-neighbour tight-binding limit. Here, we also consider arbitrary distant-neighbour hopping processes and show that this extension allows the system to reach new topological phases that are characterised by an arbitrary large number of edge states.
After saying a few words about the topological classification of single-particle gapped Hamiltonians [77], we will see that even in the case of *semimetals, gapless systems like graphene*, the edge-state emergence finds a topological explanation, via a dimensional reduction. As a simple illustration, we will consider a zigzag graphene nanoribbon and also investigate the robustness of its edge states agains local disorder such as point defects [23].

The second half of this chapter mainly focuses on the analysis of a *two-dimensional eight-band topological superconductor*, whose zero-energy boundary modes are Majorana modes [24]. The considered system relies on a honeycomb lattice in the presence of spin-singlet superconductivity, magnetic field induced Zeeman splitting and Rashba spin-orbit interactions. So far the literature has only focused on monatomic pattern lattices, or more generally on systems where the topological characterisation does not depend on the spin-orbit interactions. In the case of a honeycomb lattice, we show that the diatomic pattern directly affects the topological phases via the magnitude of these interactions. We also give a prescription to access the topological properties of this eight-band system [25], and thus predict the emergence of zero-energy Majorana modes that are localised at the edges of doped and strained nanoribbons.

3.1 A generalised Shockley model

3.1.1 On the topology of the Bloch band structure

As an illustrative introduction to topological systems, we consider the one-dimensional two-band model of a dimerised Peierls chain. It is the underlying model Su, Schrieffer and Heeger used to explain the formation of solitons as topological excitations in polyacetylene [21]. But this model also refers to the anterior work of Shockley [20] in which he discussed, from the atomic level, the surface states in semi-infinite crystals predicted by Tamm [78]. This is the subject of the subsequent paragraphs, where the formation of spinless surface states is extended here to a distant-neighbour tight-binding analysis. The Hamiltonian matrix of the infinite system in momentum space is generically written as

$$H(k) = h_0(k)\sigma_0 + h_1(k)\sigma_1 + h_2(k)\sigma_2 + h_3(k)\sigma_3 \,, \tag{3.1}$$

where σ_i refers to the Pauli matrices. The system preserves the time-reversal symmetry, which requires $H^*(k) = H(-k)$. So every component is an even function of the momentum, except h_2 which is odd. Less importantly, intra-sublattice processes h_0 are neglected here for simplicity. Although such a process would break the particle-hole symmetry, it would not change neither the (direct) gap closing condition of the spectrum, nor the eigenstates, that are two crucial points when dealing with topological matter. Finally, it is assumed that $h_3 = 0$ too. Thus, the two sublattices remain equivalent and the system preserves the chiral (or sublattice) symmetry given by the anticommutation relation $\{H(k), \sigma_3\}$=0. As already mentioned, the chiral symmetry leads to a particle-hole symmetric spectrum, but even when this symmetry is broken, the relation $\sigma_2^* H^*(k) \sigma_2^* = -H(k)$ requires the spectrum to be particle-hole symmetric. Under those conditions, the only non-null components in the Hamiltonian matrix are the off-diagonal ones

$$\begin{aligned} h_1(k) &= t_1 + \sum_{n=1}^{\frac{N-1}{2}} \big(t'_{2n-1} + t_{2n+1}\big) \cos(nk) + t'_N \cos\big(\frac{N+1}{2}k\big) \\ h_2(k) &= \sum_{n=1}^{\frac{N-1}{2}} \big(t'_{2n-1} - t_{2n+1}\big) \sin(nk) + t'_N \sin\big(\frac{N+1}{2}k\big) \,, \end{aligned} \tag{3.2}$$

where t_n (t'_n) denotes the hopping amplitude between a certain site and its n-th nearest neighbour on its right (left), according to Fig. 3.1. Here N refers to the highest order hopping process allowed in the model. It is necessarily an odd integer, since only inter-sublattice couplings are taken into account. Introducing the complex off-diagonal component $h = h_1 + ih_2$ and its argument θ, the band structure of the dimerised chain is given by

$$E(k) = \pm|h(k)| \,, \quad \langle\psi_\pm(k)| = \left(1, \ \pm e^{i\theta_k}\right) \,. \tag{3.3}$$

Importantly, we are limiting the band structure, or equivalently the Hamiltonian matrix, to a periodic Brillouin zone (BZ), thus Bloch's theorem implies $H(k+G) = H(k)$, with G a reciprocal lattice vector. As long as there is an energy gap separating the conduction and the valence bands, θ_k remains well defined. It is then possible to define a mapping from the BZ, a one-dimensional sphere S^1, to the space of gapped Bloch Hamiltonians, restricted by the chiral symmetry to the equator of the Bloch sphere, which is also a one-dimensional sphere S^1. For such gapped Hamiltonians which respect the chiral symmetry, the question is to know whether they are equivalent or not, whether the mappings they define can be continuously deformed into one another or not. If the answer is yes, the mappings are said to be homotopic. It defines equivalence classes, called homotopy classes, that form a group. They are examples of topological invariants. The case we are considering concerns mappings from a circle S^1 to another circle S^1 and $\pi_1(S^1)$ denotes the corresponding homotopy group. It is the simplest case of spheres homotopy groups that describe how spheres can wrap around each other. As far as we are concerned the wrapping is given by counting the number of times θ_k wraps around the circle when k runs over the whole BZ. This number, also called winding number, is an integer that characterises the homotopy class. This is the reason why $\pi_1(S^1) = \mathbb{Z}$, and the topological invariant is defined as

$$W = \frac{1}{2\pi} Im \int_{BZ} dk \, \partial_k \ln h(k). \tag{3.4}$$

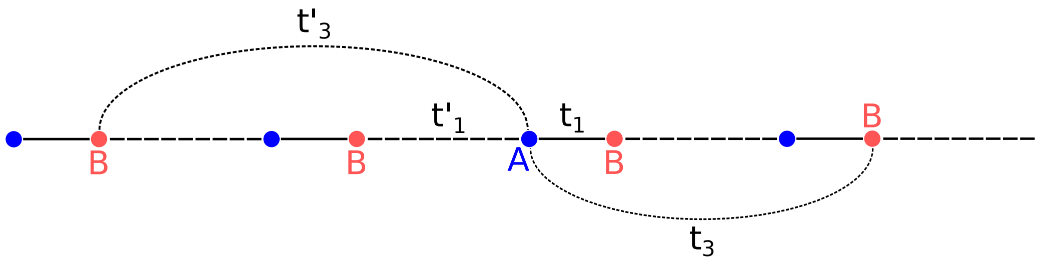

Fig. 3.1 One-dimensional dimer chain with the four intrasublattice hopping processes (black lines) allowed for $N = 3$.

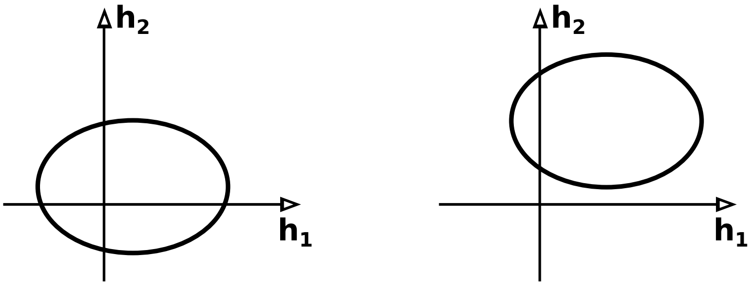

Fig. 3.2 Illustrations of two nonequivalent closed paths that $h(k)$ is likely to outline.

Here $h(k)$ is a complex number and the above integer simply reduces to

$$W = \frac{1}{2\pi} \int_{BZ} dk \, \partial_k \theta_k \; . \tag{3.5}$$

A geometrical interpretation of this winding number is illustrated in Fig. 3.2. Since θ_k is the argument of $h(k)$, the topological invariant is given by counting the number of times the closed path drawn by $h(k)$ encloses the complex-plane origin. To compute this integer, it is not necessary to know the behavior of $h(k)$ along the curve described by it. For any k_n satisfying $h_1(k_n) = 0$, it is usually sufficient to know the sign of $h_2(k_n)$ and the direction $h(k)$ is going in. The later is given by the sign of the speed of $h_1(k_n)$. Therefore, the winding number can be computed from a discrete sum instead of an integral

$$W = \frac{1}{2} \sum_{k_n} \; \mathrm{sgn}\, h_2(k_n) \; \mathrm{sgn}\, \partial_k h_1(k_n) \; . \tag{3.6}$$

Of course, an equivalent expression is obtained when defining k_n using $h_2(k_n) = 0$.

3.1.2 Chiral symmetry and zero-energy modes

As mentioned above, the role played by the chiral (sublattice) symmetry is fundamental in the topological characterisation of the one-dimensional band structure. If this symmetry is broken, the mapping is defined from the BZ (S^1) to the entire two-dimensional Bloch sphere (S^2), and it is no longer restricted to the Bloch sphere equator. The one-dimensional closed path drawn by $|\psi_\pm\rangle$ on S^2 can be continuously deformed to a point. So the relative homotopy group is trivial, meaning $\pi_1(S^2) = 0$. More generally, any mapping from a p-dimensional sphere into a q-dimensional sphere is trivial when $p < q$, so that $\pi_p(S^q) = 0$.

The chiral operator S, which squares to the identity $S \times S = 1$, and anticommutes with the Hamiltonian $\{S,H\}=0$, acts onto the wavefunctions as

$$S|A,B\rangle = |A,-B\rangle \ , \tag{3.7}$$

where A (resp. B) within the bra-ket is a set of wavefunction components referring to the sublattice A (resp. B). Thus the transformation S consists in reversing all the signs of the wavefunction components on one sublattice that is the sublattice B here. It also implies the particle-hole symmetry

$$\begin{aligned} H\ |A,B\rangle &= E\ |A,B\rangle \\ H\ S|A,B\rangle &= -E\ S|A,B\rangle \ , \end{aligned} \tag{3.8}$$

where $|A,B\rangle$ is an eigenstate of the Hamiltonian. Any non-zero energy state has its own pair with opposite energy. An interesting situation occurs when focusing on the zero-energy states. Such states are necessarily eigenstates of the operator S, whose eigenvalues are ± 1. From the definition (3.7), it is clear that the zero-energy states have null components on one sublattice and verify

$$\begin{aligned} S|A,0\rangle &= |A,0\rangle \\ S|0,B\rangle &= -|0,B\rangle \ . \end{aligned} \tag{3.9}$$

Reciprocally, it is obvious that any eigenstate of the Hamiltonian such as $|A,0\rangle$ or $|0,B\rangle$ are zero-energy modes. It means that the chiral symmetry enables the distinction between two families of zero-energy states depending on their 'chirality' (eigenvalue ± 1), or equivalently, depending on the sublattice they refer to.

When the system belongs to an insulating phase, meaning there is a bulk energy gap as in Fig. 3.3, some of the zero-energy states are protected by the chiral symmetry. In the figure, two distinct cases arise. First, two zero-energy states may have opposite chirality (red and blue colors), that is they refer to opposite sublattices. In this case, any continuous perturbation is likely to make them hybridise (if they are not far apart in real space) and then move away from zero energy, resulting in two states with opposite non-null energies. Second, it may happen that there is an imbalance between the number of positive and negative chirality zero-energy states. The figure illustrates this point in the case of two zero-energy states (in blue) having the same chirality. Because they live on the same sublattice, they necessarily stay at zero energy, as long as no perturbation breaks the chiral symmetry, or equivalently as long as the system remains bipartite. The only way to make them leave the zero-energy

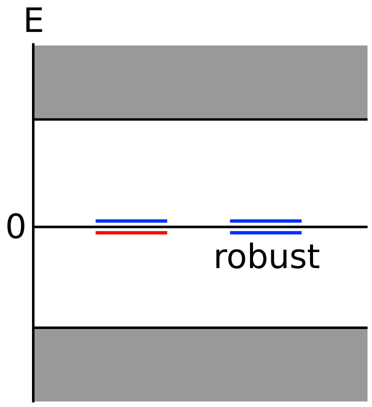

Fig. 3.3 Illustration of zero-energy states within the bulk energy gap (in white). Blue and red colors describe states of opposite chirality.

level without breaking this symmetry is to close the gap. That is why such states are said to be robust, or symmetry protected.

Therefore, the number of robust zero-energy modes cannot change under the chiral symmetry, except if the energy gap closes.

3.1.3 Bulk-edge correspondence

In what follows, we present the connection there exists between the topological number W and the number of robust zero-energy modes. This is more commonly known as bulk-edge correspondence, for it relates the topological invariant, which is defined from the bulk band structure, to the number of edge states living at a boundary with the vacuum.

On the one hand, let us determine the winding number as a function of the model parameters. From its definition (3.4), it can be rewritten as

$$W = \frac{1}{2i\pi} \int_{\mathscr{C}} dz \, \frac{h'(z)}{h(z)} \, , \tag{3.10}$$

where we define $z = e^{ik}$, so that $\mathscr{C}$ is the unit circle enclosing the complex-plane origin. In complex analysis, this integral is given by the Cauchy's argument principle, states that the above integral is given by the difference between the number of zeros (r) and poles (p) of the function h, that are located inside the closed contour $\mathscr{C}$. Consequently,

$$W = r - p \, . \tag{3.11}$$

Based on the definitions (3.2), the function h is given by

$$\begin{aligned} h(z) &= t_1 + t_1'\, z + t_3\, z^{-1} + t_3'\, z^2 + ... + t_N\, z^{-\frac{N-1}{2}} + t_N'\, z^{\frac{N+1}{2}} \\ &= z^{-\frac{N-1}{2}} \left(t_N + ... + t_N'\, z^N\right) \end{aligned} \tag{3.12}$$

So $z = 0$ is the only pole of h with multiplicity $(N-1)/2$. It leads to $p = (N-1)/2$, whereas the zeros located inside $\mathscr{C}$ are obtained from the roots of the polynomial $t_N + ... + t_N'\, z^N$.

On the other hand, let us consider the system as semi-infinite, which means there is a boundary with the vacuum according to Fig. 3.1. The following independent recurrence relations define the zero-energy modes

$$\left\{ \begin{array}{l} t_1 A_n + t_1' A_{n+1} + t_3 A_{n-1} + t_3' A_{n+2} + ... + t_N A_{n-\frac{N-1}{2}} + t_N' A_{n+\frac{N+1}{2}} = 0 \\ t_1 B_n + t_1' B_{n-1} + t_3 B_{n+1} + t_3' B_{n-2} + ... + t_N B_{n+\frac{N-1}{2}} + t_N' B_{n-\frac{N+1}{2}} = 0 \end{array} \right. , \tag{3.13}$$

where A_n (B_n) denotes the wavefunction component on the sublattice A (B) for the dimer indexed by n. Solutions of (3.13) are obtained from the solutions, denoted z_i, of the characteristic equations

$$\left\{ \begin{array}{l} h(z_i) = 0 \\ h^*\left(\frac{1}{z_i}\right) = 0 \end{array} \right. . \tag{3.14}$$

If z_i is a root of h, then $1/z_i^*$ is a root of h^*, so that the wavefunction components are

$$\left\{ \begin{array}{l} A_n = \sum_{i=1}^{N} \alpha_i\, z_i^n \\ B_n = \sum_{i=1}^{N} \beta_i \left(\frac{1}{z_i^*}\right)^n \end{array} \right. , \tag{3.15}$$

where α_i and β_i are two complex numbers. When keeping only the evanescent modes, which correspond to $|z_i| < 1$ for A_n and $|1/z_i^*| < 1$ for B_n, the zero-energy modes satisfy

$$\left\{ \begin{array}{l} A_n = \sum_{i=1}^{r} \alpha_i\, z_i^n \\ B_n = \sum_{i=1}^{N-r} \beta_i \left(\frac{1}{z_i^*}\right)^n \end{array} \right. . \tag{3.16}$$

There are r (resp. $N-r$) independent zero-energy modes on sublattice A (resp. B). They additionally fulfil N_A and N_B boundary conditions respectively, where $N_A + N_B = N$ and $N_B = N_A + 1$. This can be checked from Fig. 3.1. It leads to $N_A = p$ and $N_B = p + 1$. Under those constraints, we are left with $r - p$ (resp. $p - r$) independent zero-energy edge states on sublattice A (resp. B).

The number of zero-energy edge states can be directly related to W via the relation (3.11), which establishes the bulk-edge correspondence of our model:

- if $W > 0$ there are $|W|$ robust edge states on the sublattice A (chirality $+1$)
- if $W < 0$, there are $|W|$ robust edge states on the sublattice B (chirality -1)
- if $W = 0$ there is no edge state and the system belongs to a trivial gapped phase.

Note that the topological invariant is limited by the highest hopping process allowed in the model, namely N, in the following way

$$-\frac{N-1}{2} \leq W \leq \frac{N+1}{2} \ . \tag{3.17}$$

Actually, this is the main idea addressed in [32]. The authors consider distant-neighbour hopping in the Haldane model [13], in order to explore topological phases characterised by an arbitrary large Chern number. We will encounter such a topological invariant later on.

3.1.4 Application and robustness against disorder

As an application, we consider the above model with hopping processes allowed up to the third nearest-neighbour. If $N = 1$, then the inequality (3.17) involves their is either one edge state on the sublattice A or none at all. The situation is much more interesting when $N = 3$. Indeed, the winding number is restricted to values $\{-1, 0, 1, 2\}$. It means that, for the edge given in Fig. 3.1, the system can exhibit up to two evanescent modes on the sublattice A, or one evanescent mode on the sublattice B. In order to evaluate the winding number of the system according to expression (3.6), we first look for the roots of

$$h_2(k) = (t_1' - t_3)\sin(k) + t_3' \sin(2k) \ . \tag{3.18}$$

Obviously, 0 and π are two roots regardless of the hopping amplitudes. Two more roots do exist when $|t_3 - t_1'| < 2t_3'$, which finally leads to the four roots

$$\begin{cases} k_1 = 0 \\ \pm k_2 = \pm \arccos\left(\frac{t_3 - t_1'}{2t_3'}\right) \\ k_3 = \pi \end{cases} \ . \tag{3.19}$$

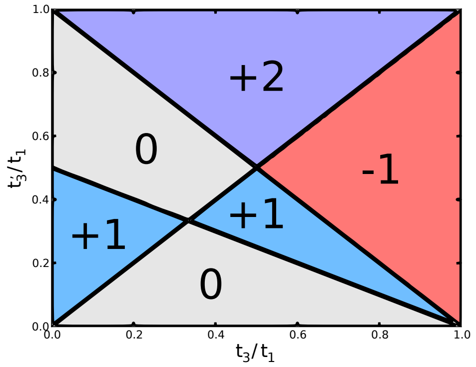

Fig. 3.4 Phase diagram of the third nearest-neighbour model and possible winding number values.

For such momenta, the derivatives of h_2 are

$$\begin{cases} \partial_k h_2(k_1) = t_1' - t_3 + 2t_3' \\ \partial_k h_2(\pm k_2) = -2t_3' \\ \partial_k h_2(k_3) = t_3 - t_1' + 2t_3' \end{cases}, \tag{3.20}$$

while the function h_1 takes the following values

$$\begin{cases} h_1(k_1) = t_1 + t_1' + t_3 + t_3' \\ h_1(\pm k_2) = \frac{(t_1 - t_3')t_3' + (t_3 - t_1')t_3}{t_3'} \\ h_1(k_3) = t_1 - t_1' - t_3 + t_3' \end{cases}. \tag{3.21}$$

Their signs are summed up in the table below, when assuming that all the hopping amplitudes are positive.

	k_1	k_2	k_3
$\partial_k h_2$	$+$	$-$	$+$
h_1	$+$	$\pm$	$\pm$

Moreover we restrict ourselves to $t_1 = t_1'$ for simplicity, so that

$$\begin{cases} \operatorname{sgn} h_1(k_2) = \operatorname{sgn}(t_1 - t_3 - t_3') \operatorname{sgn}(t_3' - t_3) \\ \operatorname{sgn} h_1(k_3) = \operatorname{sgn}(t_3' - t_3) \end{cases}. \tag{3.22}$$

The possible values of the winding number can be summarised as follows

- $t_3 - t_1 > 2t_3'$ and $W = \frac{1}{2}\left[1 + \operatorname{sgn}(t_3' - t_3)\right] \in \{0, +1\}$

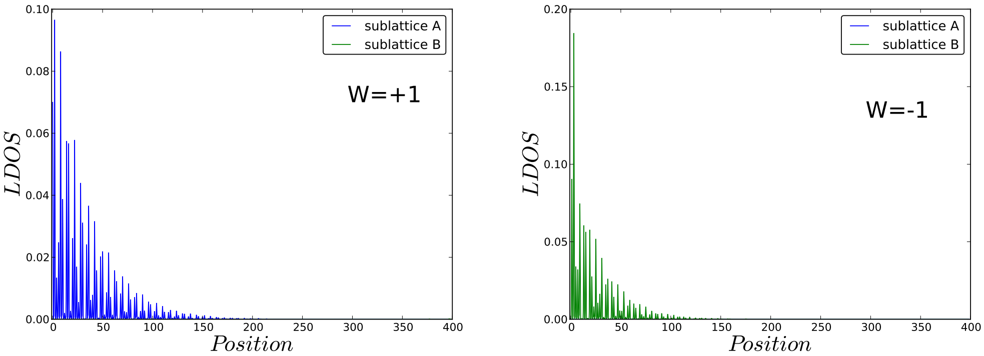

Fig. 3.5 Zero-energy LDOS for $W=+1$ (left, $t_3=0.5t_1$ and $t_3'=0.4t_1$) and $W=-1$ (right, $t_3=0.7t_1$ and $t_3'=0.4t_1$) in the case of a 400 site chain.

- $t_3-t_1<2t_3'$ and $W=\frac{1}{2}\Big[1+\big(1-2\,\mathrm{sgn}(t_1-t_3-t_3')\big)\,\mathrm{sgn}(t_3'-t_3)\Big]\in\{-1,0,+1,+2\}$.

They are represented in a phase diagram as a function of the third nearest-neighbour hopping in Fig. 3.4. The border (black lines) between two distinct topological phases correspond to a gap closing condition, i.e. the energy gap vanishes for these values of the parameters. This is an obstruction in the definition of the mapping $S^1\to S^1$. Since $|h(k)|=0$, the argument θ_k becomes ill-defined and so does W, which enables this integer to change values in a discontinuous way.

Besides, Fig. 3.5 illustrates the property of W that its sign refers to the sublattice, or equivalently to the chirality of the zero-energy modes. We plot the LDOS, which is simply the modulus square of the single ($|W|=1$) zero-energy wavefunction, in the case of a 200 dimers chain. Of course numerical computations require a finite chain that has consequently two ends, so two boundaries with the vacuum. Regarding the edge lying on the left of the system (see Fig. 3.1), one recovers indeed an evanescent mode on sublattice A (B) when $W=+1$ ($W=-1$).

We would like to end this section touching upon the edge-states robustness against disorder. This is a fundamental issue since the topological arguments usually rely on the periodicity of the Bloch band structure, allowed by the crystal translational invariance. Nevertheless, we have seen the system cannot move from a topological phase to another continuously. For this reason, the zero-energy modes are expected to be robust against any disorder that respects the chiral symmetry. This is illustrated in Fig. 3.6 in the case of $W=+2$. For such a value of the winding number, there are two edge states on the same sublattice per boundary. Thus, four zero-energy modes are expected for a finite system with two ends made of one atom A and one atom B respectively. For the left-figure plot, the disorder respects the chiral symmetry for it is simulated by random fluctuations δt_i in the hopping parameters such that

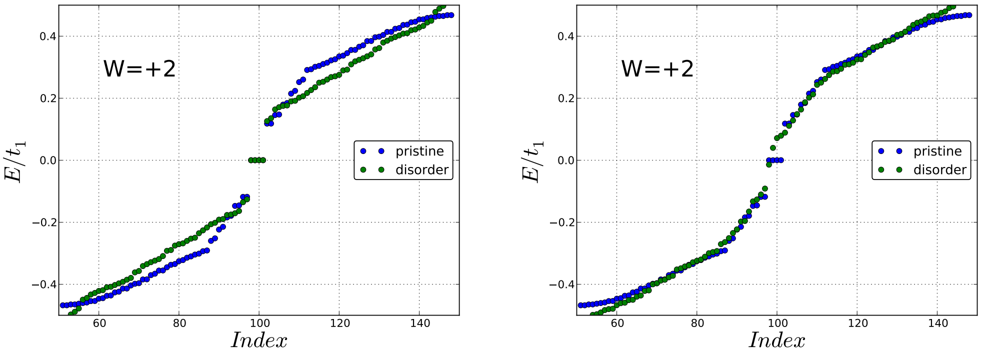

Fig. 3.6 Dimerised chain spectrum for W=+2 ($t_3 = 0.5t_1$ and $t_3' = 0.4t_1$), in presence of random hopping amplitudes (left) and random on-site potentials (right).

$|\delta t_{i=1,3}| \leq 0.2t_{i=1,3}$. Although the bulk spectrum is affected by the disorder, the zero-energy modes persist as long as the energy gap persists. For right-figure plot however, the disorder breaks the chiral symmetry, since it is simulated by random on-site potential $\delta\mu$ such that $|\delta\mu| \leq 0.2t_1$. In this case, not only the bulk spectrum is affected, but the zero-energy states are not protected anymore by the chiral symmetry. They are then allowed to move away from the zero energy, even if the gap does not close. In this sense, the edge states addressed in the generalised Shockley model can be topologically characterised only if the chiral symmetry is not broken, as already mentioned by Kane [79] about the quite similar model of Su, Schrieffer and Heeger.

Finally, it is sometimes noted in the literature that considering opposite constant on-site potentials $\pm\mu$ on the two sublattices removes the zero-energy degeneracy by shifting the edge modes up (down) to energy $\pm\mu$ [22, 80]. The resulting edge states are still within the bulk energy gap, but they immediately move away from these energies as soon as random on-site potential fluctuations are introduced, since this is not forbidden by any symmetry. Therefore, the $\pm\mu$-energy edge-states are not protected in this case.

3.2 Intermezzo: topological insulators & superconductors

Since the above study is based on a specific 'toy' model, it is natural to wonder to what extent it applies to other systems. In other words, to what extent the existence of boundary modes can be predicted from the band-structure topology of a gapped Bloch Hamiltonian? The answer actually relies on Table 3.1 and depends on the affiliation to one of 10 symmetry classes [81], as well as on the system dimensionality.

Inspired by Wigner's ideas [82], Dyson started a classification of many-body systems whose statistical properties are described in terms of random-matrix ensembles [83]. This classification in three and subsequently in six categories was finally completed by the introduction of four symmetry classes encountered in noninteracting Bogoliubov-de Gennes (BdG) systems [81], so that, there would be ten possible universality classes for single-particle disordered systems. Three discrete symmetries, which resist disorder, generate the classification. They are the time-reversal symmetry (TRS), the particle-hole symmetry (PHS) and the composition of these two, which yields the chiral or sublattice symmetry (SLS). Operators representing those symmetries are respectively denoted T, C and $S = TC$. The antiunitary time-reversal and particle-hole operators, T and C, can square to ± 1. These symmetry can also be broken so that $T = 0$ or $C = 0$. Altogether these distinct values define nine possible classes. The tenth class (AIII) comes from the SLS which can be present even if the two other symmetries are absent.

		T	C	S	d=1	d=2	d=3
Standard (Wigner-Dyson)	A	0	0	0	-	$\mathbb{Z}$	-
	AI	$+1$	0	0	-	-	-
	AII	-1	0	0	-	$\mathbb{Z}_2$	$\mathbb{Z}_2$
Chiral (sublattice)	AIII	0	0	1	$\mathbb{Z}$	-	$\mathbb{Z}$
	BDI	$+1$	$+1$	1	$\mathbb{Z}$	-	-
	CII	-1	-1	1	$\mathbb{Z}$	-	$\mathbb{Z}_2$
BdG	D	0	$+1$	0	$\mathbb{Z}_2$	$\mathbb{Z}$	-
	C	0	-1	0	-	$\mathbb{Z}$	-
	DIII	-1	$+1$	1	$\mathbb{Z}_2$	$\mathbb{Z}_2$	$\mathbb{Z}$
	CI	$+1$	-1	1	-	-	$\mathbb{Z}$

Table 3.1 Periodic table of topological insulators and superconductors defined in [77].

Based on these symmetry classes, exhaustive classifications of single-particle gapped Hamiltonians were given [9, 77, 84] as a function of spatial dimensions (see Table 3.1). There are five topological classes per dimension. For any of these five classes, the gapped phase of the system is topologically characterised either by an integer ($\mathbb{Z}$) or by an integer parity ($\mathbb{Z}_2$). Since this integer, which is either a winding number or a Chern number, cannot change continuously, the energy gap necessarily closes at interfaces between regions that are characterised by distinct topological invariants. This guarantees the existence of gapless boundary modes. Note the insulating vacuum is characterised by a null topological invariant.

In the two-dimensional quantum Hall phase (class A), a non-zero TKNN number [11], or Chern number [13], which intervenes in the measurable Hall conductance, ensures the presence of chiral edge channels. Even if the TRS is preserved and if the system is characterised by a zero Chern number, it is possible to make electrons with opposite spins satisfy integer quantum Hall effects under opposite magnetic fields. Such a two-dimensional quantum spin Hall phase (class AII) was proposed by Kane and Mele and leads to helical edge modes characterised by a $\mathbb{Z}_2$ invariant [15, 85]. This work definitively injected enthusiasm into the field of topological insulators.

Although they belong to other classes in the Altland-Zirnbauer table of gapped Hamiltonians [81], namely the BdG ones, topological superconductors also exhibit robust boundary states. Such a topological order was predicted by A. Kitaev [14], in a one-dimensional time-reversal invariant model, considering p-wave pairing. Moreover, the zero-energy edge states, which emerge in the topological phase, are Majorana modes. These modes were first introduced in 1937 by E. Majorana [86] as real solutions of the Dirac equation. They will be discussed later in this chapter, but note they obey non-Abelian statistics, which would open the perspective of their use in topological quantum computation [87]. Moreover, Majorana modes were also investigated in spin-singlet superconductors [24, 88–90], provided the TRS is broken by a Zeeman splitting.

Consequently, the one dimensional generalised Shockley model introduced in the previous section is just a little piece of the topological classification (class BDI in Table 3.1), but it highlights a universal property it shares with both insulators and superconductors. The symmetries of the Hamiltonian enable the topological characterisation of its gapped band structure, which guarantees the existence of robust zero-energy modes at a boundary where the topological invariant changes. Note the topological invariants can be also expressed in terms of Green's function [91] , which is a convenient formalism for eventual extensions to interacting systems [92, 93].

3.3 Graphene edge-states

3.3.1 Topological characterisation

Graphene is a two-dimensional semimetal that exhibits a nodal dispersion relation. Consequently, it does not directly enter the topological classification of gapped systems presented in the previous section. However, there generally exist peculiar zero-energy localised states along the edges of graphene nanoribbons. In 1996, a few years before the graphene boom,

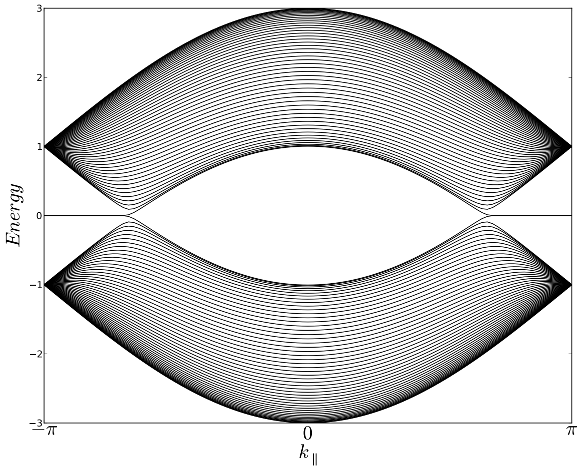

Fig. 3.7 Band structure of a zigzag graphene nanoribbon. The flat bands at zero energy correspond to the edge states and connect the two Dirac cones projection at momenta $k_{\|} = \pm\frac{2\pi}{3}$.

they were first predicted to appear at a zigzag graphite edge [7], using simple lattice considerations such as the ones discussed in Sec. 2.6. A topological explanation of these localised states at a zigzag termination was given six years later by Ryu and Hatsugai [33]. But it was only recently that the analysis of the zero-energy edge-state formation was generalised to arbitrary terminations [8], and then explained through topological arguments [34, 80]. Note that these arguments, which will be detailed below, similarly hold in the topological characterisation of nodal superconductors [94], systems in which the edge states are known as zero-energy Andreev bound states [95].

In presence of the SLS, the zero-energy edge-states of graphene find a topological characterisation through a *dimensional reduction* [9]. Given an arbitrary termination, the momentum along the edge $k_{\|}$ is a good quantum number and the tight-binding Hamiltonian matrix can be considered as describing an effective one-dimensional system for any value of this momentum $k_{\|}$. As an illustration, let us consider the simple case of the zigzag edge introduced in Fig. 2.13. The NN tight-binding Hamiltonian can be written as

$$\begin{aligned} H &= t\sum_{m,n} a^{\dagger}_{m,n} b_{m,n} + a^{\dagger}_{m,n} b_{m,n+1} + a^{\dagger}_{m,n} b_{m+1,n} + h.c. \\ &= t\sum_{k_{\|}} \Big[\sum_{n} \big(1 + e^{ik_{\|}}\big) a^{\dagger}_{k_{\|},n} b_{k_{\|},n} + a^{\dagger}_{k_{\|},n} b_{k_{\|},n+1} + h.c. \Big] \,, \end{aligned} \tag{3.23}$$

where m and n index the unit cell according to Fig. 2.13. Thus, for any value of the momentum $k_{\|}$ there corresponds an effective one-dimensional system described by the term within the bracket in the above equation and that can be mapped onto the generalised Shockley model illustrated in Fig. 3.1. Based on this figure, it turns out that $t_1 = \left(1+e^{ik_\parallel}\right)t$ and $t_1' = t$ by identification and the effective system is described by the following Hamiltonian matrix

$$H(k_\parallel, k) = \sum_k \left(t_1(k_\parallel) + t_1' e^{ik}\right) a_k^\dagger b_k + h.c. \tag{3.24}$$

This Hamiltonian matrix still has the SLS but it explicitly breaks the TRS, since t_1 is now a complex number and $H(k_\parallel, k) \neq H(k_\parallel, -k)^*$. Therefore, the effective model belongs to the class AIII (see Table 3.1) and a winding number $W(k_\parallel)$ characterises its band-structure topology. In the first section, we have seen that this integer is given by the number of times the closed path outlined by $t_1(k_\parallel) + t_1' e^{ik}$ encloses the complex-plane origin, when k describes the whole one-dimensional BZ (here $-\pi < k < \pi$). Here it occurs if and only if $|t_1(k_\parallel| < |t_1'|$, which implies the existence of a zero-energy edge-state for values of $k_\parallel$ satisfying $-\pi < k_\parallel < -2\pi/3$ or $2\pi/3 < k_\parallel < \pi$. These edge states correspond to the flat bands in the band structure of a zigzag graphene nanoribbon that is shown in Fig. 3.7.

Such a dimensional reduction can be generalised to the description of boundary terminations more complicated than the zigzag one [34]. Any one-dimensional Hamiltonian matrix $H(k_\parallel, k)$ effectively describes a one-dimensional topological insulator which can be in a trivial phase or not. If this effective system belongs to a trivial phase (none edge state), its one-dimensional energy-gap must vanish and reopen when varying $k_\parallel$, in order to reach a non-trivial phase. Such a gap closing can only occur if the one-dimensional BZ referring to k crosses a nodal point in the graphene two-dimensional BZ. This is the reason why the flat energy bands corresponding to the graphene edge-states necessarily connect two Dirac cones (nodal points), as illustrated in Fig. 3.7.

3.3.2 Localised disorder

The topological features of the edge states in graphene relies on the translational invariance of the lattice. Here we consider a localised impurity in a zigzag graphene nanoribbon. First, we numerically check to what extent the edge states resist this kind of disorder. Fig. 3.8 depicts the density of states of a zigzag nanoribbon without and with a single on-site potential in the bulk. The potential magnitude is large ($V_0 = 10t$), which yields a resonance around the energy $E \sim -1/V_0$, as discussed in the previous chapter. This corresponds to the defect-state peak in the figure. The central peak refers to the zero-energy edge states and does not appear to be affected by the impurity.

Then, one can wonder what happens to the edge states when the impurity induces a res-

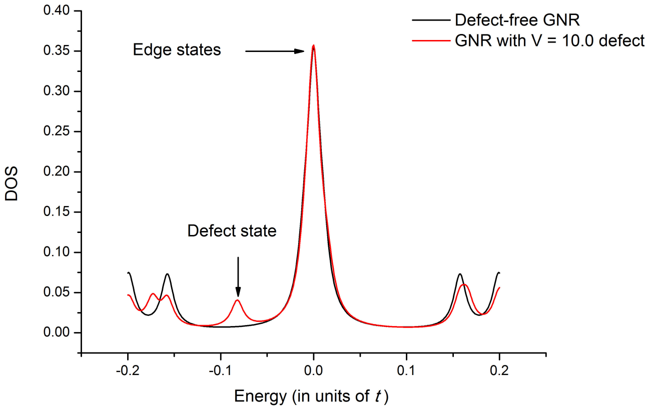

Fig. 3.8 Density of states of a zigzag graphene nanoribbon in the presence of an on-site defect.

onance at zero-energy. We have already encountered such resonators in the second chapter, and here again we consider the case of a vacancy, say localised on the sublattice A. We have shown that the missing atom necessarily induces an extra zero-energy state with non-null component only on the sublattice B. On top of that, the zigzag termination enables a strictly localised edge-state at $k_{\|} = \pi$, as it can be seen from the wavefunction definition (2.69). The wavefunction components of this state are depicted on the right part of the Fig. 3.9. As this state is strictly localised along the edge, it is expected to be the edge-state the most insensitive to the vacancy. Therefore we consider the limit case of a vacancy localised right underneath an edge atom, as illustrated by the black square in the figure. Because the missing atom A does not break the SLS, the zero-energy edge-states have non-null components only on the sublattice B. Thus they are insensitive to the vacancy and remain unchanged. The extra zero-energy state induced on the sublattice B by the missing atom can be charac-

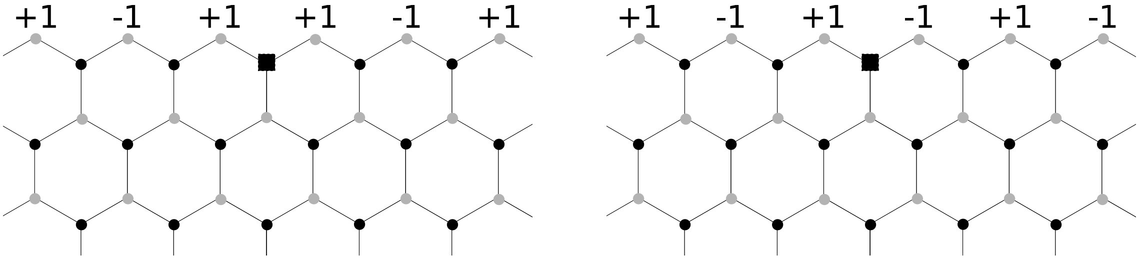

Fig. 3.9 The two edge states localised on the sublattice B when the vacancy is on the sublattice A (black square) and is localized strictly underneath an edge atom.

terised exactly in this case. Its wavefunction components are depicted in the left part of the Fig. 3.9 [23].

In this sense, the edge-states of a zigzag termination resist a localised disorder that breaks the translational invariance of the lattice.

3.4 Majorana fermions

3.4.1 Real solutions of the Dirac equation

In 1928, P. Dirac proposed a Lorentz invariant equation in order to describe relativistic spin-1/2 particles [96]. Although he entitled this work 'The Quantum Theory of the Electron', his equation also predicted the existence of antimatter. Indeed, for any particle satisfying the Dirac equation of motion, there exists a conjugated solution with the same mass but opposite charge: the antiparticle. The discovery of the positron by C.D. Anderson a few years latter was therefore a great success for Dirac's equation [97]. The covariant form of this relativistic equation is

$$\Big(i\gamma^{\mu}\partial_{\mu} - m\Big)\Psi = 0 \, , \tag{3.25}$$

where γ^{μ} denotes the 4×4 Dirac matrices, m the electron mass in the vacuum and $c = 1$. They fulfil the Clifford algebra

$$\{\gamma^{\mu}, \gamma^{\nu}\} = 2g^{\mu\nu} \tag{3.26}$$

where $g^{\mu\nu}$ is the Minkowski spacetime metric whose signature is $(-,+,+,+)$ and they are defined as

$$\gamma^{0} = \sigma^{0} \otimes \tau^{3} \, , \qquad \gamma^{\mu=1,2,3} = i\sigma^{\mu} \otimes \tau^{\mu} \, . \tag{3.27}$$

The Pauli matrices σ^{μ} and τ^{μ} respectively refer to the spin and charge sectors. If one is interested in real fermionic fields Ψ, one needs to make Eq. (3.25) be real too. This is the problem E. Majorana faced to [86], and he found out a basis where the Dirac matrices are purely imaginary

$$\begin{aligned} \tilde{\gamma}^{0} &= \ \sigma^{2} \otimes \tau^{1} \qquad & \tilde{\gamma}^{1} &= i\sigma^{1} \otimes \tau^{0} \\ \tilde{\gamma}^{2} &= i\sigma^{2} \otimes \tau^{1} \qquad & \tilde{\gamma}^{3} &= i\sigma^{3} \otimes \tau^{0}. \end{aligned} \tag{3.28}$$

In Majorana's representation, the Dirac equation is real, so that it can describe the evolution of real fermionic fields by simply imposing the reality condition

$$\tilde{\Psi} = \tilde{\Psi}^* . \tag{3.29}$$

Now, let us see how this reality condition turns out in another representation, such as the Dirac's one (3.27). There exists a unitary transformation U so that $\Psi = U\tilde{\Psi}$. After defining $C = UU^{\dagger *}$, which is a unitary operator too, the reality condition becomes

$$\Psi = C\Psi^* . \tag{3.30}$$

Moreover, this matrix satisfies

$$\begin{aligned} C^\dagger \gamma^\mu C &= U^*(U^\dagger \gamma^\mu U)U^{\dagger *} \\ &= (U\tilde{\gamma}^{\mu *}U^\dagger)^* \\ &= -\gamma^{\mu *} , \end{aligned} \tag{3.31}$$

so that the complex conjugation of Dirac equation (3.25) leads to

$$\begin{aligned} C\Big(-i\gamma^{\mu *}\partial_\mu - m\Big)\Psi^* &= 0 \\ \Big(i\gamma^\mu \partial_\mu - m\Big)C\Psi^* &= 0 . \end{aligned} \tag{3.32}$$

It means that $C\Psi^*$, which satisfies the same Dirac equation as Ψ, is its charge conjugate counterpart. This is the reason why Majorana fermions are defined as being their own antiparticle and are neutral objects. Fortunately, the Majorana fermion definition (3.30) is Lorentz invariant and holds in any inertial frame, thanks to the property (3.31) [98].

3.4.2 Condensed matter realisations

Majorana fermions in condensed matter physics were introduced in the context of vortices in two-dimensional $p_x + ip_y$ superconductors [99, 100]. Superconductivity, indeed, appears to be the natural playground for a condensed matter realisation of Majorana fermions, since it allows excitations that are BdG quasiparticles made of electrons (particles) and holes ('antiparticles'). Moreover the PHS is inherent to the mean-field description of superconductors, which requires every non-zero-energy state to have its own particle-hole conjugate partner with opposite energy and yields a redundancy. Therefore, the neutral Majorana fermions are linear combinations of an electron and a hole state with equal weights, which occurs only at zero-energy.

A. Kitaev subsequently proposed a one-dimensional tight-binding model that describes electrons in a finite chain in the presence of p-wave superconductivity [14]. Such a system is likely to host zero-energy Majorana modes localised at the ends of the chain. At a mean-field level, the Hamiltonian of the infinite system is

$$H = \sum_i \mu c_i^\dagger c_i + t\big(c_{i+1}^\dagger c_i + c_i^\dagger c_{i+1}\big) + \Delta\big(c_{i+1}^\dagger c_i^\dagger + c_i c_{i+1}\big) \ , \tag{3.33}$$

where μ is the chemical potential, t the nearest-neighbour hopping amplitude and Δ the superconducting gap, supposed to be real. This p-wave pairing couples electrons with the same spin on neighbouring sites. Then the Hamiltonian can be re-written as

$$H = \frac{1}{2}\sum_k \psi^\dagger(k) H(k) \psi(k) \ , \tag{3.34}$$

where $\psi^\dagger(k) = (c_k^\dagger, c_k)$ and the 2×2 Hamiltonian matrix is given by

$$H(k) = 2\Delta \sin k \ \sigma_2 + \big(\mu + 2t\cos k\big) \ \sigma_3 \ . \tag{3.35}$$

It leads to the following dispersion relation

$$E_\pm = \pm\sqrt{(\mu + 2t\cos k)^2 + (2\Delta \sin k)^2} \ . \tag{3.36}$$

It can be remarked already that any gap closing may occur at the momenta $k = 0$ and $k = \pi$ only. Remember that this is a necessary condition to enable the system to change topological phases. As explained in [101], this one dimensional spinless model belongs to the class BDI and therefore supports a $\mathbb{Z}$ topological characterisation. Indeed, when performing the rotation defined by the unitary operator $U = e^{i\frac{\pi}{4}\sigma_2}$, the above Hamiltonian matrix becomes

$$\begin{aligned} \tilde{H}(k) &= U^\dagger H(k) U \\ &= \big(\mu + 2t\cos k\big) \ \sigma_1 + 2\Delta \sin k \ \sigma_2 \ , \end{aligned} \tag{3.37}$$

whose topological characterisation is equivalent to the one of the generalised Shockley model discussed in Sec. 3.1. Based on the relation (3.6), the winding number that characterises the two-band model is

$$W = \frac{\operatorname{sgn}\Delta}{2}\left[\operatorname{sgn}(2t+\mu)+\operatorname{sgn}(2t-\mu)\right] , \tag{3.38}$$

where we have used the fact that $2\Delta \sin k$ vanishes at $k = 0$ and $k = \pi$. Thus there is one Majorana mode localised at each end of the finite chain if $2|t| > |\mu|$, and none at all if $2|t| < |\mu|$. This precisely corresponds to the criterion introduced in Kitaev's original work [14]. Discussions about multiple Majorana edge modes and larger winding numbers can be found in references [102, 103].

These fermions were also predicted in Sr_2RuO_4 [104] and in systems made of cold fermionic atoms [105], again in the context of spinless $p_x + ip_y$ superconductors. The quest for a possible realisation of Majorana fermions actually took a serious step when Fu and Kane proposed to mimic the spin-triplet superconductivity at the surface of a topological insulator, using proximity-induced s-wave superconductivity [106]. Then, it was realised that a two-dimensional semiconductor could replace the topological insulator when considering a spin-orbit coupling and a Zeeman splitting, in addition to the s-wave pairing [89, 107]. One-dimensional versions of these proposals were suggested soon after [88, 108]. Majorana modes are also expected in two-dimensional noncentrosymmetric s-wave superconductors [24, 90], as well as in s-wave superfluids of cold fermionic atoms [109].

3.5 Spin-singlet superconductivity and Majorana modes in a honeycomb lattice

More generally, topological spin-singlet superconductors are known to manifest Majorana boundary modes in the presence of Rashba spin-orbit interactions, when a Zeeman magnetic field breaks the time-reversal symmetry (TRS) [24, 88–90, 107, 108]. Such boundary modes are investigated here in the honeycomb lattice with s-wave or d-wave superconductivity. Their emergence is connected to topological properties of the Bloch band structure, which is characterised by a first Chern number (class D). In a similar manner as the case of the quantum spin Hall effect [110], these topological properties can also be reduced to the knowledge of energy-band parities defined at any of the time-reversal invariant momenta in the Brillouin zone. In the case of the honeycomb lattice, we show that the diatomic pattern is responsible for a non-vanishing Rashba spin-orbit coupling at such momenta. Therefore, and contrary to similar superconductors the literature focuses on [24, 88–90, 107, 108], the Majorana-mode emergence explicitly depends on the magnitude of the spin-orbit

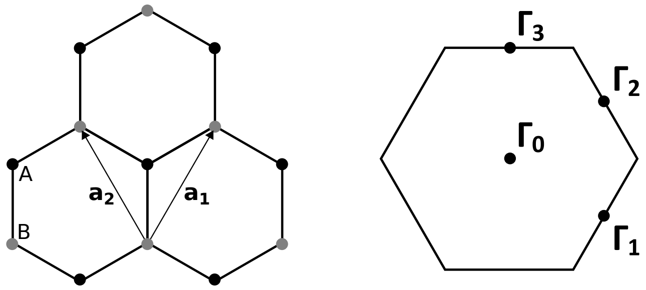

Fig. 3.10 The honeycomb lattice (left) and the hexagonal Brillouin zone (right) with its TRI momenta.

coupling. Although the band structure of the considered system relies on eight energy bands, symmetries enable us to characterise its topology and subsequently to give an analytical criterion that describes the emergence of Majorana modes. Importantly, such boundary modes cannot exist in the case of a zero doping, and their emergence is finally predicted at the edges of strained and doped nanoribbons.

3.5.1 Tight-binding Hamiltonians

Let us denote $\mathbf{a}_1$ and $\mathbf{a}_2$ the basis vectors that span the triangular Bravais lattice of the honeycomb lattice, as illustrated in Fig. 3.10. The electrons are described in a nearest-neighbour tight-binding approximation. In momentum space, the Hamiltonian for free particles is

$$\begin{aligned} H_0 = t \sum_{\mathbf{k},\sigma} f(\mathbf{k})\, a^\dagger_{\mathbf{k}\sigma} b_{\mathbf{k}\sigma} + h.c. \\ + \mu \sum_{\mathbf{k},\sigma} a^\dagger_{\mathbf{k}\sigma} a_{\mathbf{k}\sigma} + b^\dagger_{\mathbf{k}\sigma} b_{\mathbf{k}\sigma} \end{aligned} \tag{3.39}$$

where μ is the chemical potential and t the nearest-neighbour hopping amplitude. Moreover $f(\mathbf{k}) = \left(\alpha + e^{i\mathbf{k}.\mathbf{a}_1} + e^{i\mathbf{k}.\mathbf{a}_2}\right)$, while α refers to a tunable hopping amplitude, related to an eventual uniaxial strain. This parameter controls the existence of chiral massless Dirac fermions in the honeycomb lattice spectrum [43]. The fermionic operator $a_{\mathbf{k}\sigma}$ ($b_{\mathbf{k}\sigma}$) annihilates an electron with momentum $\mathbf{k}$ and spin σ in sublattice A (B).

As Majorana fermions are defined as being their own antiparticle, it is natural to introduce a superconducting pairing for a condensed matter realisation. Here we focus on spin-singlet superconductivity. It can be induced by proximity effect or originate from strong electron-electron interactions [111–113]. At a mean-field level, this is described by

$$\begin{aligned} H_S = & \Delta_0 \sum_{\mathbf{k}} (a^\dagger_{\mathbf{k}\uparrow} a^\dagger_{-\mathbf{k}\downarrow} + b^\dagger_{\mathbf{k}\uparrow} b^\dagger_{-\mathbf{k}\downarrow}) + h.c. \\ & + \Delta_1 \sum_{\mathbf{k}} f(\mathbf{k}) (a^\dagger_{\mathbf{k}\uparrow} b^\dagger_{-\mathbf{k}\downarrow} - a^\dagger_{\mathbf{k}\downarrow} b^\dagger_{-\mathbf{k}\uparrow}) + h.c. \end{aligned} \tag{3.40}$$

The real numbers Δ_0 and Δ_1 respectively denote on-site and nearest-neighbour electronic interactions. Attractive interactions correspond to negative values of these parameters, resulting in conventional and unconventional spin-singlet superconducting phases [111–113] respectively.

The time-reversal symmetry is broken by an applied magnetic field perpendicularly to the lattice. This yields a Zeeman potential V_z such that

$$H_Z = V_z \sum_{\mathbf{k},\sigma} \sigma (a^\dagger_{\mathbf{k}\sigma} a_{\mathbf{k}\sigma} + b^\dagger_{\mathbf{k}\sigma} b_{\mathbf{k}\sigma}) \, . \tag{3.41}$$

Finally, breaking the reflection symmetry relatively to the lattice plane, for example with ad-atoms [114], induces a Rashba spin-orbit coupling. It tends to align the spin in the direction defined by the nearest-neighbour vectors, which breaks the inversion symmetry between the two sublattices. The corresponding Hamiltonian in momentum space is given by

$$H_R = \lambda \sum_{\mathbf{k},\sigma,\sigma'} \begin{pmatrix} 0 & \mathscr{L}_+(\mathbf{k}) \\ \mathscr{L}_-(\mathbf{k}) & 0 \end{pmatrix}_{\sigma\sigma'} a^\dagger_{\mathbf{k}\sigma} b_{\mathbf{k}\sigma'} + h.c. \tag{3.42}$$

where λ characterises the coupling magnitude. The Rashba spin-orbit coupling does not break the time-reversal symmetry. This requires the functions $\mathscr{L}_\pm$ to satisfy $\mathscr{L}_\pm(\mathbf{k}) = -\mathscr{L}^*_\mp(-\mathbf{k})$ in momentum space.

As detailed in the next section, the topological order, which characterises the presence of Majorana modes, can be described from the TRI-momentum properties. In the case of a Bravais lattice with a monatomic pattern, there is the additional condition $\mathscr{L}^*_\pm(\mathbf{k}) = \mathscr{L}_\mp(\mathbf{k})$, coming from the Hamiltonian matrix that must be Hermitian. The spin-orbit coupling is then an odd function of the momentum and vanishes at any TRI momentum: $\mathscr{L}_\pm(\mathbf{\Gamma}_i) = 0$. Indeed, these specific momenta are defined by $\mathbf{\Gamma}_i = -\mathbf{\Gamma}_i + \mathbf{G}$, with $\mathbf{G}$ a vector of the reciprocal lattice. For this reason, the Rashba spin-orbit coupling does not appear in the Majorana-existence criterion [24, 88–90]. In that sense, the spin-dependent process essentially gaps the spectrum and protects the gapless boundary modes, in the same way as the intrinsic spin-orbit does in the quantum spin Hall phase [15, 85]. For the honeycomb lattice however, there are two non-equivalent atoms per unit cell. The spin-orbit coupling is a function of the momentum such as

$$\mathscr{L}_\pm(\mathbf{k}) = i\left[\alpha - 2\cos\left(\frac{\sqrt{3}}{2}k_x \pm \frac{\pi}{3}\right)e^{i\frac{3}{2}k_y}\right] . \tag{3.43}$$

Now, this process does not vanish at the TRI momenta, i.e. $\mathscr{L}_\pm(\mathbf{\Gamma}_i) \neq 0$ a priori. That is why one expects this process to explicitly affect the Majorana-existence condition. This is the essential difference from the previous studies in the literature that mainly concern monatomic-pattern lattices and noncentrosymmetric superconductors.

3.5.2 Energy-band parity definition

The Bogoliubov-de Gennes Hamiltonian of the total system, namely $H_0 + H_R + H_Z + H_S$, is

$$H = \frac{1}{2}\sum_{\mathbf{k}} \psi^\dagger(\mathbf{k})\mathscr{H}(\mathbf{k})\psi(\mathbf{k}) . \tag{3.44}$$

The fermionic fields are defined by

$$\psi^\dagger(\mathbf{k}) = \left(a^\dagger_{\mathbf{k}\uparrow}, b^\dagger_{\mathbf{k}\uparrow}, a^\dagger_{\mathbf{k}\downarrow}, b^\dagger_{\mathbf{k}\downarrow}, a_{-\mathbf{k}\uparrow}, b_{-\mathbf{k}\uparrow}, a_{-\mathbf{k}\downarrow}, b_{-\mathbf{k}\downarrow}\right), \tag{3.45}$$

whereas the Hamiltonian matrix is generically written under the form

$$\mathscr{H}(\mathbf{k}) = \begin{pmatrix} H(\mathbf{k}) & \Delta(\mathbf{k}) \\ -\Delta^*(-\mathbf{k}) & -H^*(-\mathbf{k}) \end{pmatrix}. \tag{3.46}$$

Here, Δ labels a 4×4 block. It results from the spin-singlet superconducting gaps introduced in (3.40) and verifies the condition $\Delta^*(-\mathbf{k}) = \Delta(\mathbf{k})$. Of course the Hamiltonian matrix satisfies the fundamental particle-hole symmetry (PHS)

$$\mathscr{C}^\dagger\mathscr{H}(\mathbf{k})\mathscr{C} = -\mathscr{H}^*(-\mathbf{k}). \tag{3.47}$$

The charge conjugation operator is defined by $\mathscr{C} = \sigma_0 \otimes s_0 \otimes \tau_1$, where σ, s and τ are Pauli matrices referring to the sublattice, spin and charge subspaces respectively. It squares to plus the identity operator and the system belongs to the Bogoliubov-de Gennes class D [77]. This symmetry relation results in the remarkable property that every non-zero energy state has its own pair. If $|\psi(\mathbf{k})\rangle$ in an eigenstate with energy $E(\mathbf{k})$, then the PHS requires

$\mathscr{C}|\psi^*(-\mathbf{k})\rangle$ to be eigenstate with energy $-E(-\mathbf{k})$.

Let us perform the following unitary transformation

$$\tilde{\mathscr{H}}(\mathbf{k}) = U^\dagger \mathscr{H}(\mathbf{k}) U \tag{3.48}$$

with

$$\begin{aligned} 2U =& \sigma_0 \otimes s_0 \otimes (\tau_0 + \tau_1) \\ &+ \sigma_1 \otimes s_3 \otimes (\tau_0 - \tau_1) \, . \end{aligned} \tag{3.49}$$

The Hamiltonian matrix still reads

$$\tilde{\mathscr{H}}(\mathbf{k}) = \begin{pmatrix} \tilde{H}(\mathbf{k}) & \tilde{\Delta}(\mathbf{k}) \\ -\tilde{\Delta}^*(-\mathbf{k}) & -\tilde{H}^*(-\mathbf{k}) \end{pmatrix} . \tag{3.50}$$

In the new basis, the Bogoliubov-de Gennes Hamiltonian matrix still respects the PHS, relatively to the same operator $\mathscr{C}$ since $[U, \mathscr{C}] = 0$. But now, the 4×4 blocks satisfy the two constraints $\tilde{H}(\mathbf{k}) = \tilde{H}(-\mathbf{k})$ and $\tilde{\Delta}(\mathbf{k}) = -\tilde{\Delta}(-\mathbf{k})$. The off-diagonal block $\tilde{\Delta}$ has acquired an odd momentum dependence under the unitary transformation. Therefore, the Hamiltonian matrix formally describes an odd-parity superconductor [115, 116]. Periodicity in momentum space also requires the blocks of the Hamiltonian matrix $\tilde{\mathscr{H}}(\mathbf{k})$ to satisfy more restrictive conditions

$$\begin{aligned} \tilde{H}(\mathbf{\Gamma}_i - \mathbf{k}) &= +\tilde{H}(\mathbf{\Gamma}_i + \mathbf{k}) \\ \tilde{\Delta}(\mathbf{\Gamma}_i - \mathbf{k}) &= -\tilde{\Delta}(\mathbf{\Gamma}_i + \mathbf{k}) \, . \end{aligned} \tag{3.51}$$

Hence, the off-diagonal blocks are also odd functions of $\mathbf{k}$ in the vicinity of any $\mathbf{\Gamma}_i$. They consequently vanish at every TRI momentum, where the Hamiltonian matrix $\tilde{\mathscr{H}}(\mathbf{k})$ becomes purely block-diagonal. This leads to the following commutation relation

$$[\mathscr{P}, \tilde{\mathscr{H}}(\mathbf{\Gamma}_i)] = 0, \tag{3.52}$$

where the operator $\mathscr{P} = \sigma_0 \otimes s_0 \otimes \tau_3$ plays the role of a parity operator. Since a common basis of eigenvectors does exist, if one of these vectors, say $|\psi(\mathbf{\Gamma}_i)\rangle$, is an eigenstate of the Hamiltonian matrix $\tilde{\mathscr{H}}(\mathbf{\Gamma}_i)$ with energy $E(\mathbf{\Gamma}_i)$, then it is also an eigenvector of the parity operator $\mathscr{P}$, with the eigenvalue $\pi(\mathbf{\Gamma}_i) = \pm 1$. This eigenvalue defines an energy-band parity

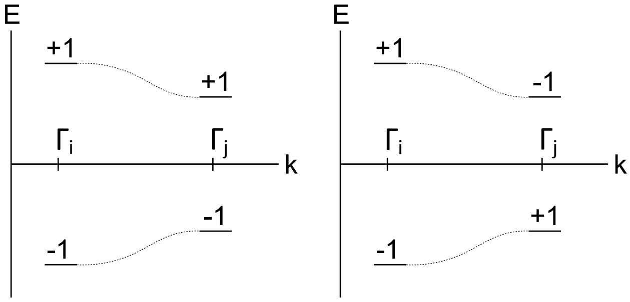

Fig. 3.11 Illustration of a band inversion that would occur at zero-energy. The lowest band and its particle-hole symmetric are depicted by dashed lines. The ±1 values define the energy-band parity at any TRI momenta, although only two of them are shown.

at any TRI momentum. Additionally, there is the anticommutation relation

$$\{\mathscr{P},\mathscr{C}\}=0\,, \tag{3.53}$$

so that $\mathscr{C}|\psi^*(\mathbf{\Gamma}_i)\rangle$ is eigenvector of the parity operator too, but with the eigenvalue $-\pi(\mathbf{\Gamma}_i)$.

For now, let us assume that, in the presence of spin-orbit coupling, the energy gap can only close at the TRI momenta. Then, together with the PHS, the band parity enable us to identify any gap closing that occurs at zero energy. This is illustrated in Fig.3.11. The parity eigenvalues are only mentioned for the lowest energy band and its particle-hole symmetric one, at two TRI momenta. From the figure, it is clear that any parity change for a given band requires a gap closing. More generally, any gap closing happening at zero energy is characterised by a sign change of the quantity

$$\delta_i=\prod_{E_n<0}\pi_n(\mathbf{\Gamma}_i)\,, \tag{3.54}$$

which is the parity product of all the negative-energy bands, with n the energy-band index. Besides, dealing with the parity at a given energy is equivalent to dealing with the energy sign at a given parity, except for a possible sign discrepancy

$$\delta_i=(-1)^{N/2}\prod_{\pi_n>0}\mathrm{sgn}E_n(\mathbf{\Gamma}_i)\,, \tag{3.55}$$

where N is the number of bands in the bulk spectrum. Note that the PHS ensures N to be even. In (3.55), the eigenvalue product for given positive parities is nothing but the determinant of the diagonal block $\tilde{H}(\mathbf{\Gamma}_i)$. As a result, (3.55) can be re-written as

$$\delta_i = (-1)^{N/2}\,\mathrm{sgn}[\mathrm{Det}\tilde{H}(\mathbf{\Gamma}_i)]\ . \tag{3.56}$$

3.5.3 Topological characterisation

Following the prescription introduced by L. Fu [110] and M. Sato [115], a connection is established between Eq. (3.56) and the first Chern number. Let us start with the the Berry connection

$$\begin{aligned}\mathbf{A}(\mathbf{k}) &= i\sum_n \langle\psi_n(\mathbf{k})|\nabla_{\mathbf{k}}|\psi_n(\mathbf{k})\rangle \\ &= \frac{i}{2}\mathrm{Tr}[M^\dagger(\mathbf{k})\nabla_{\mathbf{k}}M(\mathbf{k})] \\ &= \frac{i}{2}\nabla_{\mathbf{k}}\ln\mathrm{Det}M(\mathbf{k})\end{aligned} \tag{3.57}$$

with $M_{m,n} = \langle\psi_m(\mathbf{k})|\mathscr{P}\mathscr{C}|\psi_n^*(\mathbf{k})\rangle$, and $|\psi_m(\mathbf{k})\rangle$ a common eigenvector of the Hamiltonian matrix (3.50) and the parity operator. It can easily be checked that taking the eigenstates of (3.46) leaves that quantity unchanged, so that the Chern number remains exactly the same under the unitary transformation (3.48). The Berry connection also satisfies

$$\begin{aligned}\mathbf{A}^+(\mathbf{k}) &= i\sum_{E_n>0}\langle\psi_n(\mathbf{k})|\nabla_{\mathbf{k}}|\psi_n(\mathbf{k})\rangle \\ &= i\sum_{E_n>0}\langle\psi_n^*(\mathbf{k})|\mathscr{C}^\dagger\nabla_{\mathbf{k}}\mathscr{C}|\psi_n^*(\mathbf{k})\rangle \\ &= i\sum_{E_n<0}\langle\psi_n(-\mathbf{k})|\nabla_{\mathbf{k}}|\psi_n(-\mathbf{k})\rangle \\ &= \mathbf{A}^-(-\mathbf{k}).\end{aligned} \tag{3.58}$$

Besides, relation (3.57) requires the Berry curvature to vanish

$$\mathbf{F}(\mathbf{k}) = \nabla_{\mathbf{k}}\times\mathbf{A}(\mathbf{k}) = 0. \tag{3.59}$$

According to (3.58) also

$$\mathbf{F}^\pm(\mathbf{k}) = \mathbf{F}^\pm(-\mathbf{k}), \tag{3.60}$$

therefore the knowledge of this curvature over the full Brillouin zone can be reduced to a half Brillouin zone (BZ_+). Regarding the Chern number, it can be defined as the integral of the Berry curvature relative to the negative energy band

$$\begin{aligned}\nu &= \frac{1}{2\pi}\int_{BZ}\mathbf{F}^-(\mathbf{k}) \\ &= \frac{1}{\pi}\int_{BZ_+}\mathbf{F}^-(\mathbf{k}) \\ &= \frac{1}{\pi}\oint_{\partial BZ_+}\mathbf{A}^-(\mathbf{k}).\end{aligned} \tag{3.61}$$

Using relation (3.58), it follows that

$$\begin{aligned}\nu &= \frac{1}{\pi}\int_{\Gamma_0}^{\Gamma_1}\mathbf{A}(\mathbf{k}) + \frac{1}{\pi}\int_{\Gamma_2}^{\Gamma_3}\mathbf{A}(\mathbf{k}) \\ &= \frac{i}{\pi}\ln\sqrt{\frac{\mathrm{Det}M(\mathbf{\Gamma}_1)}{\mathrm{Det}M(\mathbf{\Gamma}_0)}\frac{\mathrm{Det}M(\mathbf{\Gamma}_3)}{\mathrm{Det}M(\mathbf{\Gamma}_2)}}.\end{aligned} \tag{3.62}$$

Since

$$\begin{aligned}M_{m,n}(\mathbf{\Gamma}_i) &= \langle\psi_m(\mathbf{\Gamma}_i)|\mathscr{P}\mathscr{C}|\psi_n^*(\mathbf{\Gamma}_i)\rangle \\ &= \pi_m(\mathbf{\Gamma}_i)\langle\psi_m(\mathbf{\Gamma}_i)|\mathscr{C}\psi_n^*(-\mathbf{\Gamma}_i)\rangle,\end{aligned} \tag{3.63}$$

it finally turns out

$$\begin{aligned}(-1)^\nu &= \sqrt{\prod_{m=1}^{N}\pi_m(\mathbf{\Gamma}_0)\pi_m(\mathbf{\Gamma}_1)\pi_m(\mathbf{\Gamma}_2)\pi_m(\mathbf{\Gamma}_3)} \\ &= \prod_{E_m<0}\pi_m(\mathbf{\Gamma}_0)\pi_m(\mathbf{\Gamma}_1)\pi_m(\mathbf{\Gamma}_2)\pi_m(\mathbf{\Gamma}_3) \\ &= \prod_{i=0}^{3}\delta_i.\end{aligned} \tag{3.64}$$

This relation connects the Chern number to the product of the negative-energy band parities at the TRI momenta. For a trivial phase, i.e. a null Chern number, the product (3.64) takes the positive value $+1$. The negative value -1 can only be met for odd Chern numbers. It is important to note that this relation only refers to the parity of the Chern number, which does not allow us to discriminate the topological phase characterised by $\nu = 2$ (for example) from the trivial phase $\nu = 0$. Nevertheless, it seems that if the parity change occurs at a single

TRI momentum only (and cannot simultaneously occur at distinct TRI momenta), then the Chern number appears to be restricted to values 0 and ±1, as it can be checked from the phase diagrams in Fig. 3.13, Fig. 3.14 and Fig. 3.15. In this case, the relation in Eq. (3.64) appears to be sufficient to distinguish the trivial and topological phases.

The topological criterion is given by the parameter values that define the border between two distinct topological phases. As previously mentioned, going from one topological phase to another requires the parity product (3.54) to change signs. It also involves a gap closing at zero-energy. Indeed, when the gap closes, the two particle-hole symmetric eigenstates cannot be distinguished from each other, and so it is about their parity. The Chern number becomes ill-defined and it can then take another integer value. Then the gap closing occurs at the TRI momenta when $\mathrm{Det}\tilde{H}(\mathbf{\Gamma}_i) = 0$. This determinant can be expressed in terms of the model parameters as well and

$$\mathrm{Det}H(\mathbf{\Gamma}_i) = V_z^4 - 2bV_z^2 + b^2 - 4t^2 f^2 \mu^2 d \; , \tag{3.65}$$

where

$$b = \Delta_0^2 + (\Delta_1^2 + t^2) f^2 + \mu^2 - \lambda^2 L^2 \tag{3.66}$$

and

$$d = 1 - \Big(1 + \frac{\Delta_0^2}{t^2 f^2}\Big)\frac{\lambda^2 L^2}{\mu^2} + \Big(2 + \frac{\Delta_0\Delta_1}{t\mu}\Big)\frac{\Delta_0\Delta_1}{t\mu} \; . \tag{3.67}$$

$\mathbf{\Gamma}_i$ has been omitted in the expression of functions f and $L = |\mathscr{L}_+^* - \mathscr{L}_-|/2$. Note that $L(\mathbf{\Gamma}_i) = |\mathscr{L}_+(\mathbf{\Gamma}_i)|$. The gap closing condition at the TRI momenta is given by the roots of Eq. (3.65), namely

$$V_z^2 = \Delta_0^2 + (\Delta_1^2 + t^2) f^2 + \mu^2 - \lambda^2 L^2 \pm 2 f \mu t \sqrt{d} \; , \tag{3.68}$$

provided that $d \geq 0$, which means

$$\mu^2 \geq \mu_c^2 = \Big(1 + \frac{\Delta_0^2}{t^2 f^2}\Big)\lambda^2 L^2 \tag{3.69}$$

if one consider only s-wave superconductivity ($\Delta_1 = 0$), or

$$\mu^2 \geq \mu_c^2 = \lambda^2 L^2 \tag{3.70}$$

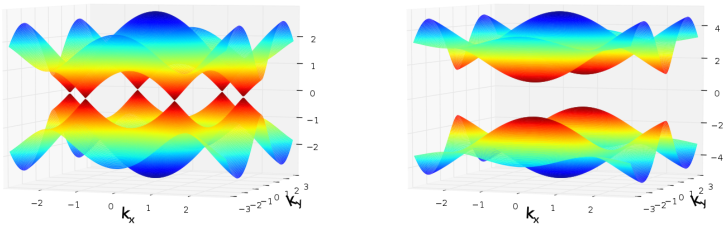

Fig. 3.12 Honeycomb lattice spectra in a nearest-neighbour approximation for $\alpha = 1$ (left) and $\alpha = 3$ (right).

if only d-wave superconductivity is considered ($\Delta_0 = 0$). The first consequence of the diatomic pattern, which implies $L(\boldsymbol{\Gamma}_i) \neq 0$, is that a non-zero doping is mandatory to make a band inversion occur at a time-reversal invariant momentum. Second, the diatomic pattern, via the magnitude of the Rashba spin-orbit coupling, also constraints the gap closing condition (3.68), which is not the case in the previous studies in the literature, as previously mentioned. Nevertheless, we are about to show that the formation of Majorana boundary modes remains possible in the honeycomb lattice, even though constrained its diatomic pattern.

3.5.4 Applications

According to relation (3.64), the emergence of Majorana modes depends on the parity-product sign defined at each TRI momentum. This section illustrates this connection through concrete examples. For simplicity, we consider $\Delta_1 = 0$, and we discuss cases where a parity change only occurs at a single TRI momentum, namely either $\boldsymbol{\Gamma}_0$ or $\boldsymbol{\Gamma}_3$. We consider three cases.

Top of the band structure

First, the system is highly doped in order to focus on the quadratic part of the free-electron spectrum, which means $\mu \sim f(\boldsymbol{\Gamma}_0)t$. It corresponds to the blue regions at the top (or bottom) of the band structure in Fig. 3.12. For simplicity we consider

$$\mu = f(\boldsymbol{\Gamma}_0)t = (\alpha + 2)t \; . \tag{3.71}$$

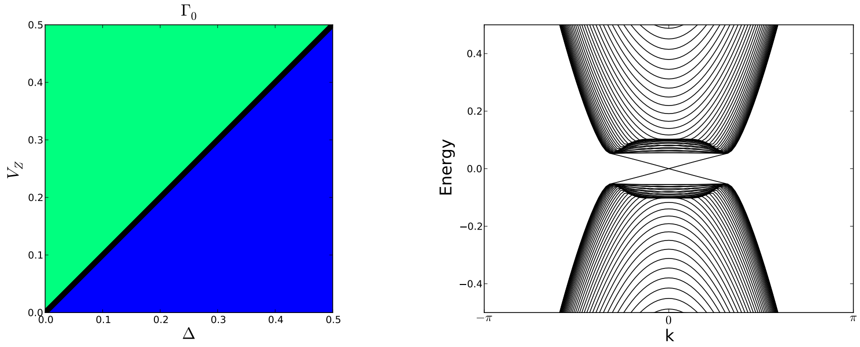

Fig. 3.13 Parity product δ_0 (left) and zigzag-nanoribbon band structure (right): $\alpha = 1$, $\mu = f(\boldsymbol{\Gamma}_0) = 3t$ and $\lambda = 0.1t$ for both pictures, whereas $V_z = 0.3t$ and $\Delta = 0.2t$ in the right plot. The blue (green) color corresponds to $\delta_0 = +1$ (-1), while the black line in between is given by the gap closing condition (3.68). The parameters are expressed in units of t.

Assuming that $\lambda^2 \ll \mu^2$, then $d > 0$ is always satisfied. The gap closing condition (3.68) becomes

$$\begin{aligned} V_z^2 = & \Big[f(\boldsymbol{\Gamma}_i) - f(\boldsymbol{\Gamma}_0)\Big]\Big[f(\boldsymbol{\Gamma}_i) - f(\boldsymbol{\Gamma}_0) + \frac{L^2(\boldsymbol{\Gamma}_i)}{f(\boldsymbol{\Gamma}_0)}\frac{\lambda^2}{t^2}\Big]\, t^2 \\ & + \Big[1 + \frac{L^2(\boldsymbol{\Gamma}_i)}{f(\boldsymbol{\Gamma}_0) f(\boldsymbol{\Gamma}_i)}\frac{\lambda^2}{t^2}\Big]\, \Delta_0^2 \end{aligned} \tag{3.72}$$

in a first order approximation, at any TRI momentum $\boldsymbol{\Gamma}_{i=0,1,2,3}$. Moreover,

$$f(\boldsymbol{\Gamma}_{i=1,2}) = \alpha\ , \quad f(\boldsymbol{\Gamma}_3) = (\alpha - 2)\ , \tag{3.73}$$

so that $|f(\boldsymbol{\Gamma}_{i=1,2,3}) - f(\boldsymbol{\Gamma}_0)| \sim 1$. It is clear that no gap closing can occur at such momenta for values of the Zeeman fields like $V_z \leq 0.5t$. Thus the parity product is only likely to change signs at $\boldsymbol{\Gamma}_0$. The topological phase corresponds to

$$V_z > \Big[1 + \frac{L^2(\boldsymbol{\Gamma}_0)}{f^2(\boldsymbol{\Gamma}_0)}\frac{\lambda^2}{t^2}\Big]\Delta_0\ . \tag{3.74}$$

This is illustrated by the phase diagram in Fig. 3.13. Note that $L(\boldsymbol{\Gamma}_0) = 0$ would lead to the usual criterion $V_z > \Delta_0$ which is obtained in the case of a monatomic pattern [25].

Van-Hove Singularities

Second, Majorana modes can also emerge due to a parity change that occurs at a non-zero TRI momenta, like $\boldsymbol{\Gamma}_3$. We consider a strain such that $1 < \alpha < 2$. In that case $|f(\boldsymbol{\Gamma}_{i=1,2})| \neq$

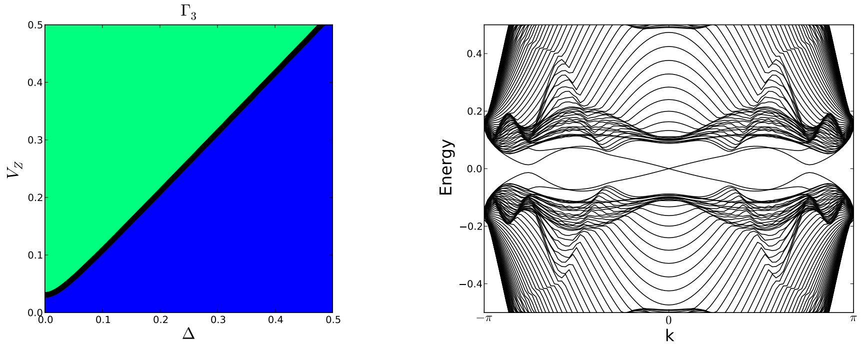

Fig. 3.14 Parity product δ_3 (left) and zigzag nanoribbon band structure (right): $\alpha = 1.2$, $\mu = f(\mathbf{\Gamma}_3) = 0.8t$ and $\lambda = 0.1t$ for both pictures, whereas $V_z = 0.3t$ and $\Delta = 0.2t$ in the right plot. The blue (green) color corresponds to $\delta_0 = +1$ (-1), while the black line in between is given by the gap closing condition (3.68). The parameters are expressed in units of t.

$|f(\mathbf{\Gamma}_3)|$ according to the definitions in Eq. (3.73), such that a parity change can occur at $\mathbf{\Gamma}_3$ only.

We focus on a system which is strained and sufficiently doped to approach the Van-Hove singularity that arises at $\mathbf{\Gamma}_3$. It is related to a saddle point around which the free-electron spectrum is hyperbolic. This is described by the yellow regions in Fig. 3.12. This singularity is related to a divergence in the electronic density of states. Note that the electronic density strongly increases such that a d-wave pairing may also appear ($\Delta_1 \neq 0$) and dominate over the s-wave pairing, without compromising the Majorana mode existence [113]. As already mentioned however, we consider here $\Delta_1 = 0$.

From (3.73), it is clear that stretching the lattice, i.e. increasing α, reduces the van Hove singularity energy given by $|f(\mathbf{\Gamma}_3)t|$. This enable us to decrease the doping down to about one-tenth of the bandwidth. Note that such a doping becomes relevant in a graphene layer [117] that can be strained up to twenty percent [118]. When considering $\mu = f(\mathbf{\Gamma}_3)$ the topological criterion reads

$$V_z > \left[1 + \frac{L^2(\mathbf{\Gamma}_3)}{f^2(\mathbf{\Gamma}_3)} \frac{\lambda^2}{t^2}\right] \Delta_0 \,, \tag{3.75}$$

as long as $\lambda^2 \ll \mu^2$. A phase diagram is presented in Fig. 3.14 for a strained honeycomb lattice, $\alpha = 1.2t$. The spin-orbit coupling $\lambda = 0.1t$ yields a clear gapped band structure, but considering a smaller coupling would not compromise the Majorana modes existence.

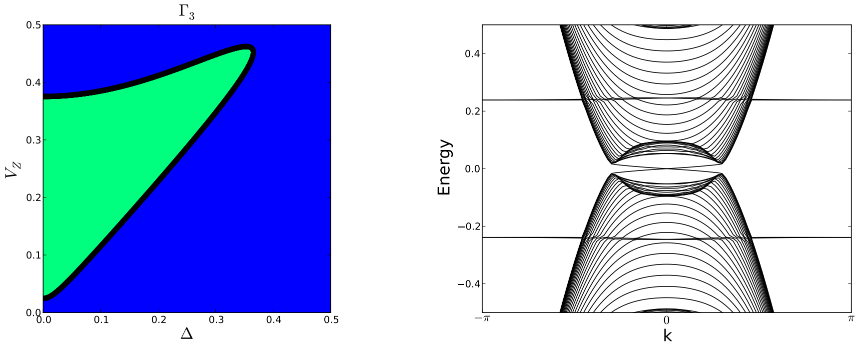

Fig. 3.15 Parity product δ_3 (left) and zigzag nanoribbon band structure (right): $\alpha = 2.2$, $\mu = f(\mathbf{\Gamma}_3) = 0.2t$ and $\lambda = 0.03t$ for both pictures, whereas $V_z = 0.3t$ and $\Delta = 0.2t$ in the right plot. The blue (green) color corresponds to $\delta_0 = +1$ (-1), while the black line in between is given by the gap closing condition (3.68). The parameters are expressed in units of t.

Dirac Cone Merging

Finally, Majorana modes may also appear after a parity product changes signs at $\mathbf{\Gamma}_3$, when the spectrum is quadratic in its vicinity. Such a situation is reached when increasing the strain magnitude beyond a critical value $\alpha = 2$. At this point, the two-nonequivalent Dirac cones (red regions in Fig. 3.12) merge, which defines a Lifshitz transition [16, 43]. Beyond this transition, the spectrum become gapped and quadratic around $\mathbf{\Gamma}_3$.

Let us consider a system that is sufficiently strained ($\alpha \gtrsim 2$) and weakly doped so that we focus on the quadratic part of the spectrum around $\mathbf{\Gamma}_3$ (red regions in Fig. 3.12). Contrary to the two previous cases, the doping and the spin-orbit coupling are of comparable orders of magnitude. Any expansion like (3.72) does not hold in that case and the condition $d \geq 0$ is not necessarily met. This leads to a critical value for the superconducting gap. Majorana modes can exist only when

$$\Delta^2 < \Delta_c^2 = \left(\frac{\mu^2}{\lambda^2 L^2(\mathbf{\Gamma}_3)} - 1\right) f^2(\mathbf{\Gamma}_3) t^2 \,, \tag{3.76}$$

which requires a doping such that $\mu > \lambda L(\mathbf{\Gamma}_3)$. It turns out that the Rashba spin-orbit coupling drastically affects the existence of the topological phase , leading to a phase diagram similar to the one in Fig. 3.15. Note that the zigzag-boundary termination is responsible for the flat bands that appear in the band structure. They were not visible in the two previous cases, because the energies considered were too high.

Although this third scenario is not achievable in graphene, it should find a possible reasilation in s-wave superfluids of cold fermionic atoms [109].

Part II

Spintronic in Mesoscopic Superconductors

Chapter 4

Frequency-dependent spin accumulation in out-of-equilibrium superconductors

4.1 Introduction

Chargeless spin accumulation has recently been realised experimentally [26, 119, 120], enabling an estimate of the spin-relaxation time in mesoscopic superconductors. This is remarkably long, of the order of nanoseconds, significantly longer than the charge-relaxation time [121–126]. The measurement of this spin relaxation time using the injection of spin from a ferromagnet (FM) into a superconductor (SC) has recently been presented [26] yielding an estimation of the order of $10ns$ [127]. The SC was subject to a Zeeman magnetic field which splits its density of states (DOS) for the up and down quasiparticles [128, 129]. To test that this spin relaxation time value is accurate a new experiment has been developed in which a normal-superconducting junction is subject to both a constant (DC) and a time dependent (AC) bias. The ferromagnetic lead is replaced by a normal one, as in [26] it was shown that spin accumulation was mostly due to the Zeeman split rather than to the ferromagnetic character of the lead. In the new experiments the SC is much cleaner, with a DOS much closer to the BCS form [27]. The time-averaged spin chemical potential difference resulting from the spin accumulation is measured as a function of the applied chemical potential, the intensity of the AC signal, and as a function of the frequency.

Here we present the model which allows us to fit the experimental data in [27] (a pdf version of this reference is provided at the end of the chapter), extract the value of the spin-relaxation time, and explain the experimental dependence of the accumulated spin with respect to various parameters. The injection between the SC and the FM/metallic lead is simulated using the Fermi's golden rule (FGR) and taking into account all possible tunneling processes when an electron from the lead is injected into the SC (the electron can enter the SC as a quasiparticle with the same spin, or as a quasihole of opposite spin) [130, 131]. Our model generalises the theory presented in [26] which was an incomplete approximation, as some of the tunneling processes have not been taken into account, and which was valid only for small values of the spin imbalance. We subsequently write down and solve self-consistently the time-dependent semi-classical equations of motion for the spin accumulation in the SC. The relation between the spin accumulation in the SC and what is seen in a non-local measurement of this accumulation performed using a FM lead is obtained by imposing the condition that the electric current through the non-local probe is zero [27]. The bias voltage to which the probe is subjected to satisfy this condition is the measured non-local voltage that we can relate theoretically with the applied voltage.

A crucial observation to be made is that a frequency dependence for the time-averaged non-local measured voltage is conditioned by the existence of non-linearities in the system (such as the non-linearity of the conductance of the detection junction, and the non-linear dependence of the spin accumulation in the SC on the difference of chemical potentials between the spin up and down quasiparticles). Such non-linearities are automatic in a SC for not too small values of the spin accumulation due to the strong non-linear form of the BCS DOS. For a fully linear system the measured spin accumulation is independent of frequency, and the spin-relaxation time cannot be obtained from frequency-domain measurements.

First we remind the reader of the theory of spin injection into a SC, as well as the relation between the injection electric and spin current as a function of the applied voltage. Then the experimental setup is presented, and we introduce the semi-classical equations of motion that rules the time-evolution of the spin. Finally we solve these equations for a DC bias, before studying sinusoidal and rectangular AC biases.

4.2 FM-SC junction

In this section we introduce the model to describe the FM-SC junction and we compute the tunneling currents flowing through it.

4.2.1 Theoretical model

The total Hamiltonian for the junction is : $\mathrm{H} = \mathrm{H}_F + \mathrm{H}_S + \mathrm{H}_T$. The Hamiltonian for the FM lead is

$$\mathrm{H}_F = \sum_{q,\sigma} (\varepsilon_q + \mu_F) c^\dagger_{q,\sigma} c_{q,\sigma}, \tag{4.1}$$

with $\varepsilon_q = \hbar^2 q^2/2m$ and μ_F the chemical potential in the FM. Actually, the "ferromagnetic" character of the lead will be encoded in the spin-dependent tunnel amplitude . The BCS Hamiltonian H_S is given by

$$\mathrm{H}_S = \sum_{p,\sigma} (\varepsilon_p + \mu_s - \sigma\mu_B H) c^\dagger_{p,\sigma} c_{p,\sigma} - \sum_p \left(\Delta c^\dagger_{p,\uparrow} c^\dagger_{-p,\downarrow} + h.c.\right), \tag{4.2}$$

with $\varepsilon_p = \hbar^2 p^2/2m$, Δ is the superconducting energy gap and $\mu_B H$ is the Zeeman energy. The tunneling Hamiltonian is

$$\mathrm{H}_T = \sum_{p,q,\sigma} \left(T^\sigma_{p,q} c^\dagger_{p,\sigma} c_{q,\sigma} + h.c.\right). \tag{4.3}$$

The first term of H_T describes the transfer of electrons with spin σ and momentum q into the superconductor with a spin dependent amplitude $T^\sigma_{p,q}$. We assume that there is no spin flip at the interface but that the momentum is not conserved, $p \nrightarrow q$. It is more convenient to express the operators for electrons in the SC in terms of quasiparticle operators using the Josephson's definition of the Bogoliubov-Valatin transformation [132, 133]

$$c^\dagger_{p,\uparrow} = u_p \gamma^\dagger_{e,p\uparrow} + v_p \gamma_{h,p\downarrow}, \tag{4.4}$$

$$c^\dagger_{-p,\downarrow} = u_p \gamma^\dagger_{e,p\downarrow} - v_p \gamma_{h,p\uparrow}, \tag{4.5}$$

where the $\gamma^\dagger_{e(h),p}$ are creation operators of electronlike (holelike) excitations. Since a quasiparticle has probability u_p^2 to be an electron and probability v_k^2 to be a hole, the quasiparticle charge is given by $q_p = u_p^2 - v_p^2$. The corresponding charge carried by the condensate is $2v_p^2 = 1 - q_p$ [130]. With the proper choice of the coherence factors u_p and v_p, the BCS Hamiltonian can be written as

$$\mathrm{H}_S = \mu_s \sum_{p,\sigma} c^\dagger_{p,\sigma} c_{p,\sigma} + \sum_{p,\sigma} E_{p,\sigma} \left(\gamma^\dagger_{e,p\sigma} \gamma_{e,p\sigma} + \gamma^\dagger_{h,p\sigma} \gamma_{h,p\sigma}\right), \tag{4.6}$$

where

$$u_p = \frac{1}{2}\Big(1 + \frac{\varepsilon_p}{\sqrt{\varepsilon_p^2 + \Delta^2}}\Big),$$
$$v_p = \frac{1}{2}\Big(1 - \frac{\varepsilon_p}{\sqrt{\varepsilon_p^2 + \Delta^2}}\Big),$$

and $E_{p,\sigma} = \sqrt{\varepsilon_p^2 + \Delta^2} - \sigma\mu_B H$ the excitation energy [128, 129]. Introducing $\bar{\sigma} = -\sigma$, the tunneling Hamiltonian becomes

$$\mathrm{H}_T = \sum_{p,q,\sigma} \Big(T^{\sigma}_{p,q} \big[u_p \gamma^{\dagger}_{e,p\sigma} c_{q,\sigma} + v_p \gamma^{\dagger}_{h,p\bar{\sigma}} c_{q,\sigma} \big] + h.c. \Big). \tag{4.7}$$

4.2.2 Tunnel current

We now calculate the particle tunneling current flowing through the junction by using Fermi's Golden rule[130, 134]. The allowed tunneling processes and the corresponding probabilities are described in Table 4.1. For example, for a $\gamma^{\dagger}_{e,p\sigma} c_{q,\sigma}$ process (an electron $c_{q,\sigma}$ is annihilated in the FM to create a quasiparticle $\gamma^{\dagger}_{e,p\sigma}$ in the SC), the total probability is a product of the tunnel probability given by the tunnel Hamiltonian, $|T^{\sigma}_{p,q}|^2 u_p^2$, the probability to have a filled state in the FM to tunnel from, $f(\varepsilon_q)$, and the probability to have an empty state in the SC to tunnel into, $1 - f_{p\sigma}(E_{p,\sigma})$.

The tunneling average current through the junction for a given spin can be written as

$$\begin{aligned} I_\sigma = \frac{2\pi}{\hbar} \sum_{p,q} |T^{\sigma}_{p,q}|^2 \Big\{ & u_p^2 \delta(\varepsilon_q - E_{p,\sigma} + eV) \big[f(\varepsilon_q) - f_{p\sigma}(E_{p,\sigma}) \big] \\ & - v_p^2 \delta(\varepsilon_q + E_{p,\bar{\sigma}} + eV) \big[1 - f(\varepsilon_q) - f_{p\bar{\sigma}}(E_{p,\bar{\sigma}}) \big] \Big\}, \end{aligned} \tag{4.8}$$

Process	Probability	Charge	Quasiparticle charge	Condensate charge	Spin
$\gamma^{\dagger}_{e,p\sigma} c_{q,\sigma}$	$u_p^2[1 - f_{p\sigma}(E_{p,\sigma})] f(\varepsilon_q)$	$+1$	$+q_p$	$1 - q_p$	σ
$c^{\dagger}_{q,\sigma} \gamma_{e,p\sigma}$	$u_p^2[1 - f(\varepsilon_q)] f_{p\sigma}(E_{p,\sigma})$	-1	$-q_p$	$-1 + q_p$	$\bar{\sigma}$
$\gamma_{h,p\bar{\sigma}} c_{q,\sigma}$	$v_p^2 f_{p\bar{\sigma}}(E_{p,\bar{\sigma}}) f(\varepsilon_q)$	$+1$	$-q_p$	$1 + q_p$	σ
$c^{\dagger}_{q,\sigma} \gamma^{\dagger}_{h,p\bar{\sigma}}$	$v_p^2[1 - f_{p\bar{\sigma}}(E_{p,\bar{\sigma}})][1 - f(\varepsilon_q)]$	-1	$+q_p$	$-1 - q_p$	$\bar{\sigma}$

Table 4.1 Tunneling processes in excitation representation [130, 131].

where we assumed $T^{\sigma}_{p,q} = T^{\sigma}_{q,p}$. To simplify this formula we note that for each state with $p^+ > k_F$, energy $E_{p^+,\sigma}$ and u_{p^+}, there exists another state $p^- < k_F$ with the same energy $E_{p^-,\sigma} = E_{p^+,\sigma}$ (note however that $\varepsilon_{p^+} = -\varepsilon_{p^-}$). This implies for the coherence factors that $u^2_{p^\pm} = v^2_{p^\mp}$. Moreover we can reasonably assume that $|T_{p^+,q}| = |T_{p^-,q}|$. By separating the sum over p into two sums over $p^\pm$, and by noting that only the coherence factors depend on $p^\pm$ (with $u_{p^\pm} = v_{p^\mp}$, $u^2_{p^\pm} + v^2_{p^\pm} = 1$) we obtain

$$\begin{aligned} I_\sigma = \frac{2\pi}{\hbar} \sum_{p^+,q} |T^{\sigma}_{p^+,q}|^2 \Big\{ & \delta(\varepsilon_q - E_{p^+,\sigma} + eV)\left[f(\varepsilon_q) - f_{p^+\sigma}(E_{p^+,\sigma})\right] \\ & - \delta(\varepsilon_q + E_{p^+,\bar{\sigma}} + eV)\left[1 - f(\varepsilon_q) - f_{p^+\bar{\sigma}}(E_{p^+,\bar{\sigma}})\right] \Big\}, \end{aligned} \tag{4.9}$$

where we assumed that there is no charge accumulation, meaning that the Fermi-Dirac distribution in the superconductor is identical for momenta greater and lesser than the Fermi momentum k_F. In the following the sign $+$ of the momentum p will be omitted for brevity. We can now convert the momentum summation into an energy integral, using

$$\sum_q \to \int dq \underbrace{\rho(q)}_{(L/2\pi)^d} \to \int dE \rho(E). \tag{4.10}$$

For the energy range we consider, it is reasonable to assume that the FM DOS and the tunneling probabilities are roughly independent of energy. Performing the momentum-energy conversion for the $\sum_q$ in the FM, and subsequently the resulting energy integral, we obtain

$$I_\sigma = \frac{2\pi}{\hbar} \sum_p \rho_F |T^\sigma|^2 \Big\{ f(E_{p,\sigma} - eV) - f_{p\sigma}(E_{p,\sigma}) + f_{p\bar{\sigma}}(E_{p,\bar{\sigma}}) - f(E_{p,\bar{\sigma}} + eV) \Big\}. \tag{4.11}$$

Here ρ_F is the total density of states of the ferromagnetic lead (integrated over the volume of the FM). The conversion of the summation over the momentum p in the SC into an energy integral is more tricky. This is because the two first terms of the above expression correspond to the injection of an electron as an electron-like excitation of energy $E_{p,\sigma}$. The last two terms correspond to the conversion of an electron into a hole-like excitation at energy $-E_{p,\bar{\sigma}}$. The SC densities of states are different for the two processes, due to the presence of the Zeeman field: $\rho_S(E_{p,\sigma}) \neq \rho_S(-E_{p,\bar{\sigma}})$. Converting the momentum summation over p into an energy integral thus leads to

$$\begin{aligned}I_\sigma = \frac{2\pi}{\hbar}\rho_F\rho_0|T^\sigma|^2\int_{-\infty}^{+\infty} dE\Big\{&\rho(E_\sigma)\left[f(E_\sigma - eV) - f_\sigma(E_\sigma)\right]\\ &+\rho(E_{\bar\sigma})\left[f_{\bar\sigma}(E_{\bar\sigma}) - f(E_{\bar\sigma} + eV)\right]\Big\},\end{aligned} \tag{4.12}$$

where $E_\sigma = E - \sigma\mu_B H$, ρ_0 is the DOS of the superconductor at the Fermi energy, and

$$\rho(E) = \theta(E - \Delta)\frac{E}{\sqrt{E^2 - \Delta^2}}, \tag{4.13}$$

is the usual normalised BCS density of states, with θ the Heaviside step function. In real materials this DOS needs to be modified to round-off singularities and to take into account the existence of states inside the gap [135]. Such states can be induced for instance by disorder (static impurities, magnetic impurities, etc.). Several theoretical models which describe the presence of such gap states can be used in order to fit properly the experimentally measured DOS. The most commonly used is the Dynes model for the DOS [136], in which a phenomenological parameter δ is added to the energy as an imaginary part corresponding to a quasiparticle lifetime

$$\rho_D(E) = \left|\mathrm{Re}\left[\frac{E + i\delta}{\sqrt{(E + i\delta)^2 - \Delta^2}}\right]\right|. \tag{4.14}$$

We can also use the Fulde DOS which also takes into account the presence of spin orbit effects, disorder, etc., in conjunction with an applied magnetic field [137]. It is however very difficult to properly fit the experimentally measured DOS using this models. Sometimes is most useful to use in the numerical calculations directly the DOS measured experimentally. The total spin and electric tunneling current can be written as $I_e = e\sum_\sigma I_\sigma$ and $I_s = \hbar/2\sum_\sigma \sigma I_\sigma$ where

$$\begin{aligned}I_\sigma = \frac{\pi}{\hbar}\rho_F\rho_0|T^\sigma|^2\int_{-\infty}^{+\infty} dE\Big\{&\rho(E_\sigma)\left[f(E - eV) - f(E - \sigma\mu_s)\right]\\ &+\rho(E_{\bar\sigma})\left[f(E + \sigma\mu_s) - f(E + eV)\right]\Big\}.\end{aligned} \tag{4.15}$$

Here μ_s refers to the shift of the chemical potential due to the spin imbalance.

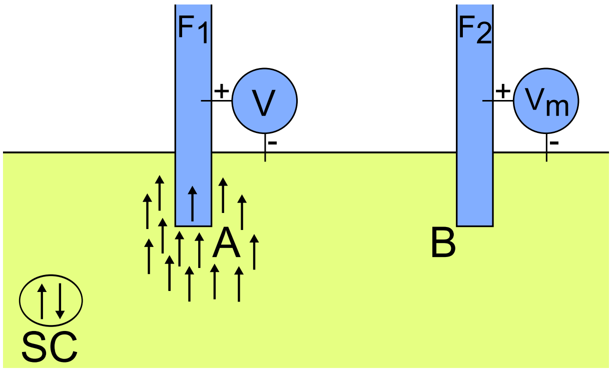

Fig. 4.1 Illustration of the experimental setup.

4.3 Spin accumulation in a SC-FM junction

4.3.1 Experimental setup

The setup that we consider is presented in Fig. 4.1. A voltage bias V is applied between a lead and the SC at point A (injection junction). The spin accumulation $S(t)$ in the SC is measured at point B (detection junction) by applying a voltage difference V_m between a ferromagnetic lead and the SC and imposing the condition that the electrical current flowing through the detection junction is zero.

4.3.2 Semiclassical equations of motion

We assume that the time dependent spin accumulation $S(t)$ in the superconductor satisfies a simple equation of motion

$$\frac{dS(t)}{dt} = I_s^i(t) - \frac{S(t)}{\tau_s}, \tag{4.16}$$

where τ_s is the spin relaxation time in the SC. As described in the previous section, I_s^i, the spin current in the injection junction, is a function of the applied voltage V between the SC and the injection lead. In much of our analysis, as well as in the experiments presented in Ref. [27] the injection lead is considered to be non-FM (i.e. $T_\downarrow^i = T_\uparrow^i = T^i$) and the injected spin current can be written as

$$\begin{aligned} I_s^i =& \hbar/2\sum_{\sigma}\sigma I_\sigma \\ =& \pi\rho_F\rho_0|T^i|^2\int_{-\infty}^{+\infty} dE\Big\{\left[\rho(E_\uparrow)+\rho(E_\downarrow)\right]\left[f(E-eV)-f(E+eV)\right] \\ & -2\rho(E_\downarrow)f(E+\mu_s)-2\rho(E_\uparrow)f(E-\mu_s)\Big\}. \end{aligned} \tag{4.17}$$

The spin accumulation in the superconductor can be written as

$$S(t)=\hbar/2\rho_0\int dE[\rho(E_\downarrow)f(E+\mu_s)-\rho(E_\uparrow)f(E-\mu_s)]. \tag{4.18}$$

This relates the accumulated spin to the chemical potential difference between the up and down spins in the SC. The equation of motion can be formally integrated

$$S(t)=e^{-t/\tau_s}\int_0^t dt' I_s^i(t')e^{t'/\tau_s}. \tag{4.19}$$

Note that I_s^i is also a function of μ_s. The equations (4.17), (4.18), and (4.19) form a self-consistent system of integral equations which can be solved numerically to determine μ_S as a function of V for all times t. An exception to this can be made for very small values of μ_s when we can neglect the dependence of I_s^i on μ_s, and we calculate the accumulated spin and correspondingly of μ_s directly from Eq. (4.19), as done in [26].

When the applied voltage is constant in time the system will end up in a stationary state in which the injected spin current will exactly compensate the spin relaxation in the superconductor such that $dS(t)/dt=0$. Imposing this condition in the equations of motion yields $I_s^i=S/\tau_s$, where now both S and I_s^i are time-independent. Equations (4.17) and (4.18) form a self-consistent system of equations which can be solved numerically to determine the stationary value of μ_S as a function of V. To determine the measured voltage V_m as a function of μ_s, and correspondingly on the value of the applied voltage, V, we need to impose the extra condition that in the detection junction the total electrical current $I_e^d=0$, where, as described in the previous section I_e^d is given by

$$\begin{aligned} I_e^d &= e\sum_\sigma I_\sigma \\ &= \frac{2\pi e^2}{\hbar}\rho_F\rho_0\int_{-\infty}^{+\infty} dE\Big\{\big[|T_\uparrow^d|^2\rho(E_\uparrow)+|T_\downarrow^d|^2\rho(E_\downarrow)\big]f(E-eV) \\ &\qquad\qquad - \big[|T_\uparrow^d|^2\rho(E_\downarrow)+|T_\downarrow^d|^2\rho(E_\uparrow)\big]f(E+eV) \\ &\qquad\qquad - \big[|T_\uparrow^d|^2-|T_\downarrow^d|^2\big]\big[\rho(E_\uparrow)f(E-\mu_s)-\rho(E_\downarrow)f(E+\mu_s)\big]\Big\}, \end{aligned} \tag{4.20}$$

Note that the currents through the injector and the detector satisfy the same equations but with different parameters. Here, for the FM detector the transmission coefficients are spin-dependent $T_\uparrow^d \neq T_\downarrow^d$. If this is not the case, $V_m = 0$ for all accumulated μ_s. Conversely, the measured V_m value depends strongly on the polarisation of the detector $P^d = (|T_\uparrow^d|^2 - |T_\downarrow^d|^2)/(|T_\uparrow^d|^2 + |T_\downarrow^d|^2)$, with a typical experimental $P^d \approx 0.1$ for the Cobalt lead.

4.4 Results for an applied DC voltage

In Fig. 4.2 we present a typical dependence of V_m on V. Similar to Ref. [26] this follows qualitatively the form of $I_s(V)$ which exhibits the same main features as the BCS DOS [26] (e.g. two coherence peaks, a quasi-null value at small V's and a saturation at large V's). To understand the difference between our approach and previous approximations we will separately take into account the effects of two important factors, the non-linearity and the self-consistency. The non-linearity comes into play when H and μ_s are large, and the above current formulas cannot be Taylor expanded in these parameters. The self-consistence expresses the back-reaction of the accumulated μ_s on the injection current; when μ_s is small with respect to the applied voltage, we can neglect it in Eq. (4.17) and solve the equations of motion in a non-self-consistent matter. We begin by analysing the effect of the self-consistence. In Fig. 4.2 we present the dependence of V_m on V obtained both self-consistently (full line) and non-self-consistently (dashed line). It appears that the main difference is quantitative, i.e. the self-consistence is introducing an overall correcting factor which does not depend strongly on V. To test this assumption we write down the self-consistent and non-self-consistent solutions of the equations of motion in the linear limit (small μ_s). In this regime we can perform a Taylor expansion of Eq. (4.18) in μ_S, $S = \hbar\rho_0\rho(\mu_B H)\mu_s^{nsc}$, which together with the condition $I_s^i = S/\tau_s$ yields

$$\mu_s^{nsc} = \tau_s[\hbar\rho_0\rho(\mu_B H)]^{-1} I_s^i(V). \tag{4.21}$$

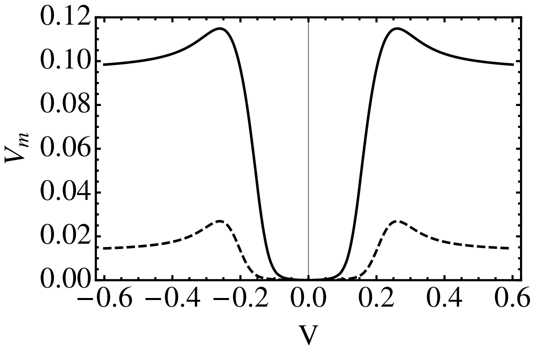

Fig. 4.2 The measured V_m (in meV) as a function of the applied chemical potential V (also in meV) calculated in a self-consistent manner (full line) and non-self consistent manner (dashed line) for parameter values of $\Delta = 0.22meV$, $P^d = 2\%$,and $\tau_s = 0.44$ in the normalised units described in the text. The DOS is considered to be of BCS Dynes type with a $\delta_i = 7\mu V$ for the injection DOS, $\delta_d = 1\mu V$ for the detector DOS. The temperature is taken to $T = 270mK$. The magnetic field is $H = 0.21T$.

We can also solve the equations of motion self-consistently by making a Taylor expansion of Eq. (4.17) in μ_s

$$I_s^i = I_s^i(V) + (2g_{ns}\hbar/e^2)\rho(\mu_B H)\mu_s^{sc} = S/\tau_s, \tag{4.22}$$

with $g_{ns} = (2\pi e^2/\hbar)\rho_F |T^i|^2 \rho_0$ is the normalised conductance of the injection junction. Noting that $S = 2\hbar\rho_0\rho(\mu_B H)\mu_s^{sc}$, we find

$$\mu_s^{sc} = \frac{\tau_s[\hbar\rho_0\rho(\mu_B H)]^{-1} I_s^i(V)}{1 - 2\tau_s g_{ns}/e^2\rho_0} \tag{4.23}$$

and $\mu_s^{sc}/\mu_s^{nsc} = 1/(1-2\tau_s g_{ns}/e^2\rho_0)$. In our numerical calculations we will set $g_{ns}/e^2\rho_0 = 1$, so that τ_s is measured in units of $e^2\rho_0/g_{ns}$. Indeed, it seems that in the linear limit, the non-self-consistent and self-consistent approaches differ by a simple numerical factor, which converges to 1 when $\tau_s \ll 1$. This observations has been checked numerically in Fig. 4.3 where we have plotted the accumulated μ_s calculated using the non-self-consistent and the self-consistent approach (with a correcting factor of $1/(1-2\tau_s)$ taken into account). Indeed we see that the two give the same result in the linear (small V) regime.

It appears thus that the effect of solving the equations of motion in a self-consistent or non-self-consistent manner is mainly quantitative (an overall numerical factor), which is however very important if we are interested in extracting the value of the spin relaxation time from a fit of the experimental data for an applied DC voltage. A factor of 10 difference arising in the model from the self-consistency can give thus a factor of 10 error in the estimation of the spin-relaxation time.

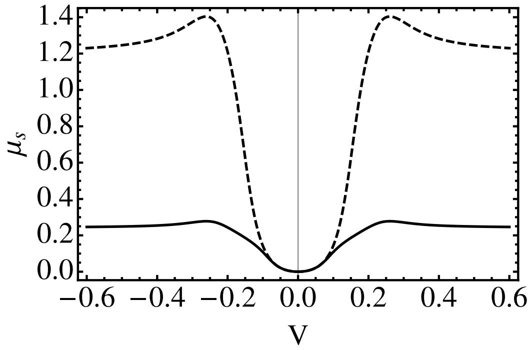

Fig. 4.3 The calculated accumulated spin-chemical potential μ_s (meV) as a function of the applied voltage (meV) using the self-consistent formalism (full line), and the non-self-consistent formalism (multiplied by a factor of $1/(1-2\tau_s)$) (dashed line). The parameters are the same in Fig. 4.2.

The second important factor to be understood is the non-linearity, in particular the non-linearity of the detection. We note that the chemical potential describing the spin accumulation μ_s depends qualitatively similar on the applied V as the measured V_m. The differences come from the non-linearity of the detection junction. To understand this, we have plotted in Fig. 4.4 the measured V_m as a function of the accumulated μ_s. Note the pronounced non-linearity of the detection junction, thus for $V \leq \Delta/2$, corresponding to a small μ_s, we have a linear dependence of V_m on μ_s, $V_m \propto P^d \mu_s$ as expected, while for $V > \Delta/2$ the linearity does not hold (for reminder: $\Delta = 0.22meV$ and $P^d = 2\%$).

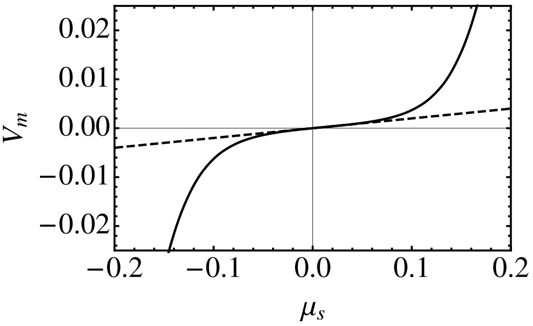

Fig. 4.4 The measured voltage V_m (in meV) as a function of μ_s (in meV) (full line). The dashed line corresponds to $V_m = P^d \mu_s$. The parameters are the same in Fig. 4.2.

4.5 Results for an applied AC voltage

4.5.1 Time-dependent behavior

Numerical results

We now apply a time-dependent (AC) sinusoidal voltage of frequency ω and amplitude V_{rf} on the injector, such that $V(t) = V + V_{rf}\cos(\omega t)$. The expressions for the spin currents do not change (see Eq. (4.17)). The only change comes from the dependence on time of the spin imbalance. We can solve numerically the self-consistent integral equations of motion (Eqs. (4.16)-(4.20)) to obtain the time-dependent $V_m(t)$, $\mu_s(t)$ and accumulated spin $S(t)$, as a function of applied V for various values of frequencies and AC amplitudes.

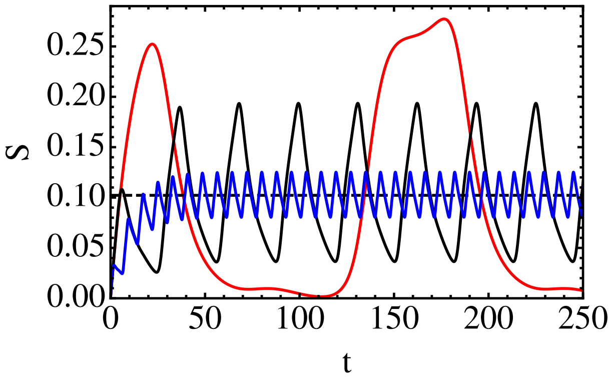

Fig. 4.5 Spin imbalance (in arbitrary units) as a function of time (in units of τ_s) for $V_{rf} = 0.05 meV$ and $\omega = 0.8/\tau_s$ (blue), $\omega = 0.2/\tau_s$ (black), and $\omega = 0.04/\tau_s$ (red). Note that the average of the oscillations (denoted by the dotted line) is independent of frequency, while their amplitude is not.

We begin by plotting the accumulated spin $S(t)$ as a function of time. The time dependence of the spin accumulation can be understood easily thinking that the superconductor acts as a capacitor (its charge could be viewed as the spin imbalance). Indeed, for large frequencies the capacitor is loading (the spins are accumulating up to a maximal value) but its decreasing never happens because the spin relaxation time is larger than the period of the oscillations. On the contrary, for small frequencies voltage the spins can relax because of the large period of the oscillations. In Fig. 4.5 we plot $S(t)$ for three values of frequency, $\omega = 0.8/\tau_s$, $\omega = 0.2/\tau_s$ and $\omega = 0.04/\tau_s$. All other parameters are the same as in the previous section. We note that the average of the oscillations is independent of frequency, while their amplitude is not. The larger the frequency, the more the behavior of $S(t)$ approaches that of a charging capacitor with smaller and smaller oscillations around the saturation value.

It would thus seem that experimentally one cannot see a frequency dependence for the

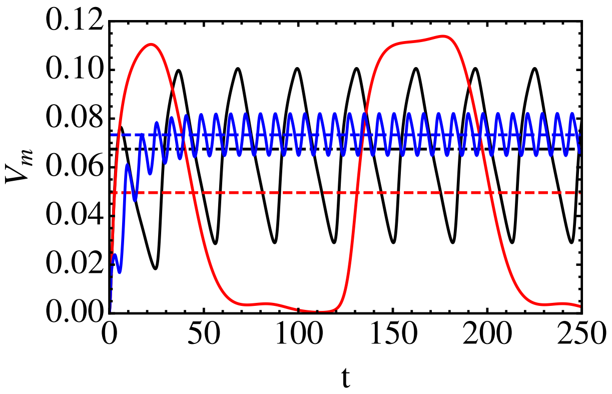

Fig. 4.6 Calculated V_m (in meV) as a function of time (in units of τ_s) for $V_{rf} = 0.05meV$, and $\omega = 0.8/\tau_s$ (blue), $\omega = 0.2/\tau_s$ (black), and $\omega = 0.04/\tau_s$ (red). Note that both the averages (denoted by the corresponding dashed lines) and the amplitude of the oscillations depend on frequency.

time-averaged spin accumulation. However, in an actual experiment one does not measure S but V_m, which can exhibit a strong non-linear behavior. We should then expect that if the amplitude of the oscillations in $S(t)$ depends on frequency, the time average of V_m depends on frequency via rectification effects. In Fig. 4.6 we plot the time dependence of V_m for three different frequencies and we see that indeed both the amplitude of the oscillations and the time average depend on frequency.

Taylor expansion

To understand the above numerical results we study a few limiting cases that can be solved analytically. For a small applied AC voltage ($V_{rf} \ll V$), with $V(t) = V + V_{rf}\cos(\omega t)$, we can use a Taylor expansion, and the spin current can be expressed as

$$\begin{aligned} I_s(t) &= I_s[V + V_{rf}\cos(\omega t)] \\ &\approx I_s[V] + \left.\frac{\partial I_s}{\partial V}\right|_V .V_{rf}\cos(\omega t) + \frac{1}{2}\left.\frac{\partial^2 I_s}{\partial V^2}\right|_V .[V_{rf}\cos(\omega t)]^2 + \ldots \end{aligned} \tag{4.24}$$

Injecting Eq. (4.24) in Eq. (4.19) gives us an expansion for the spin imbalance in powers of V_{rf} : $S(t) = S_0(t) + S_1(t) + S_2(t) + \ldots$. We focus on the first two terms in the expansion, but the next orders can be studied in a similar fashion. For times much more larger than τ_s we obtain

$$S(t) = I_s(V)\tau_s + \left.\frac{\partial I_s}{\partial V}\right|_V .V_{rf}\frac{\tau_s}{1+\tau_s^2\omega^2}\left[\cos(\omega t) + \omega\tau_s\sin(\omega t)\right]. \tag{4.25}$$

We see from the above formula that the average accumulated spin is independent of frequency, consistent with the numerical analysis in the previous section (see Fig. 4.5). However, the amplitude of the oscillations does depend on frequency. By having a quick look at the above expression we can directly point out two regimes. Thus, for $\omega\tau_s \ll 1$ we should expect a constant behavior for the dependence of the amplitude of the oscillations with the frequency, as $\frac{\tau_s}{1+\tau_s^2\omega^2} \longrightarrow \tau_s$. The opposite regime where $\omega\tau_s \gg 1$ gives us a $1/\omega$ dependence. This behavior is confirmed by a numerical analysis of the dependence of the amplitude of oscillations with the frequency where we indeed note a crossover behavior for a frequency $\omega \approx 1/\tau_s$. However this analysis in valid only when V_{rf} is very small, and in the regime in which the system is well described by the non-self-consistent calculation. Also, since the timescales involved are very short, it is much harder to have experimentally access to the amplitude of the oscillations than to the time averages, and in what follows we will focus rather on time-averaged quantities than on time-dependent ones. We expect that the non-linearity will give rise to a frequency dependence even when averaging over time, allowing us to detect directly this spin relaxation time in the frequency domain. Experimentally, one uses $0.5-50MHz$ frequencies since we expect a spin relaxation time of the order of nanoseconds.

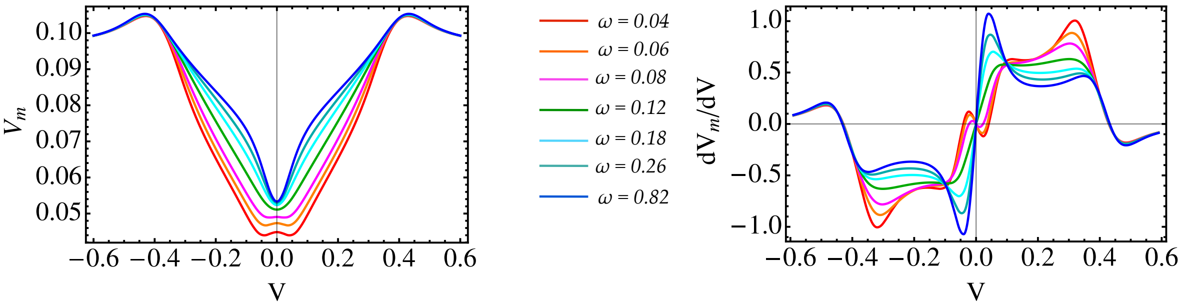

Fig. 4.7 Dependence of V_m(in meV) and dV_m/dV as a function of the applied V (in meV) for various frequencies (in units of $1/\tau_s$), at fixed AC amplitude ($V_{rf} = 0.2meV$).

4.5.2 Time-averaged quantities

In this section we study the dependence of the average measured V_m as a function of the applied voltage for different AC amplitudes and frequencies. We begin by plotting V_m and its derivative dV_m/dV as a function of V for different frequencies at fixed AC amplitude (see Fig. 4.7). All frequencies are given in units of $1/\tau_s$. Subsequently, in Fig. 4.8 and Fig. 4.9 we fix the frequency and plot the average V_m and the derivative of the average dV_m/dV as a function of applied V for various values of the AC amplitude. Finally, in Fig. 4.10 we plot the dependence of V_m on the AC frequency at a fixed AC voltage amplitude and for various applied voltages. We note that the main features that we observe, i.e a flattening of the V_m dependence on V, with an eventual extra peak arising at $V = 0$, a doubling of the peaks in the dV_m/dV dependence on V, whose position depend quasi-linearly on V_{rf}, and a

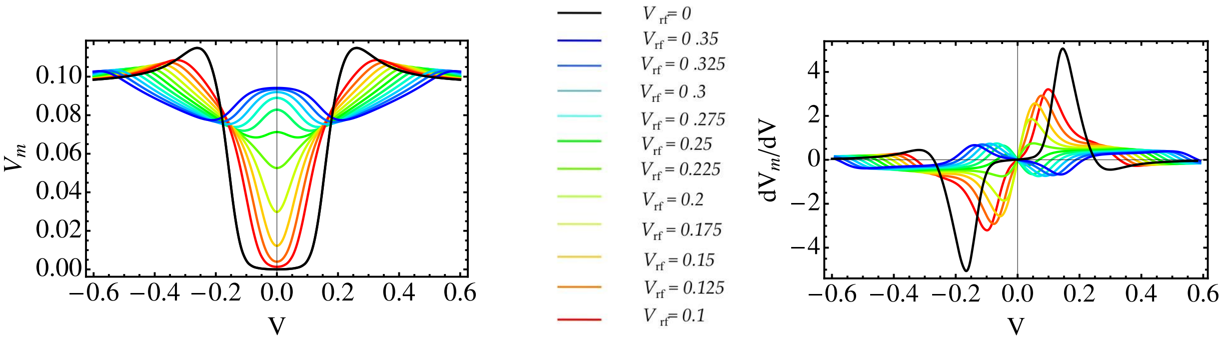

(4.26)

Fig. 4.8 Dependence of V_m (in meV) and dV_m/dV as a function of the applied V (in meV) for various values of the AC amplitude at a fixed frequency of $\omega = 0.2/\tau_s$.

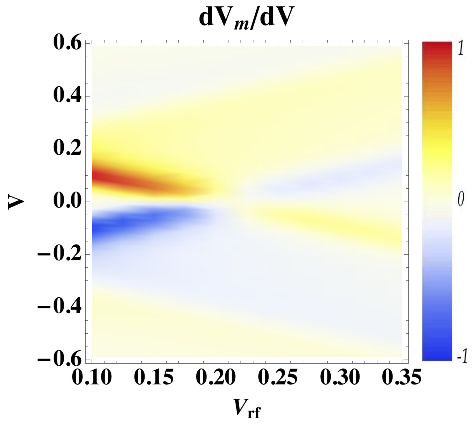

(4.27)

Fig. 4.9 3D plot of Fig 4.8: Dependence of dV_m/dV as a function of the applied V (in meV) and V_{rf} at a fixed frequency of $\omega = 0.2/\tau_s$.

saturation of V_m and dV_m/dV with increasing the frequency, are qualitatively similar to what is measured in Ref. [27]. The frequency at which the saturation occurs is directly related to the inverse of the spin-relaxation time. Thus our theory seems to describe very well the frequency and amplitude dependence of the measured accumulation. We have checked that while the measured V_m and μ_s do depend on the frequency, the accumulated spin S does not as described also in the previous section. We have calculated the accumulated spin S (see Fig. 4.11) for different values of V and frequency and we have seen that S is indeed unaffected by the frequency.

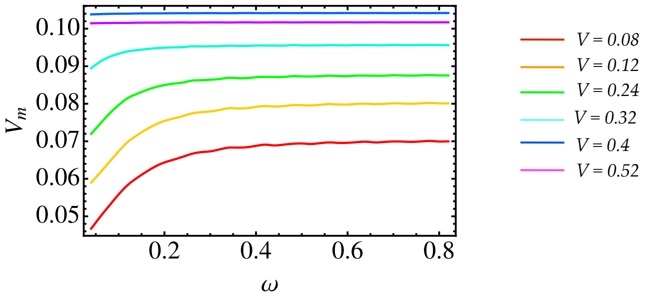

Fig. 4.10 Dependence of V_m (in meV) on the AC frequency (in units of $1/\tau_s$) at fixed AC voltage amplitude $V_{rf} = 0.2meV$, for various applied voltage V (in meV).

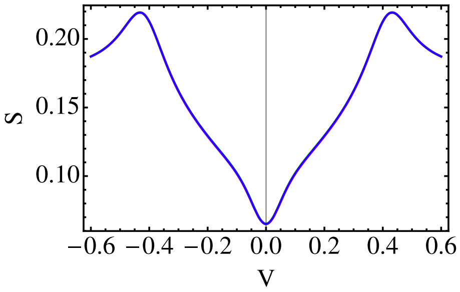

Fig. 4.11 Dependence of S (in arbitrary units) on V at fixed AC voltage amplitude $V_{rf} = 0.2meV$ and for the same frequencies ω as in Fig. 4.7 (all curves overlap).

4.5.3 Different type of AC voltage: rectangular pulse

To get an analytical understanding of the numerical results presented in the previous section we consider also a different type of AC signal, for example a chain of rectangular pulses. In this case we can also calculate analytically the form of the spin imbalance, if we make the assumption that the self-consistent effects are negligible. The pulse has the following shape

$$V_{rf}(t) = \sum_{i=0}^{N} V_{rf}\left[\theta\left(t - \frac{2\pi i}{\omega}\right) - \theta\left(t - \varepsilon - \frac{2\pi i}{\omega}\right)\right], \tag{4.28}$$

with $T = 2\pi/\omega$ the period of the signal, V_{rf} its amplitude, and ε the width of the pulse. The difference of spin imbalance between the stationary regime ($V_{rf} = 0$) and the time-dependent one ($V_{rf} \neq 0$) can be calculated exactly using Eq. (4.19):

$$\begin{aligned}\delta S(t) &= S[V_{rf}(t)] - S[V_{rf}(t) = 0] \\ &= e^{-t/\tau_s} \int_0^t e^{x/\tau_s} [I_s^i[V + V_{rf}(x)] - I_S^i(V)] dx.\end{aligned} \tag{4.29}$$

Performing the integral over time leads to

$$\begin{aligned}\delta S(t) = \{I_s^i[V + V_{rf}(x)] - I_S^i(V)\}\tau_s e^{-t/\tau_s} &\left[(e^{\varepsilon/\tau_s} - 1)\frac{e^{2\pi N/\omega\tau_s} - 1}{e^{2\pi/\omega\tau_s} - 1}\right. \\ &+ \theta\left(t - \frac{2\pi N}{\omega} - \varepsilon\right)\left(e^{2\pi N/\omega\tau_s + \varepsilon/\tau_s} - e^{2\pi N/\omega\tau_s}\right) \\ &\left.+ \theta\left(\frac{2\pi N}{\omega} + \varepsilon - t\right)\left(e^{t/\tau_s} - e^{2\pi N/\omega\tau_s}\right)\right].\end{aligned} \tag{4.30}$$

The average of Eq. (4.30) can be written as $\delta\bar{S} = 1/T \int_0^T \delta S(t) dt$ and leads to

$$\delta\bar{S} = [I_s^i(V + V_{rf}) - I_S^i(V)]\frac{\omega\varepsilon\tau_s}{2\pi} + \mathscr{O}\left(e^{-2\pi/\omega\tau_s}\right). \tag{4.31}$$

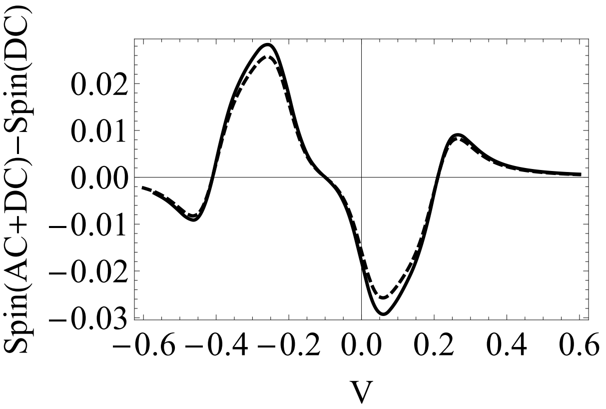

Fig. 4.12 Numerically calculated V_m (full line) (in arbitrary units), and $I_s^i(V+V_{rf})-I_S^i(V)$(dashed line), as a function of V for $V_{rf}=0.2meV$ and the frequency $\omega=0.04/\tau_s$. Note the qualitatively similar behavior of the two curves (a constant has been introduced to uniformise the two curves).

If the pulse constitutes a constant fraction of the period ($\omega\varepsilon$ is constant), the accumulated average S should be independent of frequency. We have checked that is indeed the case by a numerical analysis. Also this is consistent with our previous observations for the sinusoidal signal. An interesting observation that we make is that, as it can be seen from Eq. (4.31) the dependence of S on V is given generically by $I_s^i(V+V_{rf})-I_S^i(V)$. In Fig. 4.12 we plot the dependence on V_m as a function of V obtained numerically for a specific value of V_{rf} and of frequency. We also sketch the behavior of $I_s^i(V+V_{rf})-I_S^i(V)$, showing that indeed, to first approximation, the behavior of V_m follows qualitatively the behavior of $I_s^i(V+V_{rf})-I_S^i(V)$.

A simple generalisation can be made to understand qualitatively the behavior of V_m with V for the sinusoidal signal. To first approximation a sinusoidal signal is equivalent to a superposition of two V_{rf} and $-V_{rf}$ pulses, with an $\varepsilon\omega=1/2$. We would then expect an overall dependence of V_m qualitatively similar with $I_s^i(V+V_{rf})+I_s^i(V-V_{rf})-2I_S^i(V)$. In Fig. 4.13 we plot the dependence of the excess accumulated spin as a function of V obtained numerically for a specific value of $V_{rf}=0.2meV$ and $\omega=0.04/\tau_s$ for a sinusoidal signal, and we also sketch the behavior of $I_s^i(V+V_{rf})+I_s^i(V-V_{rf})-2I_S^i(V)$, showing that, remarkably enough, the two behaviors are indeed qualitatively similar.

Differences between accumulation and relaxation times

In this section we consider the possibility that the time for accumulation (loading) and relaxation (unloading) are different. Such phenomenon could be detected by applying a time

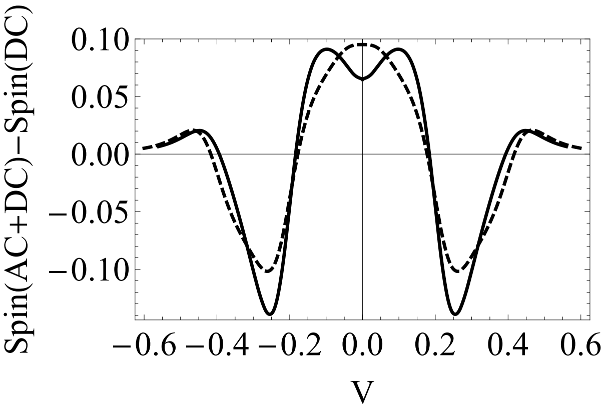

Fig. 4.13 Measured excess accumulated spin (full line), and $I_s^i(V+V_{rf})+I_s^i(V-V_{rf})-2I_S^i(V)$(dashed line), as a function of V for a sinusoidal signal with $V_{rf}=0.2meV$ and the frequency $\omega=0.04/\tau_s$. Note the qualitatively similar behavior of the two curves.

dependent voltage with the following shape (see Fig. 4.14)

$$\begin{aligned} V_{rf}(t) = &\sum_{i=0}^{N} A_1 \left[\theta\left(t-\frac{2\pi i}{\omega}\right) - \theta\left(t-\varepsilon_1-\frac{2\pi i}{\omega}\right)\right] \\ &+ \sum_{i=0}^{N} A_2 \left[\theta\left(t-\varepsilon_1-\frac{2\pi i}{\omega}\right) - \theta\left(t-\varepsilon_1-\varepsilon_2-\frac{2\pi i}{\omega}\right)\right]. \end{aligned} \tag{4.32}$$

This is because if $A_1>0$ and $A_2<0$ the first step corresponds to the loading of the superconductor and is controlled by τ_1, and the second one to the unloading and is controlled by τ_2. A similar calculation as before can be performed leading to the following form for the average spin imbalance

$$\frac{\delta\bar{S}}{I_s^i(V+V_{rf})-I_S^i(V)} = \frac{\omega(A_1\varepsilon_1\tau_1+A_2\varepsilon_2\tau_2)}{2\pi}. \tag{4.33}$$

By setting $\varepsilon_1=\varepsilon_2=\varepsilon$, $A_1=A_2=A$ and $\tau_1=\tau_2=\tau$ we effectively restore the previous situation

$$\delta\bar{S} = [I_s^i(V+V_{rf})-I_S^i(V)]\frac{2\tau\omega\varepsilon}{2\pi}, \tag{4.34}$$

with τ_s being replaced by $2\tau=\tau_1+\tau_2$. We can see that in this limit the dependence is still linear with frequency. One important observation to make is that the difference between τ_1 and τ_2 can be measured directly by applying an AC voltage with $A_1=-A_2$ and $\varepsilon_1=\varepsilon_2$. If the two times are different, the average excess accumulation will be non-zero, which is not the case when $\tau_1=\tau_2$.

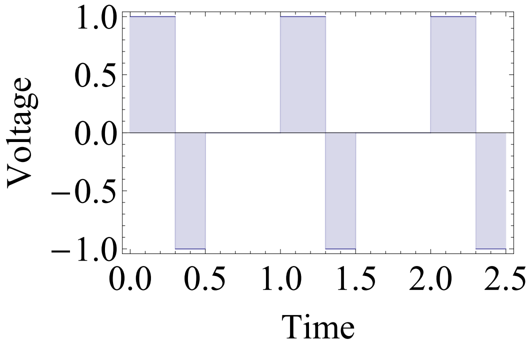

Fig. 4.14 Applied time dependent voltage for $A_1 = -A_2 = 1$, $\varepsilon_1 = 0.3$ and $\varepsilon_2 = 0.2$.

4.6 Conclusion

We have calculated the accumulated spin in a junction between a superconductor and a normal or ferromagnetic contact, taken out of equilibrium, and in the presence of a Zeeman magnetic field. The effects of DC and AC applied voltages, for different amplitudes and frequencies, have been considered. For an applied DC voltage, the dependence of the measured spin accumulation V_m on the applied voltage V roughly follows the form of the DOS, i.e. two coherence peaks, a reduction at small biases, and a saturation for large applied voltages. When an AC component is added to the applied voltage one observes a flattening of the measured spin voltage with the applied V, with an eventual extra peak arising at $V = 0$, a doubling of the peaks in the dV_m/dV dependence on V, whose position depends quasi-linearly on the amplitude of the AC voltage, and a saturation of V_m and dV_m/dV with increasing the frequency. The frequency at which the saturation occurs is directly related to the inverse of the spin-relaxation time. Our theoretical predictions show a qualitative agreement with the experimental measurements in Ref. [27]. A detailed comparison between our theoretical analysis and these experimental measurements allows the extraction of the spin relaxation time in the SC, in particular from the dependence of the measured accumulation as a function of frequency. We find that this value is of the order of ns.

Frequency-Domain Measurement of the Spin Imbalance Lifetime in Superconductors

C. H. L. Quay,[1,*] C. Dutreix,[1] D. Chevallier,[2] C. Bena,[1,3] and M. Aprili[1]

[1] *Laboratoire de Physique des Solides (CNRS UMR 8502),*
Bâtiment 510, Université Paris-Sud, 91405 Orsay, France
[2] *Instituut-Lorentz, Universiteit Leiden,*
P.O. Box 9506, 2300 RA Leiden, The Netherlands
[3] *Institut de Physique Théorique, CEA Saclay 91190 Gif-sur-Yvette, France.*

(Dated: August 14, 2014)

Abstract

We have measured the lifetime of spin imbalances in the quasiparticle population of a superconductor in the frequency domain. A time-dependent spin imbalance is created by injecting spin-polarised electrons into a thin-film mesoscopic superconductor (Al) at finite excitation frequencies and finite magnetic field. The time-averaged value of the spin imbalance as a function of excitation frequency shows a cut-off corresponding to the spin lifetime. The spin lifetime is relatively constant in the accessible ranges of magnetic fields and temperatures; its value is in agreement with previous estimates. Our data are qualitatively well-described by a theoretical model taking into account all quasiparticle tunnelling processes from a normal metal into a superconductor.

PACS numbers: 74.40.Gh, 75.76.+j, 74.78.Na

---

[*] Electronic address: charis.quay@u-psud.fr

Spin-polarised electrons injected into superconductors eventually disappear into the condensate, which is made up of Cooper pairs of electrons of opposite spin. To disappear, the injected electrons — which become quasiparticles in the superconductor — must lose energy, flip their spin and recombine with quasiparticles of the opposite spin to form Cooper pairs. These processes may be sequential or occur in parallel. For example, (1) quasiparticles may undergo elastic or inelastic spin flip processes, (2) quasiparticles may lose energy without flipping their spin, and (3) low-energy quasiparticles recombining in pairs necessarily lose a quantity of energy equivalent to the superconducting gap, usually in the form of a phonon. The characteristic timescale for these processes — as well as the order in which they occur and any interdependence between them — can shed light on microscopic properties of the superconductor, including relaxation pathways [1–8] as well as the gap structure and the pairing mechanism in unconventional superconductors [9–12].

Time- and frequency-domain experiments, whether using transport, optical pump-probe or other techniques, provide the most direct measure of the timescales involved [13–16]. Most of the work in this area has focused on the recombination of quasiparticles, usually with techniques sensitive to the number of quasiparticles and their diminution over time. A quasiparticle population which is larger than that at equilibrium does not however exhaust the possible non-equilibrium phenomena: the quasiparticle population can also manifest spin and/or charge imbalances [17–23]. These do not necessarily relax in the same way, nor on the same timescale. In this Letter we report the first frequency-domain measurement of the lifetime of a spin imbalance in the quasiparticle population in a mesoscopic superconductor.

The idea of our experiment, in brief, is as follows: We inject spin-polarised quasiparticles into a superconductor at a finite frequency $f_{RF} = \omega/2\pi$ while measuring the time-averaged spin-up quasiparticle chemical potential, $< \mu_s(\omega, t) >_t$. We expect a cut-off at roughly $\omega = 1/\tau_s$, with τ_s the spin lifetime of quasiparticles in the superconductor (Figure 1b). This is akin to filling a leaky bath from a tap, turned on and off at a regular rhythm, while measuring the time-averaged water level in the bath.

Our samples, fabricated with standard electron-beam lithography and evaporation techniques, are thin-film superconducting (S) bars, with a native insulating (I) oxide layer, across which lie normal metal (N) and ferromagnetic (F) electrodes used either as 'injectors' or as 'detectors'. (Figure 1) In our devices, S is aluminium, I Al_2O_3, F cobalt and N thick aluminium with a critical magnetic field of ~50mT. (In all the data shown here, this Al electrode

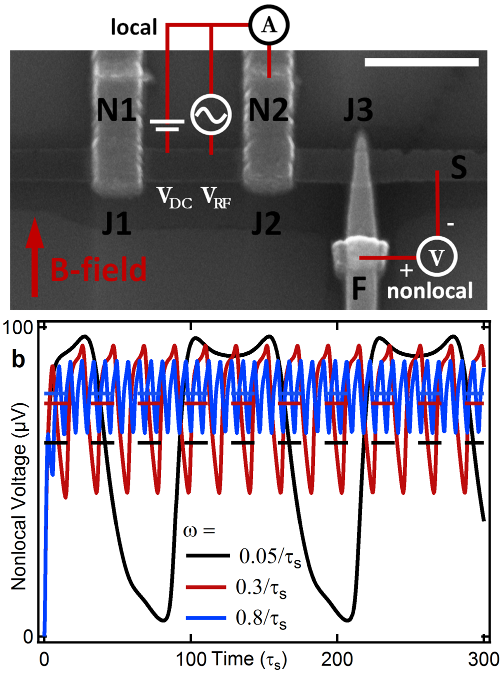

FIG. 1: (a) Scanning electron micrograph of a typical device (scale bar = 1μm) and schematic drawing of the measurement setup. S = superconductor (~8.5nm thick Al film with a native oxide), N = normal metal (100nm Al), F = ferromagnet (40nm Co, with a 4.5nm Al capping layer). The native oxide on S constitutes a tunnel barrier between it and any other given electrode. Quasiparticles are injected into S across a tunnel barrier by applying a voltage V_{DC} across J1 or J2. These are spin-polarised because of the Zeeman field in S. The nonlocal voltage V_{NL} and differential nonlocal signal dV_{NL}/dV_{DC} are measured between a distant ferromagnetic electrode and the superconductor (at J3) as a function of magnetic field and temperature, as well as as a function of the amplitude V_{RF} and frequency $f_{RF} = \omega/2\pi$ of high-frequency (1-50MHz) voltages applied to the injection electrode. The local conductance dI/dV_{DC} is measured simultaneously at the injection electrode. (b) Numerical calculations of $V_{NL}(t)$ (and its time average) for different ω. The time-averaged V_{NL} depends on ω; this is our main experimental result. These calculation were done for $V_{DC} = 200\mu$V, $V_{RF} = 250\mu$V and using the measured local conductance at J2 and J3 at 680mT.

is in the normal state.) A typical device is shown in Figure 1a. As in previous experiments, the SIF and NIS junctions have 'sheet resistances' respectively of ~ 2 and $\sim 6 \cdot 10^{-6}\Omega \cdot cm^2$ (corresponding to barrier transparencies of ~ 4 and $\sim 1 \cdot 10^{-5}$) and tunnelling is the main transport mechanism across the insulator. (See Supp. Info. of Ref. [19]) Measurements were performed at temperatures down to 50mK, in a dilution refrigerator.

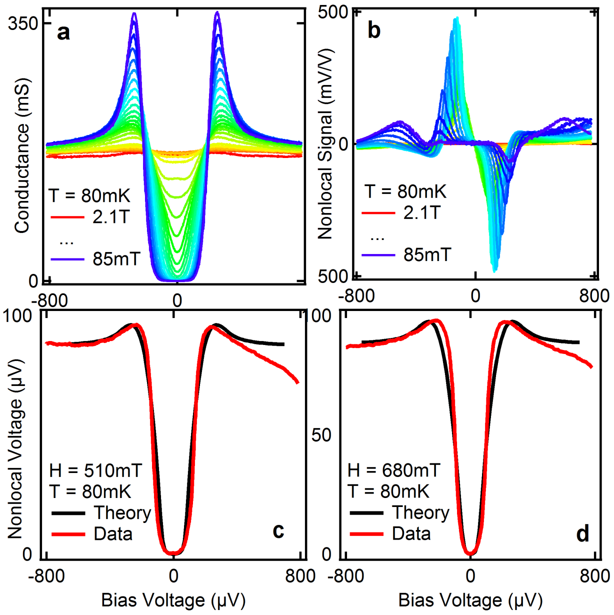

FIG. 2: (a) The conductance dI/dV_{DC} across J2, which is proportional to the quasiparticle density of states in the superconductor, as a function of V_{DC} at different magnetic fields. (b) The *differential* nonlocal signal dV_{NL}/dV_{DC} measured at J3 as a function of V_{DC} at the same fields. (c,d) Theoretical fits to $V_{NL}(V_{DC})$ measured at J3 at two different fields. These yield τ_s of several nanoseconds.

We simultaneously perform local and non-local transport measurements using standard lock-in techniques: We apply a voltage V_{DC} across junction J2, between N and S, and measure the ('local') current I injected into the superconductor through J2 and the ('non-local') voltages across the other junctions, which act as detectors. We also measure the local conductance dI/dV_{DC} and the nonlocal differential signal, dV_{NL}/dV_{DC}. The distance between injection and detection junctions is $\simeq 1\mu$m, well within the Al spin relaxation length in the superconducting state [20]. In the presence of an in-plane magnetic field, H (applied parallel to the non-superconducting electrodes), electrons injected into the superconductor create a spin imbalance in its quasiparticle population due to the Zeeman effect [19]. The non-local voltage drop V_{NL} at J3 is proportional to either $(\mu_{QP\uparrow} - \mu_P)$ or $(\mu_{QP\downarrow} - \mu_P)$, depending on the relative alignments of the F magnetisation and the magnetic field. Here $\mu_{QP\alpha}$ is the chemical potential of the spin α quasiparticle population and μ_P the Cooper pair chemical potential. We remind the reader that $\mu_C = (\mu_{QP\uparrow} + \mu_{QP\downarrow})/2$ and $\mu_S = (\mu_{QP\uparrow} - \mu_{QP\downarrow})/2$ quantify charge and spin accumulation respectively. The non-local voltage drop at J1 is proportional to $\mu_C - \mu_P$.

To explore the frequency dependence of the spin imbalance, we add higher-frequency components of amplitude V_{RF} and frequency f_{RF} =500kHz–50MHz to V_{DC} via a bias-tee located next to the device and at low-temperature.

Before presenting the experimental data, let us sketch out our main theoretical expectations. We assume that the spin accumulation, S in the superconductor satisfies

$$\frac{dS(t)}{dt} = I_s(t) - \frac{S(t)}{\tau_s}, \tag{1}$$

where τ_s is the spin relaxation time in the superconductor and I_s the spin current.

This equation admits an exact analytical solution:

$$S(t) = e^{-t/\tau_s} \int_0^t dt' I_s(t') e^{t'/\tau_s}. \tag{2}$$

We first consider a spin current of the form $I_s(t) = I_{DC} + I_{RF}e^{i\omega t}$, where I_{DC} and I_{RF} are constants, we then have

$$S(t) = \tau_s I_{DC} + \frac{\tau_s I_{RF}}{1 + \omega^2 \tau_s^2} e^{i(\omega t + \alpha)} + \text{transient terms} \tag{3}$$

with α a constant phase. The amplitude of the oscillations in $S(t)$ (and thus $\mu_s(t)$ and $V_{NL}(t)$, the quantity we measure) are frequency-dependent and show a Lorentzian cut-off behaviour. This could be measured with high-frequency detection techniques.

If, however, the spin current is generated by a sinusoidal voltage, which we assume for the moment to be small, we can write

$$I_s(t) = I_s[V(t)] = I_s[V_{DC} + V_{RF}cos(\omega t)] = \sum_{n=0}^{\infty} \frac{1}{n!} \left.\frac{\partial^n I_s}{\partial V^n}\right|_{V=V_{DC}} [V_{RF}cos(\omega t)]^n \tag{4}$$

and insert this into Eq. 4 for $S(t)$. If the current-voltage characteristic of the injection junction is nonlinear, a frequency cut-off should also appear in the time-averages of $S(t)$, $\mu_s(t)$ and $V_{NL}(t)$. Numerical work, with no approximations and assuming a non-linear injection junction, shows that this is indeed the case for $\mu_s(t)$ and $V_{NL}(t)$ though the cut-off was not observable in $S(t)$ [24]. In the case of linear injection, a non-linear detection junction will nevertheless yield a frequency cut-off in $V_{NL}(t)$. In the case of injection which is already non-linear, detector nonlinearity can further enhance the cut-off behaviour. In our devices, both injection and detection junctions are non-linear, due to the quasiparticle density of states in the superconductor.

Further details of our theoretical model, which takes into account spin but not charge imbalance, can be found in Ref. [24]. Our model is based on previous work by Zhao and Hershfield [22], which takes into account all quasiparticle tunnelling process at a normal-superconducting junction, extended to include the Zeeman effect induced by the magnetic field. In contrast to the (similar) model presented in our previous work [19], no assumptions were made about the amplitude of the Zeeman energy or μ_S (which can be up to half the size of the superconducting gap in these measurements).

Turning now to our measurements, we begin by characterising our device in the absence of high-frequency excitation. Figures 2(a) shows the local conductance as a function of bias voltage and magnetic field. We see that, for this device, the superconducting critical field at J2 is ∼1.9T. Figure 2(b) shows the corresponding differential nonlocal signal measured at J3. We remind the reader that, as the injection electrode is normal, the (anti-)symmetric part of this signal comes from the charge (spin) imbalance [19]. In contrast, if the injection electrode were ferromagnetic (and the S DOS highly nonlinear), the 'spin imbalance peaks' in the differential nonlocal signal would be of unequal heights [20]. As in our previous work, we see a spin signal which first increases with magnetic field then dies out as the magnetic field approaches its critical value. Theoretical fits to these data at fixed magnetic field such as those shown in Figures 2(c) and (d) allow us to estimate the spin lifetime τ_S at several magnetic fields, yielding results on the order of several nanoseconds, consistent with previous measurements.

Note that spin lifetimes estimated from these fits are good only to about an order of magnitude as it is difficult to theoretically account for effects on the superconducting DOS due to stray fields coming from the cobalt electrode. We emphasise, nevertheless, that our theoretical model is able to reproduce all qualitative features of our data. (Figures 2–4, Ref. [24])

We apply a magnetic field of $H = 680mT$ (to obtain a large non-local signal) and a sinusoidal excitation at 1MHz while sweeping the V_{DC} and varying the RF power. The results are shown in Figures 3(c)–(f). The main effect of the RF excitation on both the local conductance and the nonlocal signal is the phenomenon known as 'classical rectification': As sinusoidal signals spend most time at their extrema, each feature in the original trace is ‘split’ by a distance in bias voltage corresponding to the peak-to-peak amplitude of the RF excitation. These splitting of the BCS coherence peaks in the local conductance (Figure 3(c)) as well as that of the spin imbalance peaks in the nonlocal conductance (Figure 3(d)) are well-reproduced qualitatively by our theory. (Figure 3(a-b)) Figure 3 looks the same for all frequencies, modulo an offset in the RF power due to frequency-dependent attenuation in the RF lines. These measurements can thus be used as a calibration of RF power.

We next study the frequency-dependent response of our system at constant RF amplitude, using the value of the local conductance at zero bias voltage as a calibration of RF amplitude. (The RF amplitude can be more accurately determined from the location of the ‘classically rectified’ peaks and is generally $\sim 250\mu$V.) Figure 4a shows the non-local signal as a function of bias voltage at constant RF amplitude at 1MHz and 50MHz. For both frequencies, ‘classically rectified’ peaks appear at the same location, but their amplitudes are different: At frequencies which are high compared to $\sim 1/2\pi\tau_S$, the classifically-rectified peaks have smaller amplitudes than they do at low frequencies. (Whether peak amplitudes increase or decrease with frequency depend on the particular parameters of the system. [24]) To track the frequency evolution of the peak amplitude, we measure the nonlocal signal as a function of RF frequency at the bias voltages indicated by the dashed lines (Figures 4(c) and (d)). Fitting Lorentzians to our data yields spin lifetimes of 10ns and 16ns, consistent with previous results. However, our numerical results indicate that such fits can over-estimate τ_S by a factor of 2–3 depending on the bias voltage at which the cut-off is measured.

Measurements similar to those shown in Figure 4 were also performed at different fields (at the base temperature of the dilution refrigerator, ~60mK) and at different temperatures (at 680mT). These results are shown in Figure 5. No significant change in the cut-off frequency (within measurement error) was observed in the range of accessible temperatures and magnetic fields.

To ascertain that the cut-off was not due to the measurement circuit, we modified the latter slightly, obtaining the same result. We measured similar cut-offs in samples with different detector differential resistances at zero applied voltage (different levels of depairing due to stray fields), thus ruling out detector bandwidth effects. We also checked that the injection of electrons at several times the superconducting gap energy did not significantly affect the quasiparticle temperature, thus also ruling out thermoelectric effects. (See Supplementary Information.)

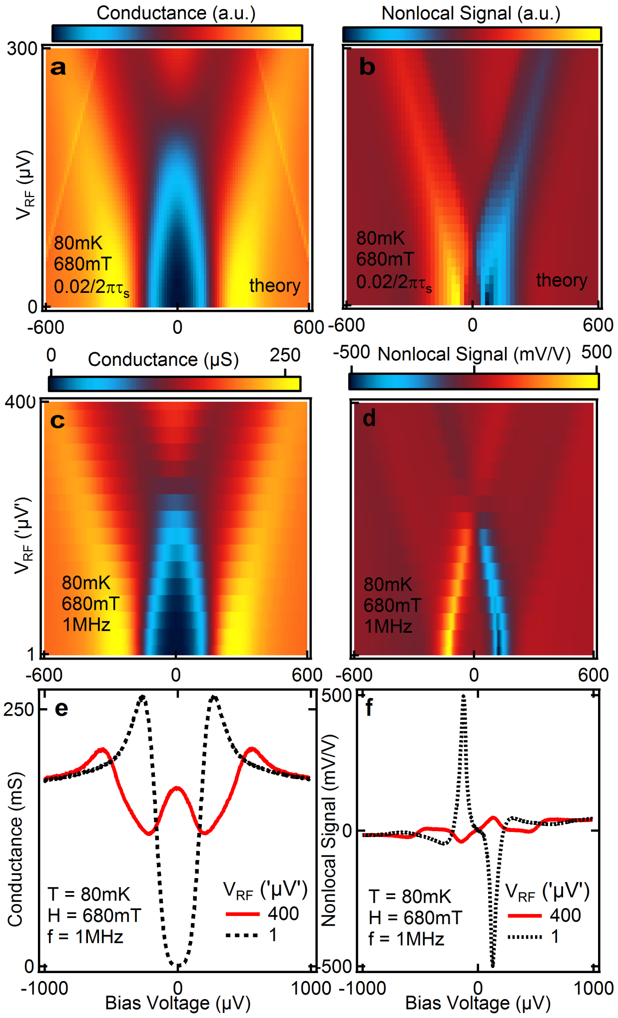

FIG. 3: (a) Calculated local conductance dI/dV_{DC} as a function of RF amplitude V_{RF} at a magnetic field of 680mT, based the superconducting DOS extracted from the measured local conductance at $V_{RF} = 0$. (b) Calculated differential nonlocal signal dV_{NL}/dV_{DC} as a function of V_{RF} at a magnetic field of 680mT, based on the superconducting DOS extracted from the measured local conductance at $V_{RF} = 0$. (c) Measured local conductance at J2 as a function of V_{RF} at $f_{RF} =$ 1MHz and $H =$ 680mT. (d) Measured differential nonlocal signal at J3 as a function of of V_{RF} at $f_{RF} =$ 1MHz and $H =$ 680mT. Classical rectification is the dominant RF effect. The V_{RF} given here are a little higher than what actually arrives at the sample due to attenuation in the line. As noted in the main text, V_{RF} can in any case be estimated from the classical rectification of features in the $V_{RF} = 0$ trace. (e,f) Two slices of (c,d).

In conclusion, we have measured the lifetime of spin imbalances in the quasiparticle pop-

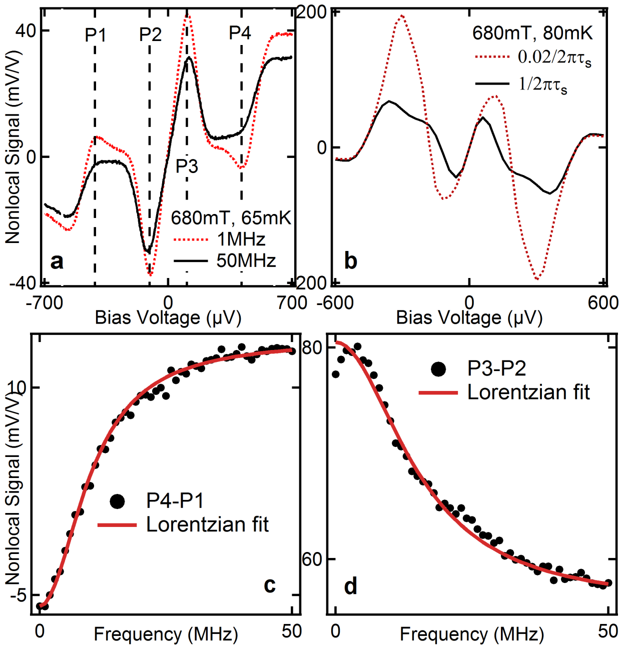

FIG. 4: (a) Measured local conductance dI/dV_{DC} at J2 as a function of V_{DC} with constant-power excitations at f_{RF} = 1MHz, 50MHz. (b) Numerical calculation of the local conductance as a function of V_{DC} with constant-power excitations at $f_{RF} = 0.02/2\pi\tau_s$, $1/2\pi\tau_s$, based on the superconducting DOS extracted from the measured local conductance at $V_{RF} = 0$. (c,d) Local conductance at J2 at the V_{DC} values indicated in (a) as a function of f_{RF}. We subtract 'opposing' peaks to obtain the anti-symmetric part of the signal, which is due to spin. Lorentzian fits give τ_s = 16ns and 10ns respectively; however, these may be slight over-estimates (see text).

ulation of a superconductor in the frequency domain. This is the most direct measurement to date of this quantity. The charge lifetime could in principle be measured in a similar way, at much higher excitation frequencies. Pushing these experiments one step further, one could look at variations in the spin accumulation either in real-time or at the excitation frequency. All of these techniques could in principle be used to measure spin lifetimes in other superconducting materials.

Acknowledgments

We thank J. Gabelli for helpful disucssions on spin dynamics in superconductors, and J. S. Meyer and M. Houzet for the same on thermoelectric effects. This work was funded by

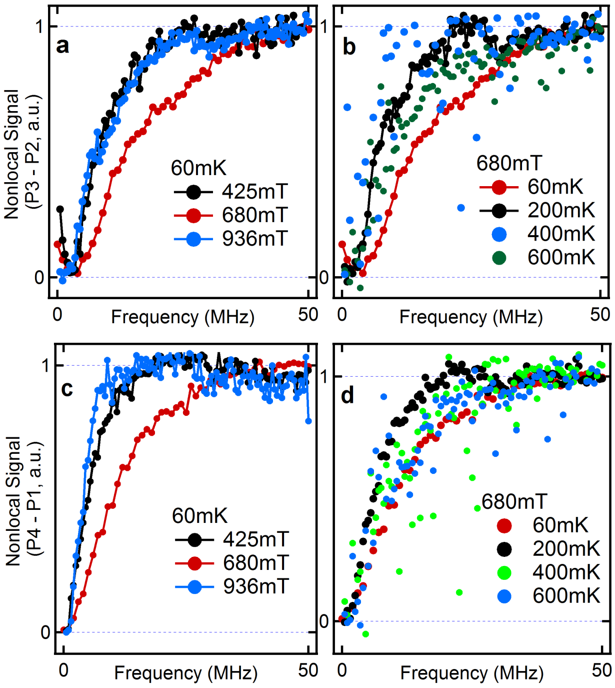

FIG. 5: Local conductance as a function of RF frequency at different fields and temperatures for two different ‘pairs’ of peaks. (cf. Figure 4.). No substantial difference in cut-off frequency is observed in the range of available temperatures and fields.

European Research Council Starting Independent Researcher (NANO-GRAPHENE 256965) and Synergy Grants; an ANR Blanc grant (MASH) from the French Agence Nationale de Recherche; and the Netherlands Organization for Scientific Research (NWO/OCW).

I. SUPPLEMENTARY INFORMATION

A. Injecting from J1

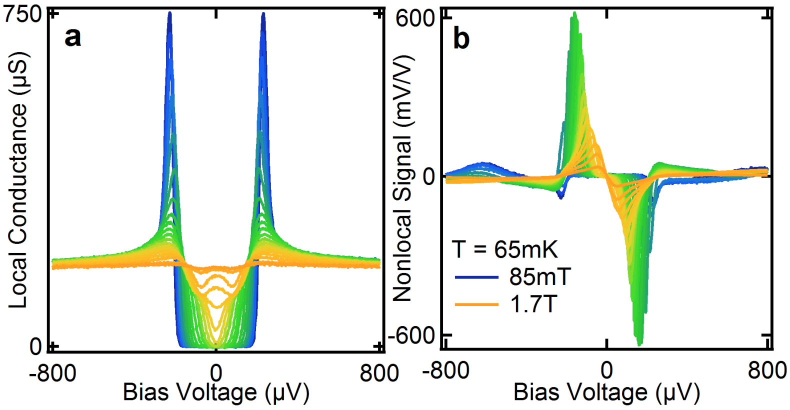

FIG. 6: (a) Local conductance dI/dV_{DC} measured at J1, over a range of magnetic fields. (b) Corresponding differential nonlocal signal dV_{NL}/dV_{DC} measured at J3.

As noted in the main text, all the data shown were with quasiparticles injection into the superconductor at the junction J2 and detection at J3.

In Figure 6, we show data from the same device, with injection across J1 instead and detection still at J3. The measured local conductance, proportional to the density of states (DOS) in the superconductor (S), shows that the latter is less depaired at J1 than at J2 (compare Figure 6a to Figure 2a of the main text). This is because the main cause of depairing is stray fields from the cobalt electrode at J3, which can have a component perpendicular to the plane of the device. As the distance J1–J3 is larger than J2–J3, the S DOS is less depaired at J1 compared to J2. Thus, the Zeeman splitting of the DOS at high magnetic fields is also more apparent in these data. The nonlocal differential signal can also be seen to be larger (Figure 6b) (To a very rough first approximation, it is proportional to the derivative of the injection DOS [19]. While this is no longer true in this case, generally the ‘sharper’ the injection and detection DOS, the larger the nonlocal signal.)

N.B. The data shown in Figure 6a are the in-phase component of the differential nonlocal signal. As J3 is very resistive ($e\mu_s \sim \Delta/2$ at most and the density of states at J3 highly nonlinear, see Figure 9), the out-of-phase component can be of comparable amplitude; however, we checked that the in-phase signal is the same as the numerical derivative (with respect to the bias voltage) of the DC nonlocal signal to an overall factor of $\lesssim 2$.

B. Ruling out Thermoelectric Effects

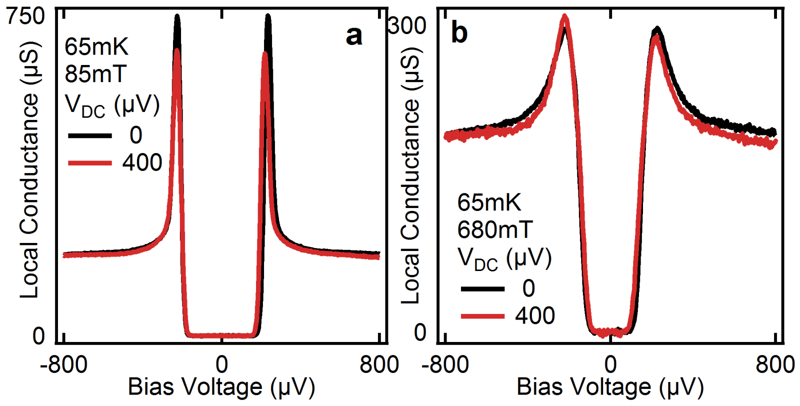

FIG. 7: Local conductance dI/dV_{DC} at J1 at two different magnetic fields, with and without a large voltage bias on J2.

To rule out thermoelectric effects [25], we measured the local conductance at J1 while biasing J2 very much above the superconducting gap, thus creating large spin and charge imbalances at J1. We compare this to the same measurement when J2 is not biased. This test was done at two different magnetic fields and the results shown in Figure 7. It can be seen that biasing J2 does not do much to broaden the DOS at J1. Thus, thermoelectric effects are negligible in the results presented in this Letter.

Biasing J2 does however induce a slight narrowing of the gap at J1 as well as an asymmetry in the amplitudes of the BCS coherence peaks. These effects will be discussed in a separate publication.

C. Very High-Frequency Injection

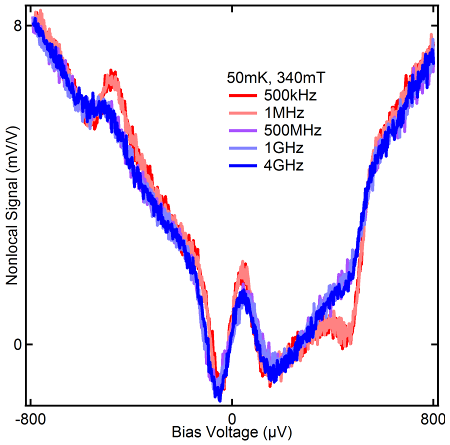

FIG. 8: Differential nonlocal signal dV_{NL}/dV_{DC} as a function of V_{DC} at different f_{RF}. These data are from a device which is different from, but nominally identical to, the one from which data are shown in the main text.

To verify that the behaviour we observe in the frequency domain is indeed a cut-off rather than e.g. an oscillatory phenomenon, we also performed measurements at RF injection frequencies very much above the observed cut-off. Figure 8 shows the differential nonlocal signal dV_{NL}/dV_{DC} as a function of DC bias voltage V_{DC} at several RF injection frequencies (and at constant amplitude V_{RF}). Between 500kHz and 500MHz, similar to data shown in the main text, the amplitudes of the classically-rectified spin imbalance peaks diminishes. However, there is no further change in the signal at higher frequencies, in agreement with our theoretical expectation of a cut-off.

D. Cobalt Polarisation

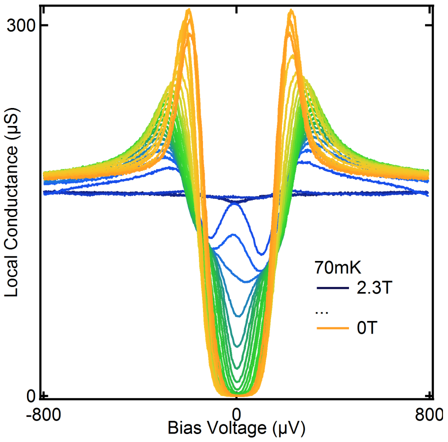

FIG. 9: Local conductance measured at J3, over a range of magnetic fields.

In order to estimate the polarisation, P of the cobalt electrode and to determine its sign, we measure local conductance spectra at J3 as a function of magnetic field. (Figure 9) From the asymmetry of the inner Zeeman-split peaks, it is already possible to see that the polarisation is negative, which is to say in the direction opposite to that of the applied field (cf. Ref. [26]). This is consistent with the work of Münzenberg and Moodera [27], indicating that the polarisation of electrons injected from cobalt across a thin Al_2O_3 barrier can be negative. From the heights of the inner 'shoulders' we estimate P to be 7–10% [26, 28], consistent with results from previous work on similar samples [19].

[1] J. R. Schrieffer and D. M. Ginsberg, Physical Review Letters **8**, 207 (1962).

[2] A. Rothwarf and B. N. Taylor, Physical Review Letters **19**, 27 (1967).

[3] C. S. Owen and D. J. Scalapino, Physical Review Letters **28**, 1559 (1972).

[4] J.-J. Chang and D. J. Scalapino, Journal of Low Temperature Physics **31**, 1 (1978).

[5] T. P. Devereaux and D. Belitz, Physical Review B **44**, 4587 (1991).

[6] M. Reizer, Physical Review B **61**, 7108 (2000).

[7] S. M. Quinlan, D. J. Scalapino, and N. Bulut, Physical Review B **49**, 1470 (1994).

[8] Y. Yafet, Physics Letters A **98**, 287 (1983).

[9] R. D. Averitt and A. J. Taylor, Journal of Physics: Condensed Matter **14**, R1357 (2002).

[10] J. Demsar, B. Podobnik, V. V. Kabanov, T. Wolf, and D. Mihailovic, Physical Review Letters **82**, 4918 (1999).

[11] N. Gedik, J. Orenstein, R. Liang, D. A. Bonn, and W. N. Hardy, Science **300**, 1410 (2003).

[12] I. Madan, T. Kurosawa, Y. Toda, M. Oda, T. Mertelj, P. Kusar, and D. Mihailovic, Scientific Reports **4** (2014).

[13] M. Johnson, Physical Review Letters **67**, 374 (1991).

[14] G. L. Carr, R. P. S. M. Lobo, J. LaVeigne, D. H. Reitze, and D. B. Tanner, Physical Review Letters **85**, 3001 (2000).

[15] R. Peters and H. Meissner, Physical Review Letters **30**, 965 (1973).

[16] P. Hu, R. C. Dynes, and V. Narayanamurti, Physical Review B **10**, 2786 (1974).

[17] J. Clarke, Physical Review Letters **28**, 1363 (1972).

[18] M. Tinkham and J. Clarke, Physical Review Letters **28**, 1366 (1972).

[19] C. H. L. Quay, D. Chevallier, C. Bena, and M. Aprili, Nature Physics **9**, 84 (2013).

[20] F. Hübler, M. J. Wolf, D. Beckmann, and H. v. Loehneysen, Physical Review Letters **109**, 207001 (2012).

[21] M. J. Wolf, F. Hübler, S. Kolenda, H. v. Loehneysen, and D. Beckmann, Physical Review B **87**, 024517 (2013).

[22] H. L. Zhao and S. Hershfield, Physical Review B **52**, 3632 (1995).

[23] S. Takahashi, H. Imamura, and S. Maekawa, Physical Review Letters **82**, 3911 (1999).

[24] D. Chevallier, C. Dutreix, M. Guigou, C. H. L. Quay, C. Bena, and M. Aprili, submitted to Physical Review B (2014).

[25] J. S. Meyer and M. Houzet, private communication (2014).

[26] P. M. Tedrow and R. Meservey, Physical Review Letters **26**, 192 (1971).

[27] M. Münzenberg and J. S. Moodera, Physical Review B **70**, 060402 (2004).

[28] D. Paraskevopoulos, R. Meservey, and P. M. Tedrow, Physical Review B **16**, 4907 (1977).

Conclusion

The first part of this thesis mainly focuses on multi-band models, based on the honeycomb lattice. The low-energy physics of graphene is ruled by chiral massless Dirac electrons that refer to two Dirac cones in the spectrum. Even if these two cones appear to be protected by the inversion and the time-reversal symmetries, they are characterised by two opposite winding numbers, which, in principle, allows a topological Dirac-cone merging transition from a semimetallic phase toward an insulating one.

The main idea of the second chapter has been to describe this transition through the impurity scattering. A localised impurity in the honeycomb lattice induces Friedel oscillations in the local density of states. If these $2k_F$-wavevector modulations are directly related to the existence of a Fermi surface and its nesting properties, they turn out to be sensitive to the pseudospin and the chiral nature of the massless Dirac electrons. When there are two Dirac cones in the semimetallic phase, as well as when the spectrum is parabolic in the insulating one, a localised impurity induces Friedel oscillations that qualitatively decay as $1/r$ with the distance to the impurity on every sublattice. However, the chirality defined in the case of massless Dirac electrons requires the oscillations on the sublattice A and those on the sublattice B to be in antiphase. Therefore, the $1/r$ decaying signals cancel each other when averaging over a unit cell, reducing the quantum interferences to a $1/r^2$ decay. A similar feature arises right at the Dirac-cone merging transition, where the spectrum is quadratic in one direction, albeit linear in the orthogonal one. Along this latter indeed, a chirality can still be defined, and the $1/\sqrt{r}$ decaying Friedel oscillations are in antiphase on the two sublattices, resulting in a $1/r$ decay when averaging over the unit cell. Therefore the Friedel oscillations, which behave differently as a function of the phase the system belongs to, can be considered as a real space signature of the Dirac-cone merging transition. Although this transition is not reachable in graphene, it may be achieved in organic layered compound α-(BEDT-TTF)$_2$I$_3$ under hydrostatic pressure [138, 139].

If the impurity consists of a missing atom on one of the two sublattices, it induces a zero-energy impurity wavefunction with non-null components only on the other sublattice. The chiral nature of electrons does not make sense at such an energy, but the two sublattices are now decoupled, which makes possible the evaluation of the impurity state. Remarkably, the non-null components of the wavefunction are given by the binomial coefficients and design the Pascal's triangle, as soon as the system reaches the insulating phase. Moreover, the evaluation of the impurity states reveals a $1/r$ decay in the semimetallic phase when there are two conical points in the spectrum. Right at the Dirac-cone merging transition, the wavefunction decays as $1/\sqrt{r}$, whereas it exhibits an exponential decay in the insulating phase. Thus, a vacancy-induced zero-energy state also enables the characterisation of the transition in real space, which would be particularly relevant in the context of artificial lattices experiments [49, 70].

In the third chapter, the formation of robust boundary modes in three systems has been discussed, as a function of the topology of their tight-binding band structure.
First, a one-dimensional two-band model, originally known as Shockley model, has been introduced and then generalised to the case of arbitrary distant neighbour processes. Under the sublattice symmetry, a winding number characterises the topology of the band structure. This topological invariant has been related to the number of zero-energy edge states that are localised at a boundary with the vacuum, which establishes a bulk-edge correspondence. If the absolute value of the winding number leads to be the number of edge states, its sign refers to the sublattice on which these evanescent modes are localised. This has been exemplified through the study of a dimerised chain when allowing third nearest-neighbour hopping processes. The topological aspect of the prediction of the zero-energy boundary modes makes them robust against disorder, as long as it does not break the chiral symmetry.
Second, it is shown how the emergence of boundary modes in two-dimensional systems that have a nodal dispersion relation, like graphene, can be topologically characterised through a dimensional reduction. In the case of graphene nanoribbons, this dimensional reduction leads to an effective mapping onto the generalised Shockley model. The effect of a localised impurity that breaks the translational invariance is investigated in a zigzag graphene nanoribbon, where the edge states appear to be robust against this kind of disorder.
Third, the topological characterisation of a two-dimensional eight-band model has been investigated. It describes electrons in a honeycomb lattice with spin-singlet superconductivity and Rashba spin-orbit coupling, when a magnetic field breaks the time-reversal symmetry. Although the spectrum cannot be obtained exactly, it is possible to reach the exact topological criterion that describes the emergence of Majorana boundary modes in the system. Indeed the Chern number that characterises the topology of the band structure has been evaluated from the band-parity defined at the time-reversal invariant points. Therefore,

Majorana modes are predicted in doped and strained nanoribbons, which appears to be experimentally relevant in s-wave superfluids of ultracold fermionic atoms [109]. Contrary to what is mainly considered in the literature, it turns out that their existence explicitly depends on the Rashba spin-orbit coupling, due to the diatomic pattern of the honeycomb lattice.

The second part of the thesis focuses on chargeless spin-imbalance occurring in out-of-equilibrium superconductors. The fourth chapter has addressed a model to fit experimental data obtained in the frequency domain and to extract the spin-relaxation time. The spin current injected in the superconductor has been obtained from the Fermi's golden rule taking into account all the quasiparticle tunneling processes between the superconductor and the normal metal. This current has then been related to the spin accumulation via a diffusion equation of motion that has to be solved self-consistently, in order to obtain the time dependence of the measured voltage and spin accumulation, as a function of the applied AC voltage. When increasing the frequency, a saturation arises with respect to the measured voltage. It qualitatively refers to the inverse of the spin-relaxation time that appears to be of the order of a few nanoseconds.

References

[1] K. S. Novoselov, A. K. Geim, S. Morozov, D. Jiang, Y. Zhang, S. Dubonos, I. Grigorieva, and A. Firsov, "Electric field effect in atomically thin carbon films," *science*, vol. 306, no. 5696, pp. 666–669, 2004.

[2] K. Novoselov, A. K. Geim, S. Morozov, D. Jiang, M. K. I. Grigorieva, S. Dubonos, and A. Firsov, "Two-dimensional gas of massless Dirac fermions in graphene," *nature*, vol. 438, no. 7065, pp. 197–200, 2005.

[3] Y. Zhang, Y.-W. Tan, H. L. Stormer, and P. Kim, "Experimental observation of the quantum Hall effect and Berry's phase in graphene," *Nature*, vol. 438, no. 7065, pp. 201–204, 2005.

[4] A. F. Young and P. Kim, "Quantum interference and Klein tunnelling in graphene heterojunctions," *Nature Physics*, vol. 5, no. 3, pp. 222–226, 2009.

[5] O. Klein, "Die reflexion von elektronen an einem potentialsprung nach der relativistischen dynamik von Dirac," *Zeitschrift für Physik*, vol. 53, no. 3-4, pp. 157–165, 1929.

[6] T. Ando, T. Nakanishi, and R. Saito, "Berry's phase and absence of back scattering in carbon nanotubes," *Journal of the Physical Society of Japan*, vol. 67, no. 8, pp. 2857–2862, 1998.

[7] M. Fujita, K. Wakabayashi, K. Nakada, and K. Kusakabe, "Peculiar localized state at zigzag graphite edge," *Journal of the Physical Society of Japan*, vol. 65, no. 7, pp. 1920–1923, 1996.

[8] A. Akhmerov and C. Beenakker, "Boundary conditions for Dirac fermions on a terminated honeycomb lattice," *Physical Review B*, vol. 77, no. 8, p. 085423, 2008.

[9] S. Ryu, A. P. Schnyder, A. Furusaki, and A. W. Ludwig, "Topological insulators and superconductors: tenfold way and dimensional hierarchy," *New Journal of Physics*, vol. 12, no. 6, p. 065010, 2010.

[10] K. v. Klitzing, G. Dorda, and M. Pepper, "New method for high-accuracy determination of the fine-structure constant based on quantized Hall resistance," *Physical Review Letters*, vol. 45, no. 6, p. 494, 1980.

[11] D. Thouless, M. Kohmoto, M. Nightingale, and M. Den Nijs, "Quantized Hall conductance in a two-dimensional periodic potential," *Physical Review Letters*, vol. 49, no. 6, p. 405, 1982.

[12] M. V. Berry, “Quantal phase factors accompanying adiabatic changes,” *Proceedings of the Royal Society of London. A. Mathematical and Physical Sciences*, vol. 392, no. 1802, pp. 45–57, 1984.

[13] F. D. M. Haldane, “Model for a quantum Hall effect without Landau levels: Condensed-matter realization of the" parity anomaly",” *Physical Review Letters*, vol. 61, no. 18, p. 2015, 1988.

[14] A. Y. Kitaev, “6. QUANTUM COMPUTING: Unpaired Majorana fermions in quantum wires,” *Physics Uspekhi*, vol. 44, p. 131, Oct. 2001.

[15] C. L. Kane and E. J. Mele, “Quantum spin Hall effect in graphene,” *Phys. Rev. Lett.*, vol. 95, p. 226801, Nov 2005.

[16] I. Lifshitz and M. I. Kaganov, “Some problems of the electron theory of metals i. classical and quantum mechanics of electrons in metals,” *Physics-Uspekhi*, vol. 2, no. 6, pp. 831–855, 1960.

[17] V. V. Cheianov and V. I. Fal’ko, “Friedel oscillations, impurity scattering, and temperature dependence of resistivity in graphene,” *Phys. Rev. Lett.*, vol. 97, p. 226801, Nov 2006.

[18] J. Friedel, “Electronic structure of primary solid solutions in metals,” *Advances in Physics*, vol. 3, no. 12, pp. 446–507, 1954.

[19] C. Dutreix, L. Bilteanu, A. Jagannathan, and C. Bena, “Friedel oscillations at the Dirac cone merging point in anisotropic graphene and graphenelike materials,” *Physical Review B*, vol. 87, no. 24, p. 245413, 2013.

[20] W. Shockley, “On the surface states associated with a periodic potential,” *Physical review*, vol. 56, no. 4, p. 317, 1939.

[21] W. Su, J. Schrieffer, and A. J. Heeger, “Solitons in polyacetylene,” *Physical Review Letters*, vol. 42, no. 25, p. 1698, 1979.

[22] S. S. Pershoguba and V. M. Yakovenko, “Shockley model description of surface states in topological insulators,” *Physical Review B*, vol. 86, no. 7, p. 075304, 2012.

[23] L. Bilteanu, C. Dutreix, A. Jagannathan, and C. Bena, “Interplay between edge states and simple bulk defects in graphene nanoribbons,” *The European Physical Journal B*, vol. 86, no. 5, pp. 1–12, 2013.

[24] M. Sato, Y. Takahashi, and S. Fujimoto, “Non-abelian topological orders and Majorana fermions in spin-singlet superconductors,” *Phys. Rev. B*, vol. 82, p. 134521, Oct 2010.

[25] C. Dutreix, M. Guigou, D. Chevallier, and C. Bena, “Majorana fermions in honeycomb lattices,” *The European Physical Journal B*, vol. 87, no. 12, pp. 1–7, Springer.

[26] C. Quay, D. Chevallier, C. Bena, and M. Aprili, “Spin imbalance and spin-charge separation in a mesoscopic superconductor,” *Nature Physics*, vol. 9, no. 2, pp. 84–88, 2013.

[27] C. H. L. Quay, C. Dutreix, D. Chevallier, C. Bena, and M. Aprili, “Frequency domain measurement of quasiparticle spin lifetime in superconductors,” *submitted to PRL*, 2014.

[28] D. Chevallier, C. Dutreix, M. Guigou, C. Quay, M. Aprili, and C. Bena, “Frequency-dependent spin accumulation in out-of-equilibrium mesoscopic superconductors,” *arXiv preprint arXiv:1408.1833*, 2014.

[29] V. Klechkovskii, “Justification of the rule for successive filling of (n+ l) groups,” *SOVIET PHYSICS JETP-USSR*, vol. 14, no. 2, pp. 334–335, 1962.

[30] N. D. Mermin and H. Wagner, “Absence of ferromagnetism or antiferromagnetism in one-or two-dimensional isotropic heisenberg models,” *Physical Review Letters*, vol. 17, no. 22, p. 1133, 1966.

[31] P. R. Wallace, “The band theory of graphite,” *Physical Review*, vol. 71, no. 9, p. 622, 1947.

[32] D. Sticlet and F. Piéchon, “Distant-neighbor hopping in graphene and Haldane models,” *Physical Review B*, vol. 87, no. 11, p. 115402, 2013.

[33] S. Ryu and Y. Hatsugai, “Topological origin of zero-energy edge states in particle-hole symmetric systems,” *Phys. Rev. Lett.*, vol. 89, p. 077002, Jul 2002.

[34] P. Delplace, D. Ullmo, and G. Montambaux, “Zak phase and the existence of edge states in graphene,” *Physical Review B*, vol. 84, no. 19, p. 195452, 2011.

[35] G. Mikitik and Y. V. Sharlai, “Manifestation of Berry’s phase in metal physics,” *Physical Review Letters*, vol. 82, no. 10, pp. 2147–2150, 1999.

[36] J.-N. Fuchs, F. Piéchon, M. Goerbig, and G. Montambaux, “Topological Berry phase and semiclassical quantization of cyclotron orbits for two dimensional electrons in coupled band models,” *The European Physical Journal B-Condensed Matter and Complex Systems*, vol. 77, no. 3, pp. 351–362, 2010.

[37] M. Katsnelson, K. Novoselov, and A. Geim, “Chiral tunnelling and the Klein paradox in graphene,” *Nature Physics*, vol. 2, no. 9, pp. 620–625, 2006.

[38] S. Reich, J. Maultzsch, C. Thomsen, and P. Ordejon, “Tight-binding description of graphene,” *Physical Review B*, vol. 66, no. 3, p. 035412, 2002.

[39] C. Bena and G. Montambaux, “Remarks on the tight-binding model of graphene,” *New Journal of Physics*, vol. 11, no. 9, p. 095003, 2009.

[40] P. E. Allain and J.-N. Fuchs, “Klein tunneling in graphene: optics with massless electrons,” *The European Physical Journal B-Condensed Matter and Complex Systems*, vol. 83, no. 3, pp. 301–317, 2011.

[41] J. L. Mañes, F. Guinea, and M. A. Vozmediano, “Existence and topological stability of fermi points in multilayered graphene,” *Physical Review B*, vol. 75, no. 15, p. 155424, 2007.

[42] Y. Hatsugai, "Topological aspect of graphene physics," in *Journal of Physics: Conference Series*, vol. 334, p. 012004, IOP Publishing, 2011.

[43] Y. Hasegawa, R. Konno, H. Nakano, and M. Kohmoto, "Zero modes of tight-binding electrons on the honeycomb lattice," *Phys. Rev. B*, vol. 74, p. 033413, Jul 2006.

[44] G. Montambaux, F. Piéchon, J.-N. Fuchs, and M. Goerbig, "A universal hamiltonian for motion and merging of Dirac points in a two-dimensional crystal," *The European Physical Journal B-Condensed Matter and Complex Systems*, vol. 72, no. 4, pp. 509–520, 2009.

[45] P. Dietl, F. Piéchon, and G. Montambaux, "New magnetic field dependence of Landau levels in a graphenelike structure," *Phys. Rev. Lett.*, vol. 100, p. 236405, Jun 2008.

[46] F. Liu, P. Ming, and J. Li, "Ab initio calculation of ideal strength and phonon instability of graphene under tension," *Physical Review B*, vol. 76, no. 6, p. 064120, 2007.

[47] L. Tarruell, D. Greif, T. Uehlinger, G. Jotzu, and T. Esslinger, "Creating, moving and merging Dirac points with a Fermi gas in a tunable honeycomb lattice," *Nature*, vol. 483, no. 7389, pp. 302–305, 2012.

[48] L.-K. Lim, J.-N. Fuchs, and G. Montambaux, "Bloch-Zener oscillations across a merging transition of Dirac points," *Physical review letters*, vol. 108, no. 17, p. 175303, 2012.

[49] M. Bellec, U. Kuhl, G. Montambaux, and F. Mortessagne, "Topological transition of Dirac points in a microwave experiment," *Physical review letters*, vol. 110, no. 3, p. 033902, 2013.

[50] H. Yukawa, "On the interaction of elementary particles. i," *Progress of Theoretical Physics Supplement*, vol. 1, pp. 1–10, 1955.

[51] M. A. Ruderman and C. Kittel, "Indirect exchange coupling of nuclear magnetic moments by conduction electrons," *Physical Review*, vol. 96, no. 1, p. 99, 1954.

[52] G. Binnig and H. Rohrer, "Scanning tunneling microscopy—from birth to adolescence," *Reviews of Modern Physics*, vol. 59, no. 3, pp. 615–625, 1987.

[53] H. Hankel, *Die Euler'schen integrale bei unbeschränkter variabilität der arguments*. Leipzig., 1863.

[54] S. K. Adhikari, "Quantum scattering in two dimensions," *American Journal of Physics*, vol. 54, no. 4, pp. 362–367, 1986.

[55] M. Crommie, C. Lutz, and D. Eigler, "Imaging standing waves in a two-dimensional electron gas," *Nature*, 1993.

[56] S. Hasegawa, X. Tong, C.-S. Jiang, Y. Nakajima, and T. Nagao, "Electrical conduction via surface-state bands," *Surface science*, vol. 386, no. 1, pp. 322–327, 1997.

[57] P. Sprunger, L. Petersen, E. Plummer, E. Lægsgaard, and F. Besenbacher, "Giant friedel oscillations on the beryllium (0001) surface," *Science*, vol. 275, no. 5307, pp. 1764–1767, 1997.

[58] L. Simon, C. Bena, F. Vonau, D. Aubel, H. Nasrallah, M. Habar, and J. Peruchetti, "Symmetry of standing waves generated by a point defect in epitaxial graphene," *The European Physical Journal B*, vol. 69, no. 3, pp. 351–355, 2009.

[59] I. Brihuega, P. Mallet, C. Bena, S. Bose, C. Michaelis, L. Vitali, F. Varchon, L. Magaud, K. Kern, and J.-Y. Veuillen, "Quasiparticle chirality in epitaxial graphene probed at the nanometer scale," *Physical review letters*, vol. 101, no. 20, p. 206802, 2008.

[60] C. Bena, "Effect of a single localized impurity on the local density of states in monolayer and bilayer graphene," *Physical review letters*, vol. 100, no. 7, p. 076601, 2008.

[61] T. Wehling, A. Balatsky, M. Katsnelson, A. Lichtenstein, K. Scharnberg, and R. Wiesendanger, "Local electronic signatures of impurity states in graphene," *Physical Review B*, vol. 75, no. 12, p. 125425, 2007.

[62] V. M. Pereira, F. Guinea, J. M. B. Lopes dos Santos, N. M. R. Peres, and A. H. Castro Neto, "Disorder induced localized states in graphene," *Phys. Rev. Lett.*, vol. 96, p. 036801, Jan 2006.

[63] V. A. Gubanov, A. I. Liechtenstein, and A. V. Postnikov, *Magnetism and the electronic structure of crystals*. Springer, 1992.

[64] N. Peres, F. Guinea, and A. C. Neto, "Electronic properties of disordered two-dimensional carbon," *Physical Review B*, vol. 73, no. 12, p. 125411, 2006.

[65] T. Wehling, S. Yuan, A. Lichtenstein, A. Geim, and M. Katsnelson, "Resonant scattering by realistic impurities in graphene," *Physical review letters*, vol. 105, no. 5, p. 056802, 2010.

[66] J.-H. Chen, W. Cullen, C. Jang, M. Fuhrer, and E. Williams, "Defect scattering in graphene," *Physical review letters*, vol. 102, no. 23, p. 236805, 2009.

[67] M. Inui, S. Trugman, and E. Abrahams, "Unusual properties of midband states in systems with off-diagonal disorder," *Physical Review B*, vol. 49, no. 5, p. 3190, 1994.

[68] B. Sutherland, "Localization of electronic wave functions due to local topology," *Phys. Rev. B*, vol. 34, pp. 5208–5211, Oct 1986.

[69] E. H. Lieb, "Two theorems on the hubbard model," in *Condensed Matter Physics and Exactly Soluble Models*, pp. 55–58, Springer, 2004.

[70] M. Bellec, U. Kuhl, G. Montambaux, and F. Mortessagne, "Manipulation of edge states in microwave artificial graphene," *arXiv preprint arXiv:1406.6409*, 2014.

[71] J. Luck and Y. Avishai, "Unusual electronic properties of clean and disordered zigzag graphene nanoribbons," *arXiv preprint arXiv:1406.3924*, 2014.

[72] L. Landau, "Zur theorie der phasenumwandlungen ii," *Phys. Z. Sowjetunion*, vol. 11, pp. 26–35, 1937.

[73] R. B. Laughlin, "Quantized Hall conductivity in two dimensions," *Physical Review B*, vol. 23, no. 10, p. 5632, 1981.

[74] X.-G. Wen, "Topological orders in rigid states," *International Journal of Modern Physics B*, vol. 4, no. 02, pp. 239–271, 1990.

[75] X.-G. Wen, F. Wilczek, and A. Zee, "Chiral spin states and superconductivity," *Physical Review B*, vol. 39, no. 16, p. 11413, 1989.

[76] R. B. Laughlin, "Anomalous quantum Hall effect: an incompressible quantum fluid with fractionally charged excitations," *Physical Review Letters*, vol. 50, no. 18, pp. 1395–1398, 1983.

[77] A. P. Schnyder, S. Ryu, A. Furusaki, and A. W. Ludwig, "Classification of topological insulators and superconductors in three spatial dimensions," *Physical Review B*, vol. 78, no. 19, p. 195125, 2008.

[78] I. Tamm, "On the possible bound states of electrons on a crystal surface," *Phys. Z. Sowjetunion*, vol. 1, pp. 733–735, 1932.

[79] M. Franz and L. Molenkamp, *Topological Insulators*, vol. 6. Elsevier, 2013.

[80] R. S. Mong and V. Shivamoggi, "Edge states and the bulk-boundary correspondence in Dirac hamiltonians," *Physical Review B*, vol. 83, no. 12, p. 125109, 2011.

[81] A. Altland and M. R. Zirnbauer, "Nonstandard symmetry classes in mesoscopic normal-superconducting hybrid structures," *Physical Review B*, vol. 55, no. 2, p. 1142, 1997.

[82] E. P. Wigner, "On the distribution of the roots of certain symmetric matrices," *Annals of Mathematics*, pp. 325–327, 1958.

[83] F. J. Dyson, "Statistical theory of the energy levels of complex systems. i," *Journal of Mathematical Physics*, vol. 3, no. 1, pp. 140–156, 1962.

[84] A. Kitaev, "Periodic table for topological insulators and superconductors," *arXiv preprint arXiv:0901.2686*, 2009.

[85] C. Kane and E. Mele, "z_2 topological order and the quantum spin Hall effect," *Phys. Rev. Lett.*, vol. 95, p. 146802, 2005.

[86] E. Majorana, "Teoria simmetrica dell'elettrone e del positrone," *Il Nuovo Cimento*, vol. 14, pp. 171–184, 1937.

[87] M. H. Freedman, A. Kitaev, M. J. Larsen, and Z. Wang, "Topological quantum computation," *Bull. Amer. Math. Soc. (N.S.)*, vol. 40, no. 1, pp. 31–38, 2003. Mathematical challenges of the 21st century (Los Angeles, CA, 2000).

[88] R. M. Lutchyn, J. D. Sau, and S. Das Sarma, "Majorana fermions and a topological phase transition in semiconductor-superconductor heterostructures," *Phys. Rev. Lett.*, vol. 105, p. 077001, Aug 2010.

[89] J. Alicea, “Majorana fermions in a tunable semiconductor device,” *Phys. Rev. B*, vol. 81, p. 125318, Mar 2010.

[90] P. Ghosh, J. D. Sau, S. Tewari, and S. Das Sarma, “Non-abelian topological order in noncentrosymmetric superconductors with broken time-reversal symmetry,” *Phys. Rev. B*, vol. 82, p. 184525, Nov 2010.

[91] G. E. Volovik, *The universe in a helium droplet*, vol. 117. Oxford University Press New York, 2009.

[92] V. Gurarie, “Single-particle green’s functions and interacting topological insulators,” *Physical Review B*, vol. 83, no. 8, p. 085426, 2011.

[93] A. M. Essin and V. Gurarie, “Bulk-boundary correspondence of topological insulators from their respective green’s functions,” *Physical Review B*, vol. 84, no. 12, p. 125132, 2011.

[94] M. Sato, “Nodal structure of superconductors with time-reversal invariance and z 2 topological number,” *Physical Review B*, vol. 73, no. 21, p. 214502, 2006.

[95] M. Sato, Y. Tanaka, K. Yada, and T. Yokoyama, “Topology of andreev bound states with flat dispersion,” *Phys. Rev. B*, vol. 83, p. 224511, Jun 2011.

[96] P. A. Dirac, “The quantum theory of the electron,” *Proceedings of the Royal Society of London. Series A, Containing Papers of a Mathematical and Physical Character*, pp. 610–624, 1928.

[97] C. D. Anderson, “The positive electron,” *Physical Review*, vol. 43, no. 6, p. 491, 1933.

[98] P. B. Pal, “Dirac, Majorana, and Weyl fermions,” *American Journal of Physics*, vol. 79, no. 5, pp. 485–498, 2011.

[99] C. Caroli, P. De Gennes, and J. Matricon, “Bound fermion states on a vortex line in a type ii superconductor,” *Physics Letters*, vol. 9, no. 4, pp. 307–309, 1964.

[100] N. Read and D. Green, “Paired states of fermions in two dimensions with breaking of parity and time-reversal symmetries and the fractional quantum Hall effect,” *Physical Review B*, vol. 61, no. 15, p. 10267, 2000.

[101] S. Tewari and J. D. Sau, “Topological invariants for spin-orbit coupled superconductor nanowires,” *Physical review letters*, vol. 109, no. 15, p. 150408, 2012.

[102] Y. Niu, S. B. Chung, C.-H. Hsu, I. Mandal, S. Raghu, and S. Chakravarty, “Majorana zero modes in a quantum ising chain with longer-ranged interactions,” *Physical Review B*, vol. 85, no. 3, p. 035110, 2012.

[103] D. Sticlet, C. Bena, and P. Simon, “Josephson effect in superconducting wires supporting multiple Majorana edge states,” *Physical Review B*, vol. 87, no. 10, p. 104509, 2013.

[104] S. D. Sarma, C. Nayak, and S. Tewari, “Proposal to stabilize and detect half-quantum vortices in strontium ruthenate thin films: Non-abelian braiding statistics of vortices in a p x+ i p y superconductor,” *Physical Review B*, vol. 73, no. 22, p. 220502, 2006.

[105] V. Gurarie, L. Radzihovsky, and A. Andreev, “Quantum phase transitions across a p-wave feshbach resonance,” *Physical review letters*, vol. 94, no. 23, p. 230403, 2005.

[106] L. Fu and C. L. Kane, “Superconducting proximity effect and Majorana fermions at the surface of a topological insulator,” *Physical Review Letters*, vol. 100, no. 9, p. 096407, 2008.

[107] J. D. Sau, R. M. Lutchyn, S. Tewari, and S. D. Sarma, “Generic new platform for topological quantum computation using semiconductor heterostructures,” *Physical review letters*, vol. 104, no. 4, p. 040502, 2010.

[108] Y. Oreg, G. Refael, and F. von Oppen, “Helical liquids and Majorana bound states in quantum wires,” *Phys. Rev. Lett.*, vol. 105, p. 177002, Oct 2010.

[109] M. Sato, Y. Takahashi, and S. Fujimoto, “Non-abelian topological order in s-wave superfluids of ultracold fermionic atoms,” *Physical review letters*, vol. 103, no. 2, p. 020401, 2009.

[110] L. Fu and C. L. Kane, “Topological insulators with inversion symmetry,” *Phys. Rev. B*, vol. 76, p. 045302, Jul 2007.

[111] A. M. Black-Schaffer and S. Doniach, “Resonating valence bonds and mean-field d-wave superconductivity in graphite,” *Physical Review B*, vol. 75, no. 13, p. 134512, 2007.

[112] B. Uchoa and A. H. Castro Neto, “Superconducting states of pure and doped graphene,” *Phys. Rev. Lett.*, vol. 98, p. 146801, Apr 2007.

[113] A. M. Black-Schaffer, “Edge properties and Majorana fermions in the proposed chiral d-wave superconducting state of doped graphene,” *Physical review letters*, vol. 109, no. 19, p. 197001, 2012.

[114] J. Hu, J. Alicea, R. Wu, and M. Franz, “Giant topological insulator gap in graphene with 5 d adatoms,” *Physical review letters*, vol. 109, no. 26, p. 266801, 2012.

[115] M. Sato, “Topological properties of spin-triplet superconductors and fermi surface topology in the normal state,” *Phys. Rev. B*, vol. 79, p. 214526, Jun 2009.

[116] M. Sato, “Topological odd-parity superconductors,” *Phys. Rev. B*, vol. 81, p. 220504, Jun 2010.

[117] J. L. McChesney, A. Bostwick, T. Ohta, T. Seyller, K. Horn, J. González, and E. Rotenberg, “Extended van hove singularity and superconducting instability in doped graphene,” *Physical review letters*, vol. 104, no. 13, p. 136803, 2010.

[118] C. Lee, X. Wei, J. W. Kysar, and J. Hone, “Measurement of the elastic properties and intrinsic strength of monolayer graphene,” *science*, vol. 321, no. 5887, pp. 385–388, 2008.

[119] F. Hübler, M. Wolf, D. Beckmann, and H. v. Löhneysen, “Long-range spin-polarized quasiparticle transport in mesoscopic al superconductors with a zeeman splitting,” *Physical review letters*, vol. 109, no. 20, p. 207001, 2012.

[120] M. Wolf, F. Hübler, S. Kolenda, H. v. Löhneysen, and D. Beckmann, “Spin injection from a normal metal into a mesoscopic superconductor,” *Physical Review B*, vol. 87, no. 2, p. 024517, 2013.

[121] J. Clarke, “Experimental observation of pair-quasiparticle potential difference in nonequilibrium superconductors,” *Physical Review Letters*, vol. 28, no. 21, p. 1363, 1972.

[122] A. Aronov, “Spin injection in metals and polarization of nuclei,” *Jetp Lett*, vol. 24, no. 1, pp. 32–34, 1976.

[123] M. Johnson, “Spin coupled resistance observed in ferromagnet-superconductor-ferromagnet trilayers,” *Applied physics letters*, vol. 65, no. 11, pp. 1460–1462, 1994.

[124] C. Chen, W. Kuo, D. Chung, J. Shyu, and C.-S. Wu, “Evidence for suppression of superconductivity by spin imbalance in co-al-co single-electron transistors,” *Physical review letters*, vol. 88, no. 4, p. 047004, 2002.

[125] P. Cadden-Zimansky, Z. Jiang, and V. Chandrasekhar, “Charge imbalance, crossed andreev reflection and elastic co-tunnelling in ferromagnet/superconductor/normal-metal structures,” *New Journal of Physics*, vol. 9, no. 5, p. 116, 2007.

[126] H. Yang, S.-H. Yang, S. Takahashi, S. Maekawa, and S. S. Parkin, “Extremely long quasiparticle spin lifetimes in superconducting aluminium using mgo tunnel spin injectors,” *Nature materials*, vol. 9, no. 7, pp. 586–593, 2010.

[127] S. Kivelson and D. Rokhsar, “Bogoliubov quasiparticles, spinons, and spin-charge decoupling in superconductors,” *Physical Review B*, vol. 41, no. 16, p. 11693, 1990.

[128] P. Tedrow and R. Meservey, “Spin polarization of electrons tunneling from films of fe, co, ni, and gd,” *Physical Review B*, vol. 7, no. 1, p. 318, 1973.

[129] R. Meservey and P. Tedrow, “Spin-polarized electron tunneling,” *Physics Reports*, vol. 238, no. 4, pp. 173–243, 1994.

[130] H. L. Zhao and S. Hershfield, “Tunneling, relaxation of spin-polarized quasiparticles, and spin-charge separation in superconductors,” *Physical Review B*, vol. 52, no. 5, p. 3632, 1995.

[131] M. Tinkham, “Tunneling generation, relaxation, and tunneling detection of hole-electron imbalance in superconductors,” *Physical Review B*, vol. 6, no. 5, p. 1747, 1972.

[132] B. D. Josephson, “Possible new effects in superconductive tunnelling,” *Physics Letters*, vol. 1, no. 7, pp. 251–253, 1962.

[133] J. Bardeen, “Tunnelling from a many-particle point of view,” *Physical Review Letters*, vol. 6, no. 2, p. 57, 1961.

[134] S. Takahashi, H. Imamura, and S. Maekawa, "Spin imbalance and magnetoresistance in ferromagnet/superconductor/ferromagnet double tunnel junctions," *Physical review letters*, vol. 82, no. 19, p. 3911, 1999.

[135] A. Anthore, H. Pothier, and D. Esteve, "Density of states in a superconductor carrying a supercurrent," *Physical review letters*, vol. 90, no. 12, p. 127001, 2003.

[136] R. Dynes, V. Narayanamurti, and J. P. Garno, "Direct measurement of quasiparticle-lifetime broadening in a strong-coupled superconductor," *Physical Review Letters*, vol. 41, no. 21, p. 1509, 1978.

[137] P. Fulde, "High field superconductivity in thin films," *Advances in Physics*, vol. 22, no. 6, pp. 667–719, 1973.

[138] P. Alemany, J.-P. Pouget, and E. Canadell, "Essential role of anions in the charge ordering transition of α-(bedt-ttf)$_2$i$_3$," *Phys. Rev. B*, vol. 85, p. 195118, May 2012.

[139] M. Monteverde, M. O. Goerbig, P. Auban-Senzier, F. Navarin, H. Henck, C. R. Pasquier, C. Mézière, and P. Batail, "Coexistence of Dirac and massive carriers in α-(bedt-ttf)$_2$i$_3$ under hydrostatic pressure," *Phys. Rev. B*, vol. 87, p. 245110, Jun 2013.